Risk assessment of ground movements: application to a case study in Lisbon

Mariana Isaura de Moura Ormeche

Thesis to obtain the Master of Science Degree in

Civil Engineering

Supervisor: Prof. Rui Pedro Carrilho Gomes

Examination Commitee

Chairperson: Prof. Teresa Maria Bodas de Araújo Freitas

Supervisor: Prof. Rui Pedro Carrilho Gomes

Member: Prof. Alexandre da Luz Pinto

December 2020

Declaration

I hereby declare that this document is an original work of mine and complies with all the requirements of the Code of Conduct and Good Practices of the University of Lisbon.

Acknowledgments

Throughout the writing of this dissertation I have received a great deal of support and assistance.

I would first like to express my special thanks to my supervisor, Professor Rui Carrilho Gomes, for challenging me on this topic and for all the support, guidance, dedication, availability, advise and motivation. His expertise was invaluable in formulating the research questions and methodology. His insightful feedback also pushed me to sharpen my thinking and brought my work to a higher level.

I would also like to acknowledge the professors from the geotechnical department for the enthusiasm with which they transmit their knowledge, allowing the students to acquire the same taste for geotechnical engineering, and always showing availability to clarify doubts and give advice.

I want to thank Luisa Beltramone, my office partner, for the support and motivation throughout the process of researching and writing of this thesis but also for the friendship and of course all the happy distractions.

I also want to thank Gonçalo Moura from the NDA for all the advices, help and support throughout this process of researching and writing.

I must also express my gratitude to my family, in particular my parents, for all their unfailing support and continuous encouragement throughout my years of study as well as their wise counsel and sympathetic ear. Thank you for pushing me further and help me reach my goals.

Finally, I would like to acknowledge my friends for all their support, not only during the process of putting together this dissertation, but during these five years of study. Especially, I would like to thank Gonçalo, João, Madalena, Marta and Valter with whom I had the pleasure to share this journey at Instituto Superior Técnico, I could not have asked for better colleagues and friends.

Resumo

Os riscos geológicos, tais como deslizamentos de terras, sismos, riscos geotécnicos e inundações são uma grande preocupação para a cidade de Lisboa. Esta dissertação centra-se principalmente na análise do movimento do terreno que pode levar a um deslizamento de terras em grande escala no coração da cidade antes das obras de estabilização, numa área conhecida como o Miradouro de São Pedro de Alcântara (MSPA). O MSPA é um miradouro emblemático de Lisboa, embutido numa encosta, onde foram observados deslocamentos crescentes no muro de contenção.

O muro foi instrumentado desde 2010 com dezasseis alvos topográficos distribuídos de cada lado do muro para medir os seus deslocamentos em 3D. Os deslocamentos 3D do muro foram registados de 2010 a 2012 e de 2016 a 2018. Foram também instalados cinco inclinómetros com deslocamentos laterais medidos de 2011 a 2016 e de 2017. Para complementar os deslocamentos medidos no local, os deslocamentos verticais do MSPA também foram medidos de 2015 a 2018 utilizando a técnica InSAR.

Os parâmetros geotécnicos do solo foram determinados, e os padrões de deslocamentos observados no caso de estudo foram avaliados para determinar se representam instabilidade do talude. Foram então utilizados métodos de previsão de deslizamento de terras para determinar um tempo de colapso para o talude. Finalmente, foram estabelecidas as possíveis causas para estes movimentos do terreno, e foi desenvolvido um modelo numérico do MSPA para identificar as causas mais prováveis do movimento do terreno.

Palavras-chave

Deslizamento de terras, Métodos de previsão de deslizamento de terras, Fatores de desencadeamento de deslizamentos de terras, Movimento do Terreno

Abstract

Geohazards such as landslides, earthquakes, geotechnical risks and floods are a major concern in terms of risk for the city of Lisbon. This dissertation mainly focusses on the analysis of ground movements that can may lead to a large-scale landslide in the heart of the city before the stabilization works, in an area known as the *Miradouro de São Pedro de Alcântara* (MSPA). The MSPA is an emblematic viewpoint in Lisbon embedded in a slope, where increasing displacements were observed in the retaining wall.

The wall was instrumented since 2010 with sixteen topographical marks distributed on each side of the wall to measure its 3D displacements. The 3D displacements of the wall were registered from 2010 to 2012 and from 2016 to 2018. Five inclinometers were also installed to measure lateral displacements from 2011 to 2016 and from 2017. To complement the displacements measured on site, the vertical displacements of the MSPA from 2015 to 2018 were also measured using InSAR technique.

The geotechnical parameters of the soil were determined, and the displacements patterns observed of the case study were evaluated to determine whether they represent instability of the slope. Landslide forecasting methods were then used to determine a time of failure for the slope. Finally, the possible causes for these ground movements are established, and a numerical model of the MSPA were developed to identify the most probable causes of the ground movement.

Keywords

Landslide, Landslide forecasting methods, Landslide triggering factors, Ground movements

Contents

List of Figures

List of Tables

Abbreviations and acronyms

Abbreviations

COV	Coefficient of Variation
CW	Construction Works
E	Earthquake
EWS	Early Warning System
FE	Finite Elements
GZ	Geotechnical Zone
HS	Hardening Soil model
HSsmall	Hardening Soil with small strain-stiffness model
InSAR	Interferometric synthetic-aperture radar
LMA	Long-term Moving Average
MSPA	*Miradouro de São Pedro de Alcântara*
PI	Plasticity Index
SPT	Standard Penetration Test

Symbols

Δ	increment

Latin alphabet

A	empirical value of the Fukuzono (1985) method
B	constant of Mufundirwa et al. (2010) method
c	constant of Hayashi et al. (1988) method
c'	effective cohesion
c_u	undrained shear resistance
C	constant of Mufundirwa et al. (2010) method
D	displacement
E	shear strength
E_0	initial shear strength
E_{50}	secant stiffness at 50% of failure load
E_{50}^{ref}	secant stiffness in standard drained triaxial test at 50% of failure load
E_{oed}^{ref}	tangent stiffness for primary oedometer loading
E_{ur}^{ref}	unloading / reloading stiffness for p^{ref}
G_0	initial shear modulus
G_0^{ref}	reference shear modulus at very small strains ($\varepsilon < 10^{-6}$)
h_{pen}	penetration observed when the SPT was stopped

K_0	earth pressure coefficient at rest
K_0^{nc}	K_0-value for normally consolidated soils
m	constant of Hayashi et al. (1988) method
m	Power for stress-level dependency of stiffness
N_{60}^*	corrected value of N_{STP}^* value
N_{SPT}	number of blows of the SPT
N_{STP}^*	extrapolated number of blow of the SPT needed to reach a 30 cm penetration
p^{ref}	reference stress for stiffness
q_a	asymptotic value of the shear strength
q_f	ultimate deviatoric stress
R_f	failure ratio q_f/q_a
R_{inter}	strength reduction factor
t	time
t_f	predicted time of failure
$\bar{t_f}$	mean of forecasts
T_f	actual time of failure
t_L	time left to failure
t_p	time of prediction
v	velocity
V_S	shear wave velocity
w	water content
w_L	liquid limit
w_P	plastic limit

Greek alphabet

α	empirical value of the Fukuzono (1985) method
γ	unit weight
$\gamma_{0.7}$:	threshold shear strain at which the secant shear modulus $0.722G_0$
γ_{unsat}	unsaturated unit weight of soil
γ_s	shear strainl
γ_{sat}	saturated unit weight of soil
δ	displacement
$\bar{\delta}$	smoothed displacement
ε	strain
$\dot{\varepsilon}$	strain rate
Λ	inverse velocity
ρ	soil density
σ_1'	effective vertical stress

σ_3'	effective horizontal stress
$\sigma_{tension}$	tensile strenght
υ	Poisson's ratio
υ_{ur}	Poisson's ratio for unloading-reloading
φ'	effective shear strength angle
$\bar{\phi}_{tc}$	triaxial compression shear angle
ψ	angle of dilatancy

1. Introduction

1.1. Framework and objectives

Risk represents the potential loss of lives, livelihoods, assets and services that can occur to a particular community or society in a specific period of time. Risk is determined probabilistically as a function of hazard, exposure, vulnerability and capacity. In an urban context, the exposure factor increases the risk value, as the number of lives, livelihoods, assets and services is higher and concentrated in a small space. For a city, a way to reduce the risk is to assess the hazards it is exposed to, understand where and why they occur, their effects and the probability of occurrence, to be able to mitigate the effects those hazards can have and reduce the value of risk.

In the case of Lisbon city, geohazards such as landslides, earthquakes, geotechnical risks and floods are a major concern in terms of risk. This dissertation main focus is the analysis of ground movements that may lead to a large-scale landslide in the heart of the city. For that, the ground movements of the *Miradouro de São Pedro de Alcântara* (MSPA) before the stabilization works are analysed. The MSPA is an emblematic viewpoint in Lisbon embedded in a slope, where increasing displacements were observed in the retaining walls.

Considering the 3D displacements observed with topographical monitoring between 2010 and 2012, and between 2016 and 2017, the lateral displacements with depth measured by the inclinometers between 2011 and 2016, and in 2017, as well as the vertical displacements registered by Interferometric synthetic-aperture radar (InSAR) technique between 2015 and 2018. The aim of this document is to identify the possible causes of these observed displacements and if they present a risk of landslide of the MSPA.

The case study is firstly characterized, describing the historical background of the site, then its geological conditions and its geotechnical parameters are defined. The observed displacements are analysed, and it is determined whether they represent instability of the slope. For that, the type of ground movement that it generates is determined (e.g. WP/WLI, 1993) and the possible causes for these displacements are established. The stability of the MSPA is also addressed by using landslide forecasting methods (e.g. Fukuzono, 1985) to predict a possible time of failure for the slope. Subsequently a numerical model of the case study is developed to confirm the hypothesis for the causes of the ground movement.

1.2. Organization of the document

The present dissertation is divided in seven chapters, the first chapter being an introduction where the objectives of the work are presented as well as its structure.

The second chapter characterizes what is a landslide, the classification of its types of movement, its triggers, the possible states of activity and the types of displacement throughout these states.

In the third chapter, landslide forecasting methods are presented. The forecasting methods consist in predicting the time of failure of a slope using kinematic parameters such as displacement and its derivates, velocity and acceleration, that can be directly related with the stability conditions of a slope. Comparing then examples of application, the most reliable method is determined.

The fourth chapter presents the case study, the MSPA, its historical background, geological and geotechnical conditions. To determine the geotechnical conditions of the MSPA, data from conventional geotechnical surveys: Standard Penetration Tests (SPTs) and laboratory tests, as well as data from surface wave method are analysed and then compared to determine the geotechnical parameters of the soil.

In the fifth chapter the displacements observed are analysed. The displacements observed result from topographical monitoring from 2010 to 2012, and from 2016 to 2018, measurements of inclinometers from 2011 to 2016 and from 2017, as well as InSAR monitoring from 2015 to 2018. Possible causes for the displacements are analysed, such as precipitation and earthquakes. Finally, the forecasting methods are used to predict if there is a risk of landslide for the MSPA.

The sixth chapter presents a numerical simulation of the displacements of the MSPA using the finite element program PLAXIS 2D, for geotechnical applications. First the constitutive model used (HSsmall) is described. Then the geometry of the numerical model is defined, and the model parameters determined. Thereafter the phases of analysis are presented, and the displacements calculated in the simulations are compared with the displacements observed on site. Lastly a pseudo static simulation is preformed to evaluate the effects of a landslide in the MSPA.

Finally, in the seventh chapter, the final considerations and study proposals for future developments are made to deepen the subjects studied.

2. Landslide characterization

2.1. Introduction

In general terms, a landslide is described as “a movement of a mass of rock, earth or debris down a slope” (e.g. Cruden, 1991).

Worldwide, between 1997 and 2017, landslides were responsible of 5,3% of the mortality caused by natural hazards in the Sendai Framework Monitoring system (UNDRR, 2019).

Various landslide classifications have been proposed over time, e.g. Hutchinson, 1967; Skempton & Hutchinson, 1969; Varnes, 1978. This work adopts the glossary proposed by the International Geotechnical Societies’ UNESCO Working Party on World Landslide Inventory, WP/WLI (1993b), which provides the main characteristics of a landslide. Those characteristics are described by geometry (features and dimensions), movement and activity (state and distribution).

2.2. Landslide types of movement

The type of movement in a landslide depends on the failure mechanism, the shape and extension of the landslide body, the geomechanical characteristics of the existing materials as well as the causes responsible for the failure. According to the WP/WLI (1993b), landslides can be characterized by five types of movement: fall, topple, slide, spread and flow, numbered from 1 to 5, respectively, in Figure 2.1.

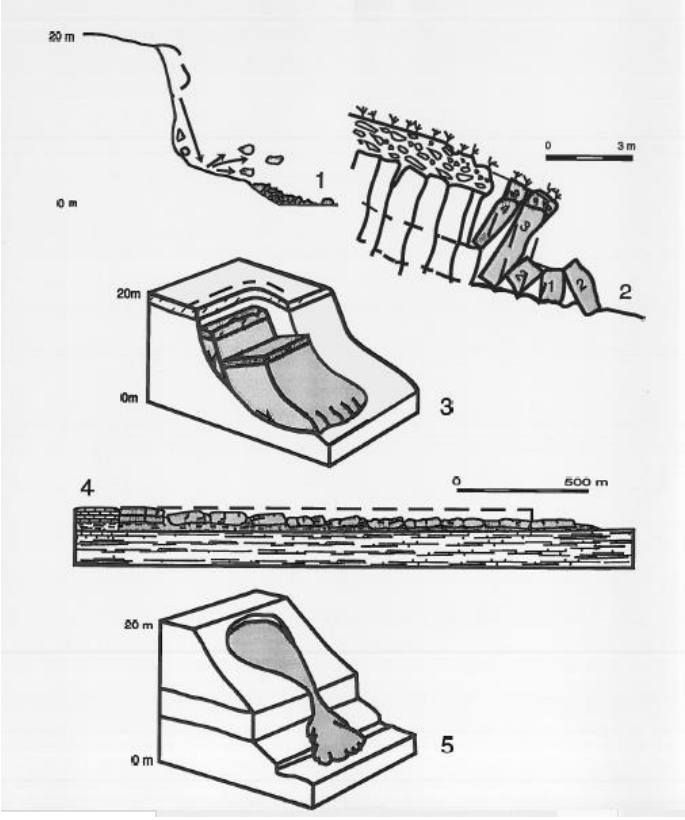

Figure 2.1. Landslide types of movement: (1) fall, (2) topple, (3) slide, (4) spread, (5) flow (WP/WLI, 1993b)

A fall (Figure 2.1.1) is the result of a detachment of soil or rock that descends through the air by falling, saltation or rolling. Usually, little or no shear displacement takes place in these cases.

A topple (Figure 2.1.2) is the result of a forward rotation out of the slope of a mass of soil or rock. The rotation is done around a point below the centre of gravity of the mass of soil or rock.

A slide (Figure 2.1.3) is a downslope movement of soil or rock mass along a surface of rupture in zones of intense shear strain. These surfaces of rupture are usually planar or circular, leading to translational or rotational slide, respectively. However, a purely planar or circular movement is rare, dislocating masses with a partially flat and partially curving shear surface are defined as compound.

A spread (Figure 2.1.4) is an extension of a cohesive soil or rock mass into softer underlying material. Spreads may be a result of liquefaction or flow. The surface of rupture is not a surface of intense shear. The main difference between rock and soil spreads is that for rocks, the movement is slow, almost constant rates and poorly affected by seasonal variation, while for soils, the movement is relatively quick, that can be influenced by short term effects such as climatic changes.

A flow (Figure 2.1.5) is a continuous movement of a mass of soil or debris with a distribution of velocities similar to the one of a viscous fluid. The surfaces of shear are short lived and usually not preserved.

It should be noted that a landslide can have different types of movement, for example, fall and topple. The number of types of movements is what describes the style of activity of a landslide.

2.3. Landslide triggering factors

Understanding why landslides occur allows the prediction of susceptibility of a given area. The triggering factors of slope instability are numerous, varied and can interact in complex and subtle way. However, from a wealth of case studies, the main causes of a landslide are well known and can be identified. Those triggering factors can be divided in two groups: inherent or basic factors, and external factors (Varnes, 1984).

2.3.1. Inherent or basic factors

When evaluating a slope stability, the first characteristic that has to be considered is the geology, this includes lithology, as well as structure. Lithology is important to determine parameters such as shear strength and permeability of the soil or rock. Structure consist in inhomogeneity and discontinuity in the soil or rock such as stratigraphic sequence, attitude of layering, faults and joints. At this stage topography plays a major role, considering the geotechnical parameters, the discontinuities and the slope gradient is an indicator of the slope stability.

Geomorphology should also be examined. The first geomorphological characteristic to be considered is the presence or absence of former landslides.

Then, hydrologic and climate conditions should be analysed, as water is one of the most important factors in slope stability. Precipitation and temperature changes can lead to changes in the movements and amount of water, as well as variation in pore water pressure that may lead to instability.

Vegetation should also be considered since it can have both favourable and unfavourable effects in slope stability. For example, a forest, as a whole, can mitigate the effects of climate in a slope, and the roots can act as a containment system, but they can also increase infiltration in the soil. The presence of trees can also amplify the effects of the wind and seismic action.

2.3.2. External factors

External factors that may trigger a landslide are the ones that change the stress conditions and/or the strength of the soil or rock that composes the slope (Varnes, 1984). In these factors water plays a major role. In fact, the hydrologic and climate conditions were already specified in the inherent factors, but as the variation of ground water level, due to, for example, human activities, or extreme rainfall as a result of climate change, generates variations in the pore water pressure that may lead to the reduction of effective stresses reducing the strength of the soil or rock. Another water related trigger that may cause instability in a slope could be a leaking pipe, that in the case of septic sewerage may lead to chemical changes in the ground.

Froude & Petley (2018), also list other factors that may trigger a landslide such as seismic actions, volcanic eruptions, construction works, change in land use, explosion, garbage collapse, human and animal activities, fire, freezing and marine erosion that cause stress changes in the slope. Changes that involve changes in the geometry of the slope, such as mining and hill cutting, might as well cause a landslide.

2.4. Landslide states of activity

According to the classification proposed by the WP/WLI (1993b), the states of activity of a landslide are:

1. **Active:** the landslide is currently moving.
2. **Suspended:** the landslide has moved during the past 12 months but is not currently active (1).
3. **Reactivated:** an active landslide (1) that has been inactive (4).
4. **Inactive:** the landslide has not moved during the past 12 months. States 5 to 8 are subdivisions of inactive landslides.
5. **Dormant:** an inactive landslide (4) that can be reactivated by its original causes or other causes.
6. **Abandoned:** an inactive landslide (4) that can no longer be affected by its original causes.
7. **Stabilized:** an inactive landslide (4) that has been protected from its original causes by artificial remedial measures.
8. **Relict:** an inactive landslide (4) that developed under climatic or geomorphological conditions considerably different from those at present.

Some of the states of activity of a landslide can be described in terms of displacement over time (Figure 2.2).

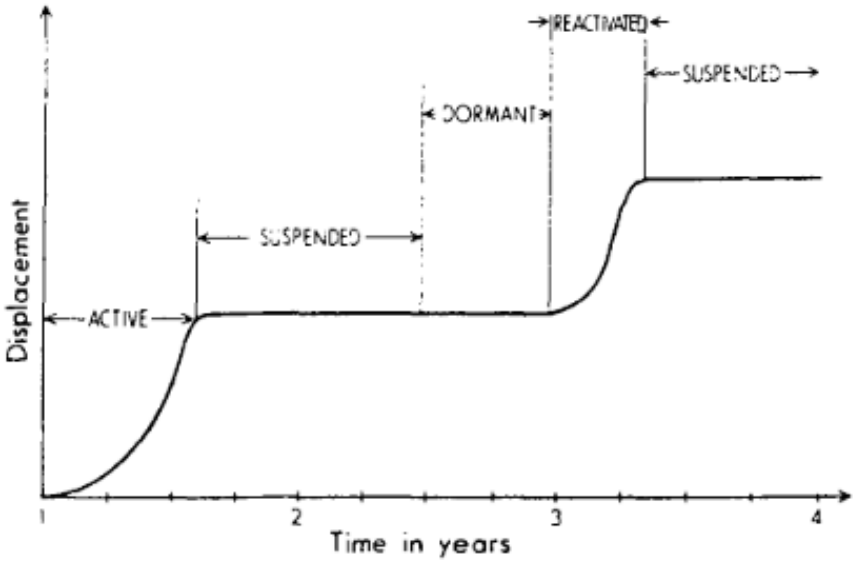

Figure 2.2. Displacement of a landslide in different states of activity (WP/WLI, 1993a)

We can understand from Figure 2.2, that what characterizes an active (1) or reactivated (3) landslide is the rapid increase of displacement over a short period of time. Meaning that if this increase of displacement can be predicted, a landslide forecast is possible.

3. Landslide forecasting methods

3.1. Introduction

Landslide forecasting consists in predicting a slope failure. This forecast can either be defined in spatial or temporal terms, depending on whether we want to predict where or when a landslide will occur, respectively.

The spatial forecast consists of estimating the probability of where a slope failure may occur, resulting in the spatial distribution of potential or existing landslides. It usually considers factors such as slope gradient, lithology, land cover or drainage, that helps to classify a given area or volume in terms of susceptibility, hazard, risk and vulnerability. These conditions are usually reproduced and presented in maps. Landslide spatial prediction would require a deeper dissertation that is not within the scope of this document, the focus will be in estimating the time of failure of a given slope.

Several methods have been established to predict the time of failure of a given slope. These methods usually consist in monitoring and analysing a certain landslide trigger (e.g. rainfall) or the slope kinematic parameters (e.g. displacement, velocity and acceleration) (Intrieri et al., 2019). Having a time of prediction of a landslide can be one of the basis of an Early Warning System (EWS) that can help prevent life, material and economical losses.

As it was seen in the previous chapter (§2.3), water is one of the major triggers of movement in a slope. In fact, a relationship between rainfall amount and the occurrence of the landslide can be established. This approach usually uses rainfall-intensity, total event rainfall, event duration, event intensity and is based on antecedent precipitation (Guzzetti et al., 2007). As technology evolves, more accurate weather forecasts are preformed, leading to more accurate landslide forecasts based not only in rainfall monitoring but also in rainfall prediction.

Several EWSs have been established based on rainfall such as one developed by Segoni et al. (2015) in Tuscany, Italy, based on the intensity-duration thresholds and dividing the area in different alert zones. Or the EWS developed by Cheng et al. (2015) in Loess Plateau of North Shaanxi Province, China, based on the effective rainfall amount, establishing three rainfall amount conditions, associated with five levels of warning, depending on the zone of the study area.

However, since rainfall is an indirect factor of instability, this kind of approaches are more prone to false or missed alarms. This is why the most reliable parameters for landslide time forecasting are the slope displacements and its derivatives, velocity and acceleration (Intrieri et al., 2019), these parameters can be directly related with the stability conditions of the slope (Lacasse & Nadim, 2009). Over its life time, a slope displacements can be described in a three stage curve (Figure 3.1): primary stage with displacement increasing logarithmically and strain rate decreasing logarithmically, secondary stage with displacement increasing linearly and constant strain rate and tertiary stage with displacement increasing exponentially and a rapid increase of strain rate.

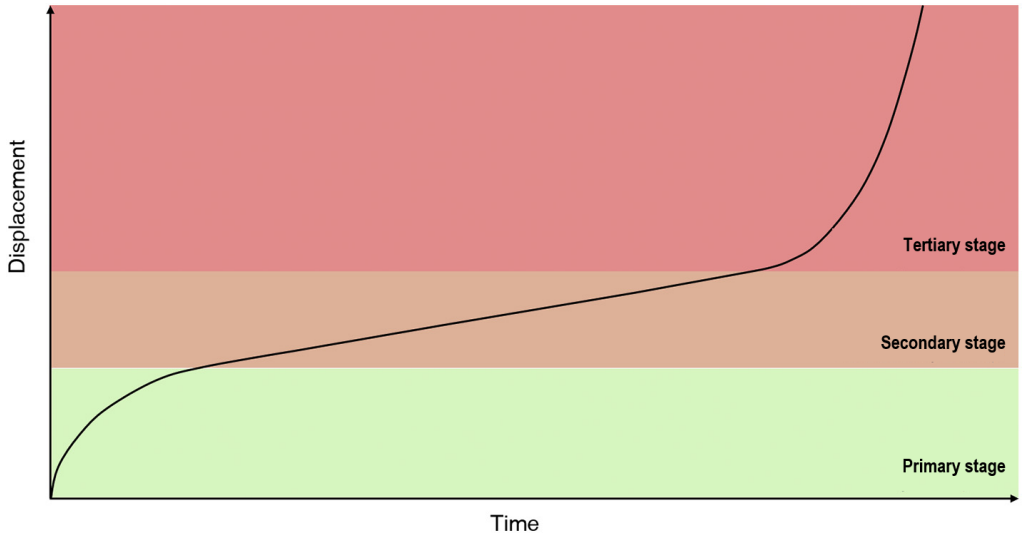

Figure 3.1. Conventional three stage interpretation of slope displacement (adapted from Intrieri et al., 2019)

Once a slope reaches tertiary stage, at the time t_0 (Figure 3.2.1), there are two possible outcomes, either the velocity increases asymptotically until the slope collapses at the time of failure t_f (Figure 3.2.2a), or, after an initial acceleration, the velocity decreases and the slope reaches a new equilibrium state without collapsing (Figure 3.2.2b).

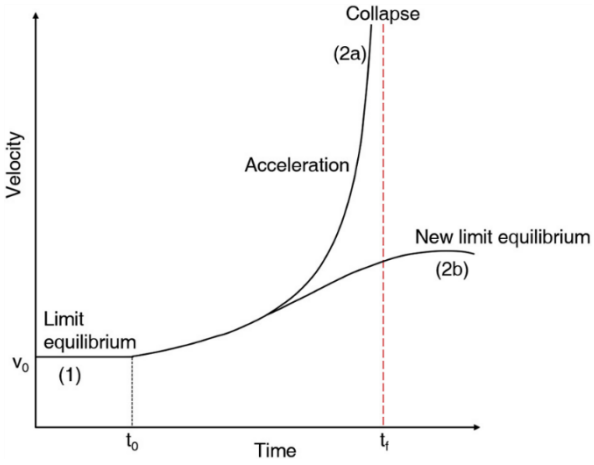

Figure 3.2. Possible outcomes once a slope reaches tertiary stage (Intrieri et al., 2019)

Based on kinematic parameters, some empirical methods have been developed. These methods have no intrinsic restriction to size, state of activity and type of material (Intrieri & Gigli, 2016), and are usually applied to sliding, toppling and compound landslides, yet there are some examples of rarer applications to rockfalls, wedge failures and slow earth flows.

3.2. Empirical methods

Empirical methods are based on the observation that displacement velocity increases exponentially before failure. The time of failure is then extrapolated through geometrical arguments from which equations can be derived.

One of the firsts to introduce a method to forecast a slope time of failure were Saito & Uezawa (1961). Based on the secondary stage curve, they determined an empirical formula, equation (3.1), based on the relationship between strain rate (in 10^{-4} min), $\dot{\varepsilon}$, and the time left to failure (in min), t_L.

$$\log_{10} t_L = 2{,}33 - 0{,}916 \log_{10} \dot{\varepsilon} \pm 0{,}59 \tag{3.1}$$

The predicted time of failure,t_f, is then determined by equation (3.2) relating the time left to failure, t_L, and the time of prediction, t_p.

$$t_f = t_L + t_p \tag{3.2}$$

The strain rate was used instead of displacement because of the monitoring equipment available at the time.

Later, Saito (1969) presented a more successful approach, developing a graphical method based on the tertiary stage curve (Figure 3.3), justified by geometrical arguments. After plotting displacement or strain versus time, three points have to be selected: $A_1(\Delta D_1, t_1)$, $A_2(\Delta D_2, t_2)$ and $A_3(\Delta D_3, t_3)$, with an equal difference of displacement, ΔD. The projections of A_1 and A_3, A_1' and A_3', respectively, are represented on a line parallel to the time axis that passes through A_2. Then, M and N are the midpoints of $A_1'A_2$ and $A_1'A_3'$, respectively. M' and N' are the projections of M and N, respectively, on a line parallel to the displacement axis that passes though A_2. The predicted time of failure, t_f, is then determined as the line $A_1'N'$ intercepts the line parallel to the time axis that passes through M'.

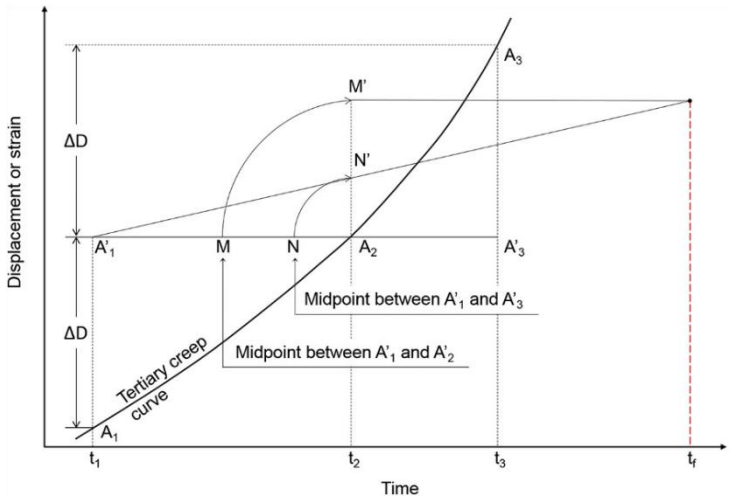

Figure 3.3. Graphical methods presented by Saito (1969) (Intrieri et al., 2019)

Although the graphical approach is recommended, the equation (3.3) was also derived, which is more practical for numerical solutions.

$$t_f = \frac{t_2^2 - t_1 t_3}{2t_2 - (t_1 + t_3)} \tag{3.3}$$

Developing Saito's idea of a simpler graphical method, Fukuzono (1985) also presented a graphical approach valid for tertiary stage. The Fukuzono (1985) method consists of plotting the inverse

velocity, Λ, versus time, t. If the slope is in equilibrium, the plot will show a line parallel to the time axis, once tertiary stage is reached and the velocity increases asymptotically, the plot will show a decreasing line whose extrapolation intercepts the time axis at the predicted time of failure, t_f.

The inverse velocity, Λ, is then concluded to correspond to equation (3.4), for the cases of slow and continuous deformation, that was derived from the linear correlation between the logarithm of acceleration and the logarithm of velocity during tertiary stage (Fukuzono, 1984; Fukuzono & Terashima, 1982).

$$\Lambda = \frac{1}{v} = [A(\alpha - 1)]^{\frac{1}{(\alpha-1)}}(t_f - t)^{\frac{1}{(\alpha-1)}} \tag{3.4}$$

Where A and α are two values found empirically, that are found not to be independent from each other and vary with the type of material and over-consolidation ratio (Dok et al., 2011; Minamitani, 2007).

For the cases where $\alpha = 2$, the plot is linear and the time of failure, t_f, is determined with linear regression, equation (3.5).

$$t_f = \frac{t_2\Lambda_2 - t_1\Lambda_1}{\Lambda_1 - \Lambda_2} \tag{3.5}$$

For the cases where $\alpha > 2$ or $1 < \alpha < 2$, the plot is convex or concave, respectively. For those cases, Fukuzono (1985) proposed a different graphical approach (Figure 3.4) that consists of drawing the tangent line of an arbitrary point Λ_1 at the time t_1, the tangent line will cross the time axis at the point t_{c1}. Afterwards, the point P_1 is plotted vertically above Λ_1 so that the segment t_1P_1 equals the segment t_1tc_1. The same process is repeated for the last point of the given data Λ_2. The time of failure, t_f, is then the interception of a straight line that passes through P_1 and P_2, with the time axis.

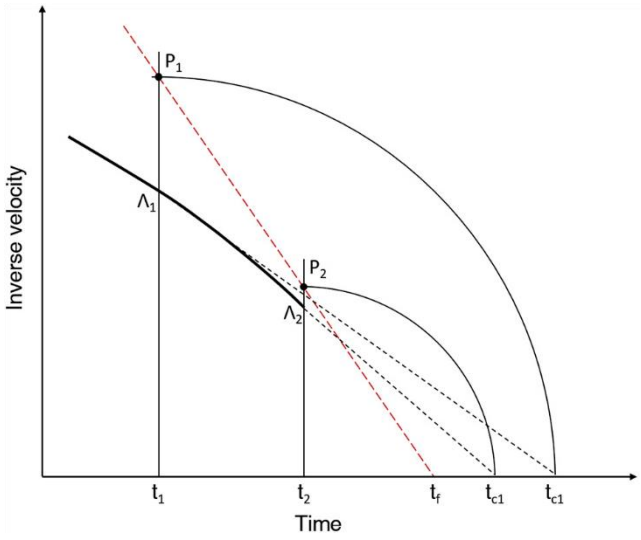

Figure 3.4. Graphical method for determining the time of failure when $\alpha \neq 2$ by Fukuzono (1985) (Intrieri et al., 2019)

Since the Fukuzono (1985) method relies on the inverse value of a derivate parameter, velocity, the time series experience a high degree of variability, and instrumental or natural noise in displacement

measurements propagates when calculating the inverse velocity, which can lead to less accurate forecasts.

Also presenting a graphical method, Azimi et al. (1988) developed Asaoka's (1978) approach to assess the final settlement in an oedometer test, by plotting displacement versus time and individualizing segments of equal displacement, ΔD. As velocity, v, increases the time intervals, Δt, will shorten until $\Delta t \rightarrow 0$ (Figure 3.5.a), meaning that the final and initial instant of the final time interval, t_i and t_{i-1}, respectively, tend to be equal. In tertiary stage, plotting t_i versus t_{i-1} will align in a straight line and the time of failure, t_f, will correspond to the interception of that line with the line that represents the identity ($t_i = t_{i-1}$), that can be extrapolated (Figure 3.5.b).

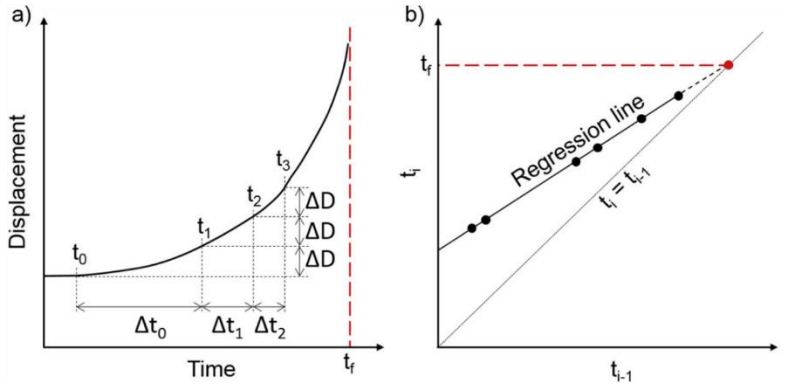

Figure 3.5. Graphical method by Azimi et al. (1988): (a) displacement curve before rupture; (b) variations between t_i and t_{i-1} (Intrieri et al., 2019)

The predictions made by the three methods presented above (Azimi et al., 1988; Fukuzono, 1985; Saito, 1969) all coincide when $\alpha = 2$ in the Fukuzono (1985) method (Intrieri et al., 2019). However, because of its simpler application, the Fukuzono (1985) method is most frequently used. It should also be noted that these methods need constant updated data to detect trend changes in the displacement and provide more accurate forecasts.

Aside from graphical methods, Hayashi et al. (1988) derived equation (3.6), based on the observation that there is a higher velocity at an early stage of tertiary stage.

$$t_L = c(\Delta t)^m \tag{3.6}$$

Where, c and m are constants, 2,13 and 1,6, respectively, empirically calculated from seven natural slope failures and Δt is the required time interval for a displacement of 10 cm starting from the beginning of tertiary stage. One of the advantages of this method is that it can predict failure at an early stage, since it is appliable to the beginning of tertiary stage but cannot be updated in case of trend changes and the early stage of tertiary stage need to be spotted in the collected data. Additionally, as it was never popular, we are not able to know how much c and m can vary from case to case.

More recently, Mufundirwa et al. (2010) started with Fukui & Okubo (1997) equation (3.7) that represents strain divergence in the terminal phase of stage failure in rocks, and replaced the strain, ε, with the displacement, D, obtaining equation (3.8).

$$\varepsilon = -B \log(t_f - t) + C \tag{3.7}$$

$$\frac{dD}{dt} = v = \frac{B}{t_f - t} \tag{3.8}$$

Where B and C are constants, t_f the time of failure, t the time of prediction and v the velocity. Multiplying equation (3.8) by the life expectancy of the slope, $t_f - t$, equation (3.9) is obtained and can be re-written as equation (3.10).

$$tv = t_f v - B \tag{3.9}$$

$$t_f = t + \frac{B}{v} \tag{3.10}$$

A graphical approach can be used, when plotting tv versus v, it shows a straight line where the predicted time of failure; t_f, is the angular coefficient of the line (Figure 3.6).

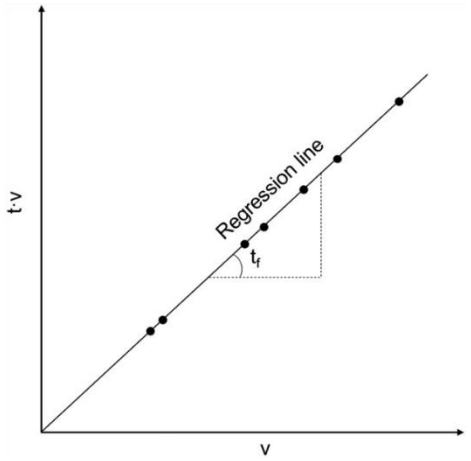

Figure 3.6. Graphical approach of Mufundirwa et al. (2010) method (Intrieri et al., 2019)

Mufundirwa et al. (2010) showed that their method provides reliable predictions for cases of plane rupture, but these results were more conservative than the ones predicted with the Fukuzono (1985) method. Plus, as the Mufundirwa et al. (2010) method is used for data in the terminal phase of tertiary stage, it cannot provide early stage predictions. The data should also be constantly updated in case of trend changes.

3.3. Examples of application

The Fukuzono (1985) method is the most used forecasting method. One example of its application is the Maoxian landslide that took place the 24 June 2017 at 5:45 a.m. in Xinmo Village, 50 km away from the Maoxian (Maoxian, namely Mao County, Aba Prefecture, Sichuan Province, China). About 18 million m^3 of rock debris, mainly cataclastic quartezite, slid off a slope above the village of about 55-60º (Intrieri et al., 2018; Jiang et al., 2017). The landslide buried 62 houses and more than 100 people (Chinese Government, 2017). After the event, the displacements of the landslide area from October 2014 until June 2017 were analysed and the Fukuzono (1985) method was applied to the accelerating time series (Figure 3.7).

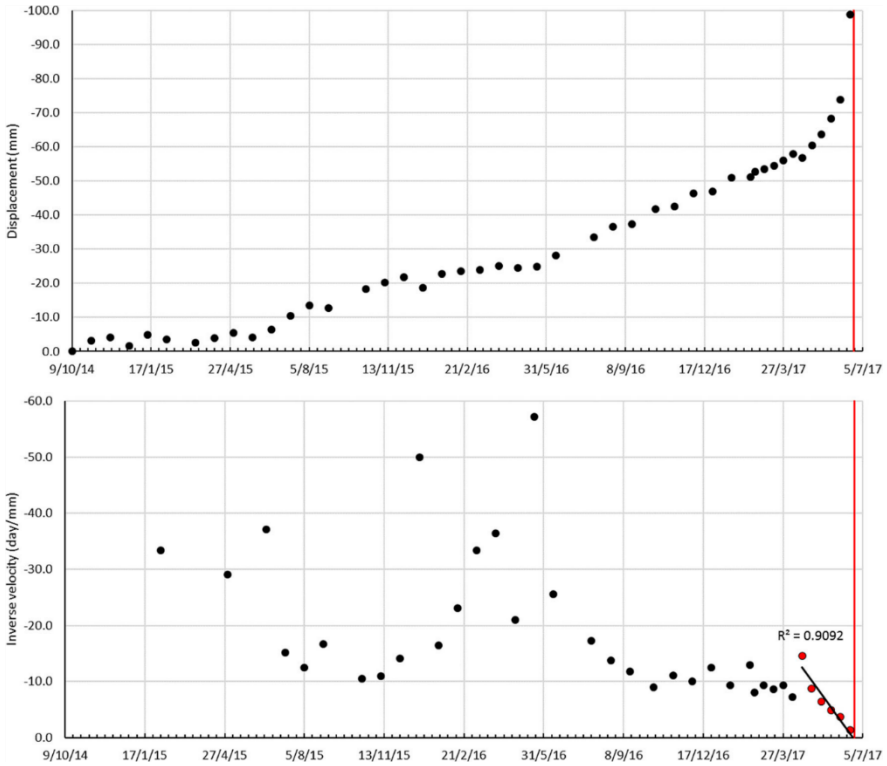

Figure 3.7. Location of Xinmo Village, the Maoxian landslide (Maoxian, namely Mao County, Aba Prefecture, Sichuan Province, China) and major historical earthquakes (adapted from Intrieri et al., 2018)

Until June 2016, the inverse velocity shows a large variability, due to the fact that when the velocity is almost null, the inverse velocity tends to infinite. Between June and October 2016, a decreasing trend is visible in the inverse velocity, which could indicate tertiary stage. However, the displacement plot does not show the typical hyperbolic curve until the begging of 2017. From the 20 April 2017 a trend change is detected. Using this data onwards the landslide forecasts were 10 June 2017, 19 June 2017 and 23 June 2017 using the data acquired in 26 May 2017, 7 June 2017 and 19 June 2017, respectively (Intrieri et al., 2018). The landslide could have been predicted, with a 1 day error, using the Fukuzono (1985) method, but it should be noted that the data has to be constantly updated in order to avoid misleading times of failure.

The Fukuzono (1985) method was effective for the Maoxian landslide, but is this method more effective than others? Intrieri & Gigli (2016) compared the forecast results of Saito (1969), Fukuzono (1985) and Mufundirwa et al. (2010) methods for different landslides (Table 3.1).

In order to compare the three methods, for each landslide, prediction plots were elaborated, plotting the time of prediction, t_p, over the predicted time of failure, t_f, (Figure 3.8), and the mean and the standard deviation of the forecast were also calculated (Figure 3.9).

Table 3.1. Landslide cases description (adapted form Intrieri & Gigli, 2016)

Name	Material	Type	Brittleness	Volume (m^3)	Trigger	Reference
Liberty Pit	Weathered quartz monzonite	Rockslide?	Medium/high	6×10^6	Blasts, pore water pressure	(Rose & Hungr, 2007; Zavodni & Broadbent, 1980)
Landslide in mine	Consolidated alluvial sediments, weathered bedrock	Deep-seated toppling	Medium	10^6	NA	(Rose & Hungr, 2007)
Betze-Post	Weathered granodiorite	Rockslide?	Medium/high	2×10^6	Rainfall	(Rose & Hungr, 2007)
Vajont	Limestone and clay	Rockslide	High	$2{,}7 \times 10^8$	Pore water pressure	(Rose & Hungr, 2007; Semenza & Melidoro, 1992)
Stromboli[1]	Shoshonitic basalts	Bulging (not a landslide)	Medium/high	NA	Sill intrusion	(Casagli et al., 2009)
Monte Beni	Ophiolitic breccias	Topple/rockslide	High	5×10^5	NA	(Gigli et al., 2011)
Cerzeto	Weathered metamorphic rocks on top, cataclastic zone and Pliocene clays	Debris slide-earth flow	Medium/low	5×10^6	Prolonged rainfalls	(Iovine et al., 2006)
Avran Valley	Chalk	Rockslide	Medium/low	8×10^4	NA	(Azimi et al., 1988)
Giau Pass	Morainic material	Complex slide	Medium/low	5×10^5	Pore water pressure	(Angeli et al., 1989; Petley et al., 2002)

[1] Stromboli was not a landslide but a volcanic bulging preceding a vent opening that was forecasted in a similar was as a landslide

NA = not available

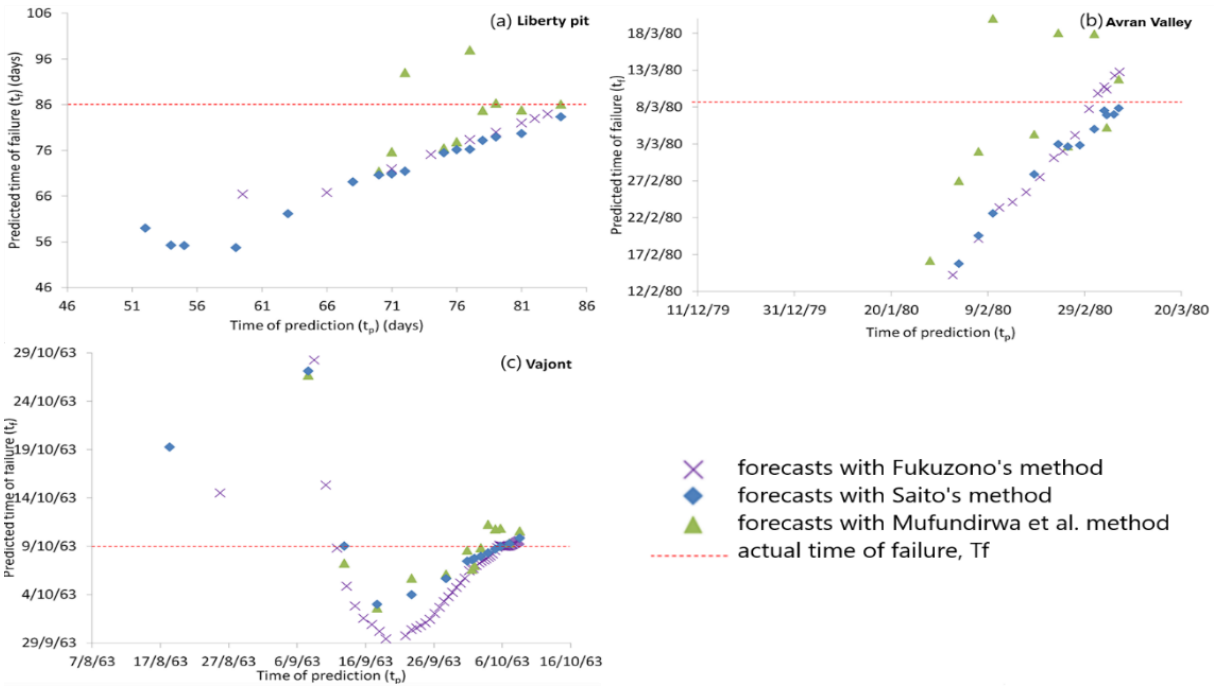

Figure 3.8. Prediction plots of the (a) Liberty pit, (b) Avran Valley and (c) Vajont landslides (adapted from Intrieri & Gigli, 2016)

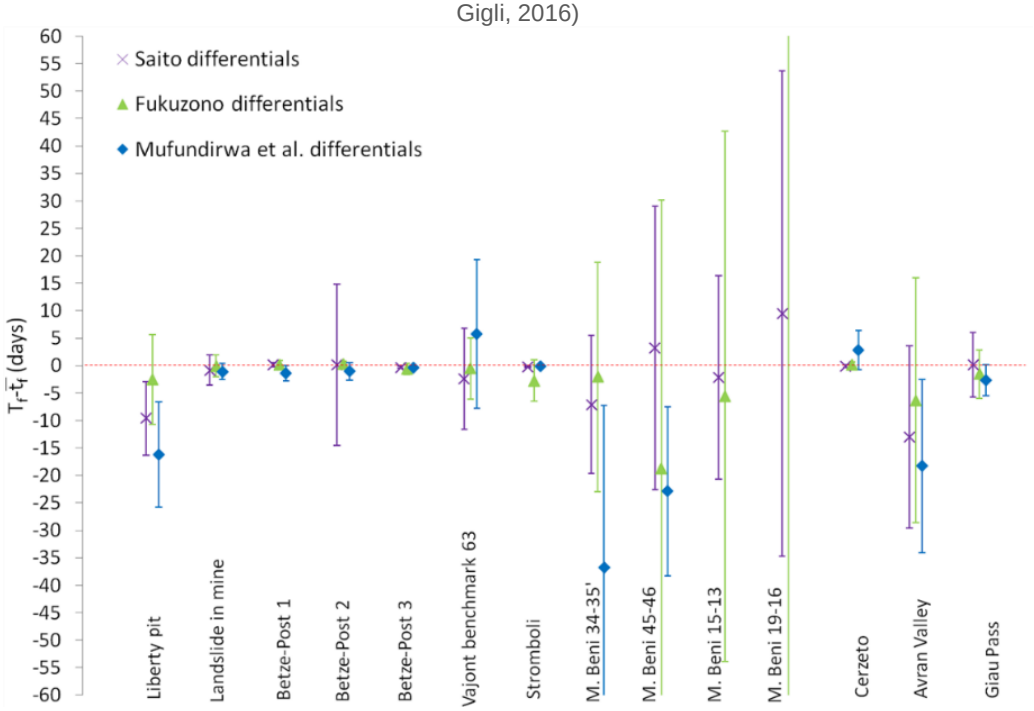

Figure 3.9. Differential between the mean of the forecasts ($\bar{t_f}$) and the actual time of failure (T_f) (adapted from Intrieri & Gigli, 2016)
The dashed line represents the exact time of failure ($T_f - \bar{t_f} = 0$). The error bars represent the standard deviations of the forecasts.

Overall, the Saito (1969) and the Fukuzono (1985) methods present more accurate mean forecasts, but also present a higher variability in the values. Considering the predictions below the dashed line in Figure 3.9 (predicted time of failure is before the event) it can be determined that using the Mufundirwa et al. (2010) method provides more conservative forecasts that could lead to more false alarms. Considering now the predictions over the dashed line in Figure 3.9 (predicted time of failure is

after the event) it is determined that the Saito's (1969) method is less conservative, that could lead to missed alarms.

It can be concluded that the forecast methods presented are a good indicator of a slopes instability and provide, in general, good predictions for the time of failure. However the quality of the forecast is directly linked to the quality of the data collected (kinematic parameters) and there is still work to do concerning the relations between the kinematic and the geomechanical parameters in order to improve these methods and predict more accurate landslide forecasts.

4. Case study - *Miradouro de São Pedro de Alcântara*

4.1. Introduction

The case study is the *Miradouro de São Pedro de Alcântara* (MSPA), one of the most emblematic viewpoints of Lisbon, providing a view over the *São Jorge* Castel, Lisbon's downtown and the Tagus River. It is located in the city centre, embedded in *São Roque*'s hill, next to *Bairro Alto* (Figure 4.1).

Figure 4.1. Location of the MSPA (adapted from GoogleEarth)

In 1732, the Lisbon City Hall acquired the land where the MSPA is today in order to extend the *Água Livres* Aqueduct to the *Graça* quarter (Figure 4.2) (Teixeira Duarte Engenharia, S.A., 2017b).

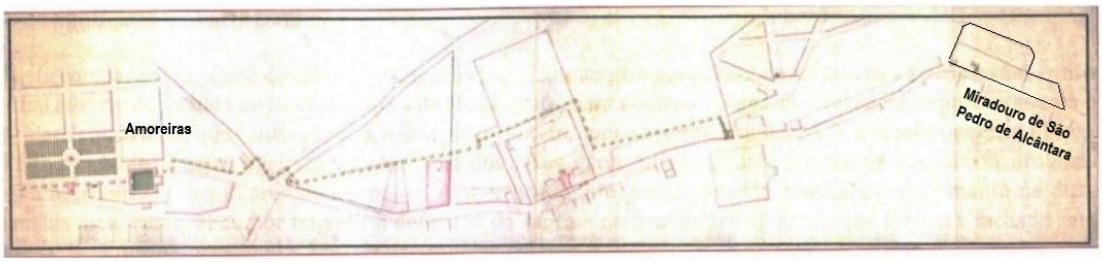

Figure 4.2. Water pipping project from *Amoreiras* to the MSPA (adapted from Teixeira Duarte Engenharia, S.A., 2017b) (unscaled)

From 1749 to 1754 takes place the construction of the retaining wall (Figure 4.3) as well as the fountain (Figure 4.3 and Figure 4.4). Unfortunately, the 1755 earthquake destroys a large part of Lisbon and the area of the MSPA is used as a landfill for material resulting from the destruction of the city, and the stability conditions of the area are not evaluated.

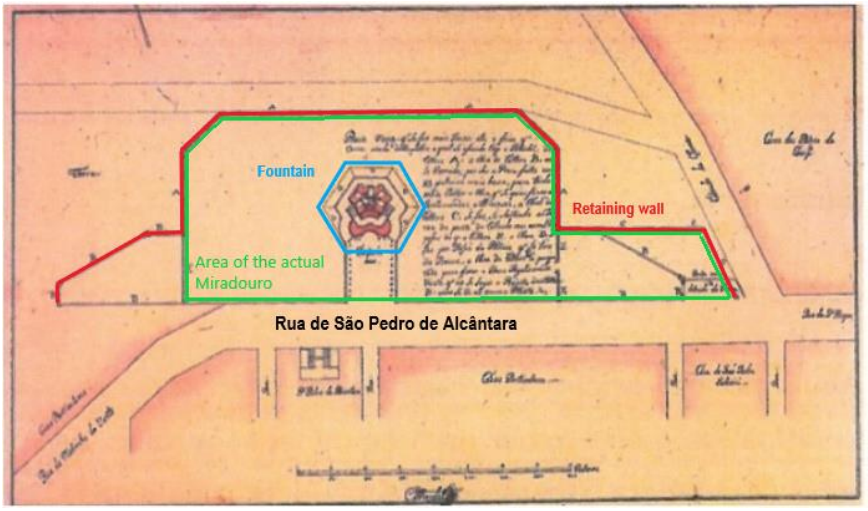

Figure 4.3. First retaining wall of the MSPA (Teixeira Duarte Engenharia, S.A., 2017b) (unscaled)

Figure 4.4. Fountain of *São Pedro de Alcântara* (Teixeira Duarte Engenharia S.A., 2017b)

In 1770, the construction of two platforms (Figure 4.5) over the existing retaining wall is conducted, but the reservoir for the extension of the Aqueduct was never built.

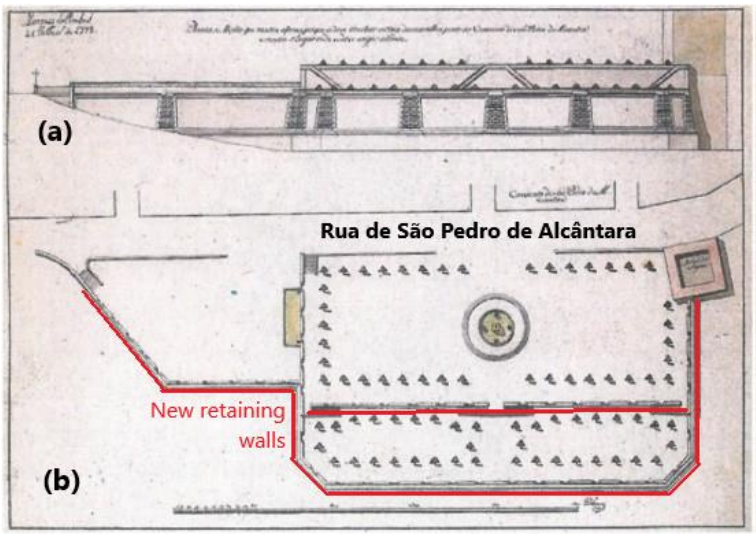

Figure 4.5. Two platform project of the MSPA (a) view from *Rua das Taipas*; (b) layout plan (Teixeira Duarte Engenharia,S.A., 2017b) (unscaled)

In 1830 the Royal Police Guard takes the initiative to conduct landscape works in the upper platform to create a garden. In 1835 the works ended in the lower platform, with stairs connecting the two platforms, turning the whole space into a public garden.

By the end of the 19th century, a few ideas were presented and discussed, but never accomplished, such as an exhibition hall proposed by the Society of Fine Arts in 1886 or a metallic viaduct connecting the MSPA to the *Campo Santana* area in 1888 (Figure 4.6).

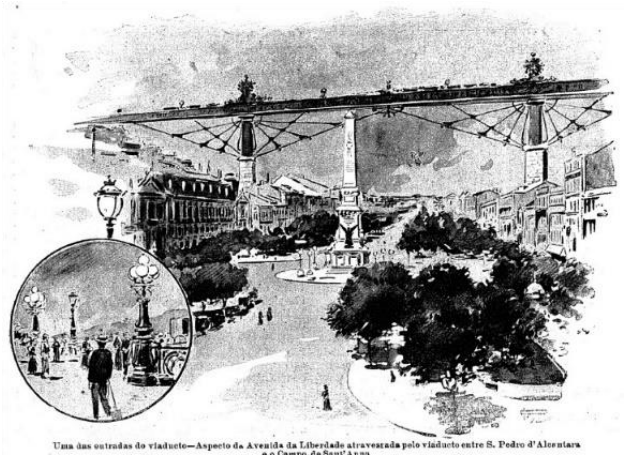

Figure 4.6. Illustration of the viaduct connecting the MSPA to the *Campo Santana* area (National Archive nº76, June 1933)

In 2006, rehabilitation works of the MSPA retaining wall were conducted. A monitoring system was installed in 2010, that identified a pattern of increasing displacements. Between May and October 2017, complementary stabilization works were conducted, where stabilization solutions were analysed by Carvalho (2017).

4.2. Geological conditions

According to the Geological Map of the Lisbon Council, the MSPA is located over *Areolas da Estefânia* (M^1_{II}) and *Argilas e Calcários dos Prazeres* (M^1_{I}) (Figure 4.7) both Miocene formations.

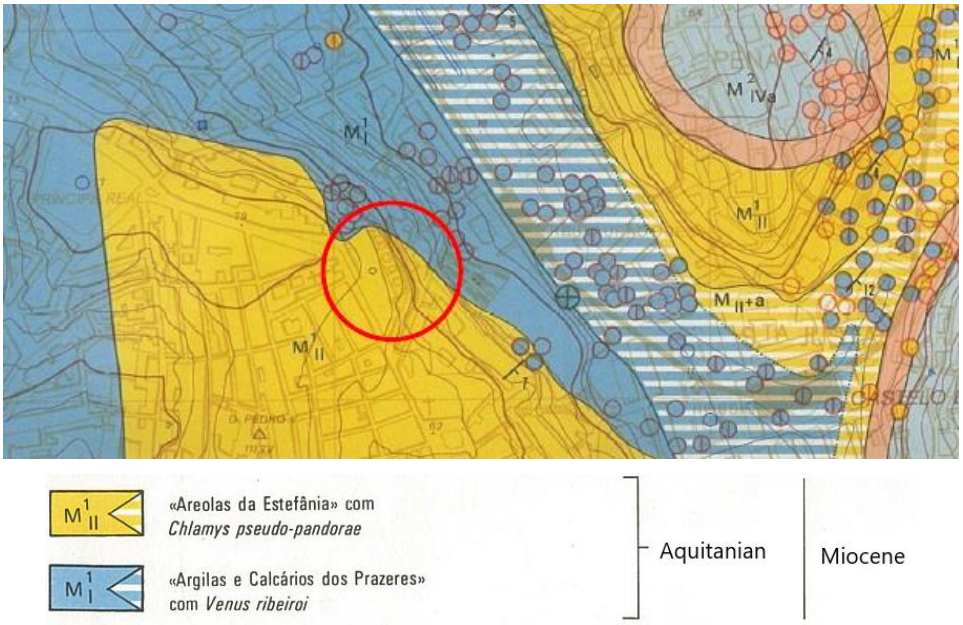

Figure 4.7. Adapted from the Geological Map of the Lisbon Council, sheet 4 (unscaled)

Based on the Geotest (2011) site investigation, the *Areolas da Esteania* unit is composed by fine silty sand and silt-sandy clays. The *Argilas e Calcários dos Prazeres* unit is composed by clays, silty clays, fine clayey sands, carbonated marlous clays and limestone, forming a high resistance core.

4.3. Geotechnical conditions

To characterize the geotechnical conditions of the MSPA, first, the data collected from the conventional geotechnical survey, and then the data from the surface waves method are analysed. Afterwards, the two analysis are compared to determine the geotechnical zones (GZs) that are used for the analysis of the displacements in the next chapters and finally the geotechnical parameters of each zone are determined.

4.3.1. Conventional geotechnical survey

The geotechnical survey conducted by Geotest (2011) included five boreholes, S1 to S5, with Standard Penetration Tests (SPTs) and recovery of remoulded samples for visual inspection and laboratory testing. The boreholes position is shown in Figure 4.8 and their depth and number of SPT tests presented in Table 4.1.

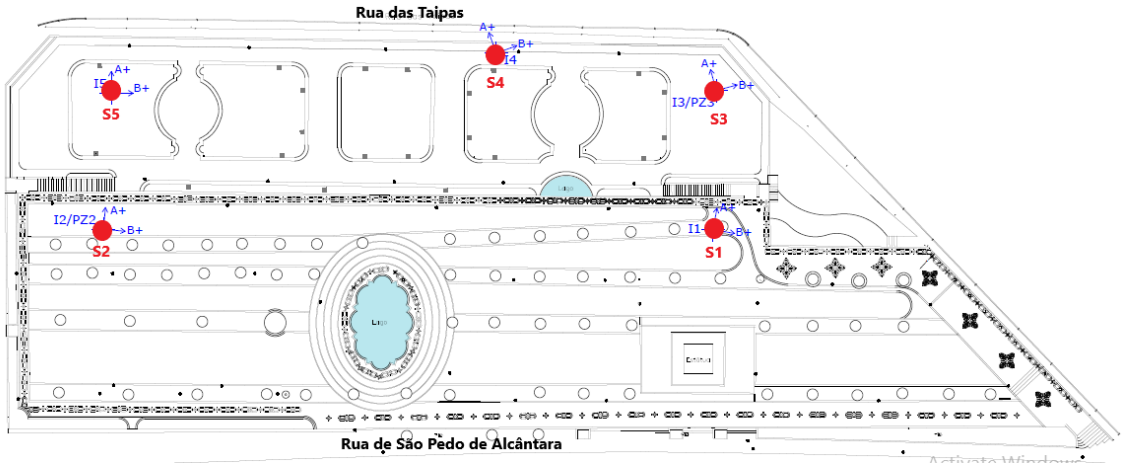

Figure 4.8. Position of the boreholes (adapted from Geotest, 2011) (unscaled)

Table 4.1. Boreholes log (adapted from Geotest, 2011)

Borehole nº	Depth (m)	Number of SPT tests
S1	31,85	21
S2	42,37	28
S3	37,42	21
S4	39,29	12
S4	34,72	23

4.3.1.1. SPT tests

The non-corrected values of N_{SPT} are analysed. For the tests that did not reach a 30 cm penetration, the number of blows needed to reach 30 cm is extrapolated, N^*_{SPT}, using equation (4.1)

$$N^*_{SPT} = \frac{N_{SPT} \times 30}{h_{pen}} \tag{4.1}$$

Where h_{pen} is the penetration measured (in cm) when the test was stopped at 60 blows.

Values over 120 blows will not be considered, as the extrapolated values above this limit are obtained for low penetration values that have a higher error associated. It should be noted that isolated values above 60 blows will not be considered either, as they could represent the interception with rigid blocs, that are not representative of the zone.

Based on the extrapolated SPT test results, three GZs are identified, GZ1 to GZ3 (Figure 4.9 and Table 4.2). The values of N_{SPT} and N^*_{SPT} are presented in Annex A.

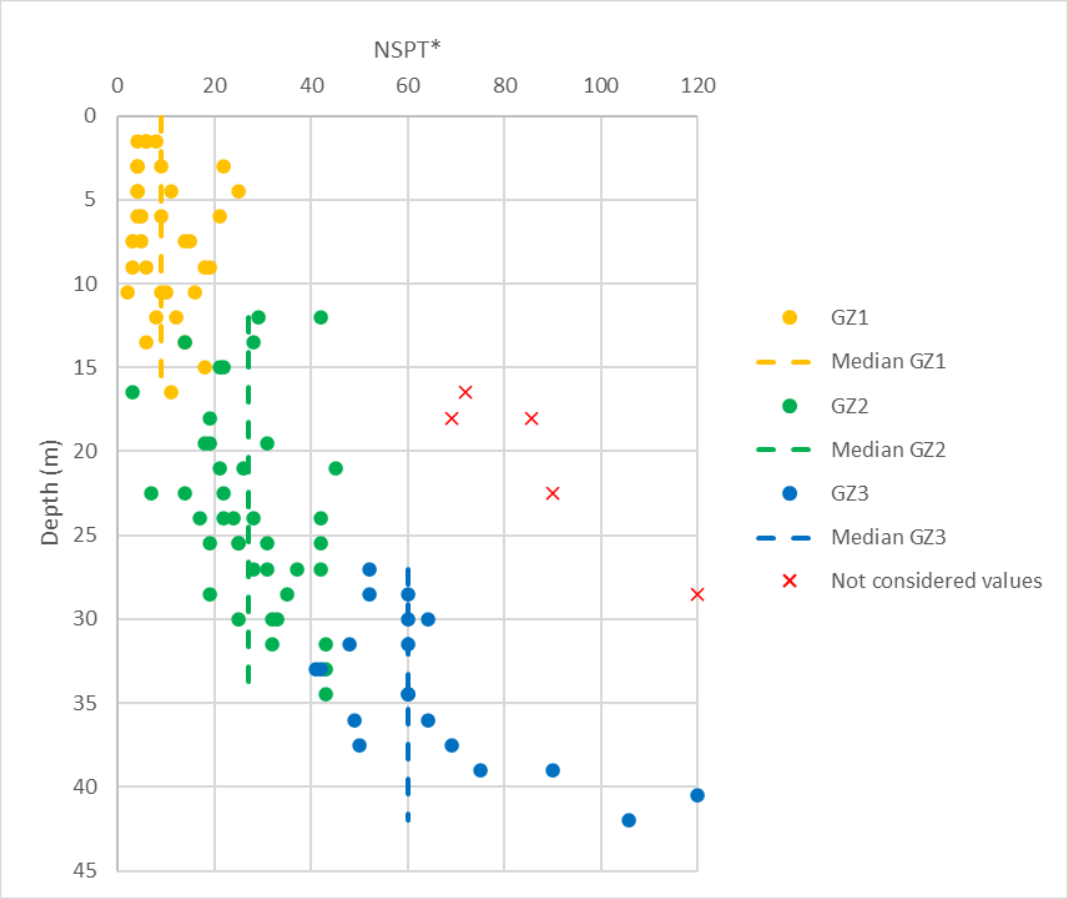

Figure 4.9. Extrapolated SPTs results[1]

Table 4.2. Statistical evaluation of N^*_{SPT} value for each GZ

	N^*_{SPT}						Depth (m)
	Minimum	Maximum	Average	Median	Standard deviation	Coefficient of Variation	
GZ1	2	25	10	9	6,18	63%	10,5-16,5
GZ2	3	45	27	27	10,26	37%	25,5-34,5
GZ3	41	120	65	60	19,78	31%	?

Considering the statistical values of N^*_{SPT} for each GZ (Figure 4.9 and Table 4.2) and comparing it with the remoulded samples, it can be concluded that GZ1 has the highest coefficient of variation (COV), 63%, probably due to its anthropic nature. It consists mostly of sandy clay with lithic fragments

[1] A value of $N^*_{SPT} = 900$ for a depth of 34,5 m (that was not considered in the data treatment) was not represented in this figure as it is too far apart from the rest of the values and made the figure non leasable in terms of x scale.

of varying size and nature, brick and plant matter uncarbonized. GZ1 is likely landfill, perhaps resulting from the destruction of the city in the 1755 earthquake, as the area was used as landfill at the time, and perhaps landfill from most recent works. GZ2 can be considered as a relatively homogeneous layer with a COV of 37% and consists mostly of silty and clayey sand, as well as sandy silts. GZ3 can also be considered as a relatively homogeneous layer with a COV of 31% and consists mostly of limestone and silty clays. Taking in account their compositions, GZ2 and GZ3 can be representative of the geological layers *Areolas da Estefânia* and *Argilas e Calcários dos Prazeres*, respectively.

4.3.1.2. Laboratory tests

The laboratory tests resulted in particle size distribution (Figure 4.10), the Atterberg limits and the ASTM unified soil classification (Table 4.3). The remoulded samples tested are from the boreholes S2 (13,45 m to 13,90 m), S3 (22,45 m to 22,90 m), S4 (22,45 m to 22,90 m) and S5 (13,45 m to 13,90 m). All these samples can be representative of GZ2, determined with the SPT results (§4.3.1.1), because of the borehole and the depth from where they were retrieved.

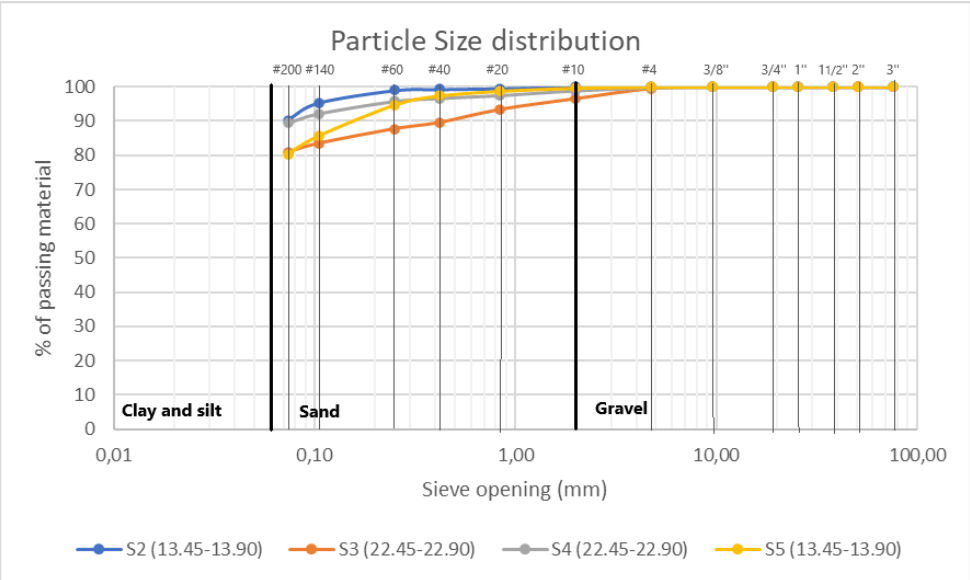

Figure 4.10. Particle size distribution of the four remoulded samples from GZ2 (adapted from Geotest, 2011)

Table 4.3. Atterberg limits and ASTM unified classification of the four remoulded samples from GZ2 (adapted from Geotest, 2011)

	Liquid Limit (%)	Plastic Limit (%)	Plasticity Index (%)	Water Content (%)	ASTM Unified Soil Classification
S2 (13,45 - 13,90)	34	20	14	21,8	CL low plasticity clay
S3 (22,45 - 22,90)	41	22	19	23,1	CL low plasticity clay with sand
S4 (22,45 - 22,90)	35	21	14	21,0	CL low plasticity clay
S5 (13,45 - 22,90)	33	19	15	21,4	CL low plasticity clay with sand
Average	36	20	15	22	

The laboratory tests performed on the four remoulded samples present similar results: low plasticity clays (CL) with small to very small amounts of sand, an average water content of 22%, and an average Plasticity Index (PI) of 15%.

4.3.2. Surface waves method

Surface wave methods follow three sequential steps: (i) acquisition of seismic data, (ii) processing, obtaining a dispersion curve estimation, and (iii) inversion, obtaining a model parameter optimization (Figure 4.11).

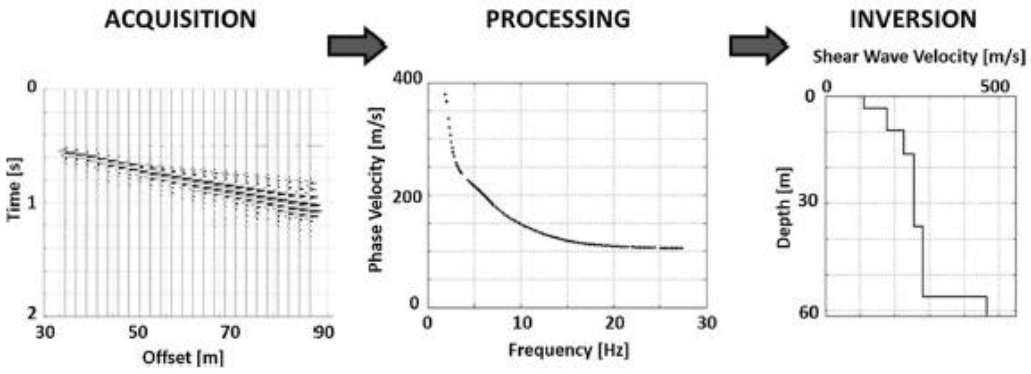

Figure 4.11. Conceptual flow of surface wave analysis (not including uncertainties): raw seismic data, experimental dispersion curve, V_S profile (Foti et al., 2018)

The initial shear modulus, G_0, of the soil is currently measured in the field by seismic surface methods, that provide shear wave velocity, V_S , profile. V_S and G_0 can correlated through the equation (4.2).

$$G_0 = \rho V_S^2 \tag{4.2}$$

Where ρ is the soil's density.

The V_S profile is also commonly used to estimate $V_{S,30}$, defined as the travel-time average shear wave velocity in the topmost 30 m of the subsurface, used in building codes such as the Eurocode 8, for a site's seismic response classification.

Oliveira (n.d.) conducted a surface wave survey at the MSPA on 4 February 2020, in which an active (10 kg hammer) and passive (ambient vibration) line acquisition with 24 low frequency vertical geophones (4,5 Hz). The geophones were connected to a seismograph that recorded the vibration.

Two linear acquisition lines were analysed: L1 and L2 (Figure 4.12 and Figure 4.13), with a length of 24 m and 36 m, respectively. The distances from the source and the first geophone for L1 and L2 were 1,0 m and 1,5 m, respectively. Both forward and reverse shots were recorded.

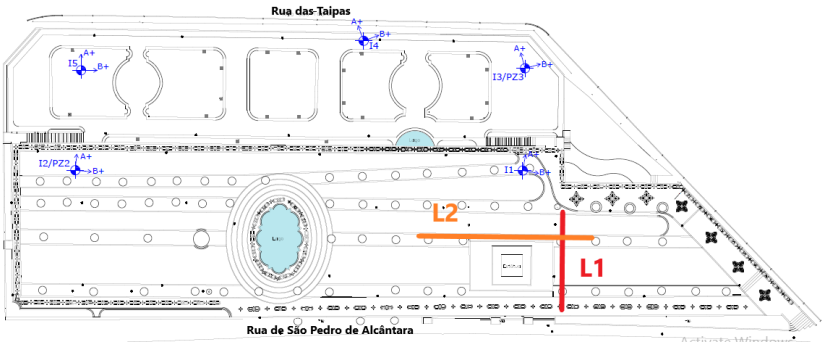

Figure 4.12. Position of the acquisition lines: L1 (in red) and L2 (in orange) (adapted from Geotest, 2011) (unscaled)

Figure 4.13. Acquisition line L1

After processing and inverting the data recorded, the V_S profile was obtained (Figure 4.14).

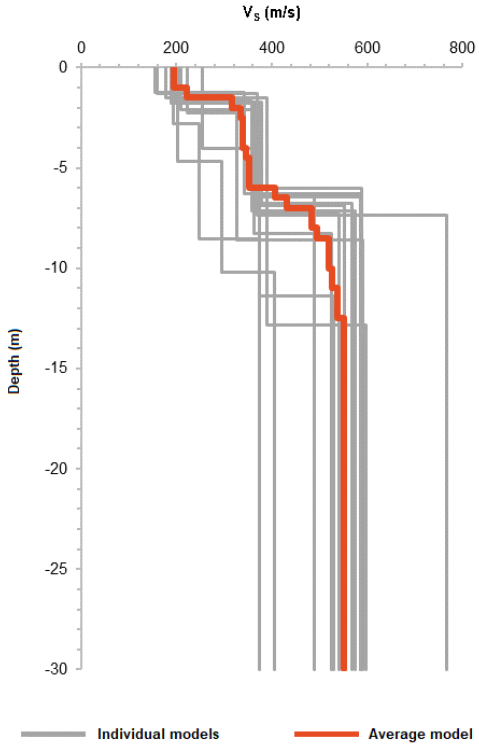

Figure 4.14. V_S profile of the ground (adapted from Oliveira, n.d.)

It is noticeable that the V_S tends to increase with depth, and three layers can be identified: the first layer goes from the surface until 1,5 m, with an average V_S of 200 m/s, the second layer until 7,0 m, with an average V_S of 350 m/s, and the third layer with no identified boundary, with an average V_S of 550 m/s.

Considering the geology of the site, two layers are be considered out of this model (Table 4.4): the first one with a depth of 7,0 m and an average V_S of 350 m/s that could represent landfill (it should be noted that the first 1,5 m can represent a more recent landfill, perhaps from the latest construction interventions, it will then not be considered for the geotechnical zonation), and the second one with an average V_S of 550 m/s that could correspond to the layer *Areolas da Estefânia*. A third layer that could

correspond to *Argilas e Calcários dos Prazeres* is not identified, either because it is deeper than 30 m or because there is no visible contrast between the *Areolas da Estefânia* and *Argilas e Calcários dos Prazeres* V_S.

Table 4.4. Layer characteristics considering the V_S profile

	Description	Average depth (m)	Average V_S $(\mathrm{m/s})$
Layer 1	Landfill	7	350
Layer 2	*Areolas da Estefânia*	>30	550

4.3.3. Geotechnical zonation

4.3.3.1. Comparison between the results of the conventional geotechnical survey and the surface waves method

Both with the conventional geotechnical survey and with the surface wave method, two layers were detected. A first layer composed by landfill and a second layer representing *Areolas da Estefânia*, that correspond to GZ1 and GZ2, respectively. Although no third layer was identified with the surface wave method, for the geotechnical characterization of the MSPA, GZ3 will also be considered, representing the layer *Argilas e Calcários dos Prazeres*, with no identifiable boundary. The characteristics of each GZ are presented in Table 4.5.

Table 4.5. GZ characteristics considering the data from the conventional geotechnical survey and the seismic surface wave method

	Description	Depth (m)	Median N_{SPT}	Average Vs (m/s)
GZ1	sandy clay with lithic fragments (landfill)	7 – 16,5	9	350
GZ2	silty and clayey sands, sandy silts (“Areolas da Estefânia”)	25,5 – 34,5	27	550
GZ3	limestone and silty clays (“Argilas e Calcários dos Prazeres”)	?	60	?

The permeability of GZ1 varies with the percentage of fine material present. Considering that GZ1 is mostly composed of sandy clays with lithic fragments, its permeability can be considered medium to low depending on the amount of fragments present. For GZ2, *Areolas da Estefania* are known to have medium to low permeability due to the sandy layers that constitute them. However the amount of sand present is very small (Figure 4.10), so the permeability of GZ2 can be considered low. For GZ3, *Argilas e Calcários dos Prazeres*, composed by limestone and silty clays is characterized by a low permeability.

4.3.3.2. Soil parameters

In this section, the geotechnical parameters of the different geotechnical zones are derived. The correlations proposed by Kulhawy & Mayne (1990) (Table 4.6 and Table 4.7) are used to estimate the shear strength angle, ϕ', as well as the undrained shear resistance, c_u.

Table 4.6. N versus $\bar{\phi}_{tc}$ relationships (adapted from Kulhawy & Mayne, 1990)

N Value (blows/ft or 305 mm)	Relative density	Approximate $\bar{\phi}_{tc}$*(º)
0 – 4	Very loose	< 28
4 – 10	Loose	28 – 30
10 – 30	Medium	30 – 36
30 – 50	Dense	36 – 41
> 50	Very dense	> 40

*$\bar{\phi}_{tc}$: triaxial compression shear angle

Table 4.7. Approximative c_u versus N relationship (adapted from Kulhawy & Mayne, 1990)

N Value (blows/ft or 305 mm)	Relative density	Approximate c_u (kPa)
0 – 2	Very soft	12,5
2 – 4	Soft	12,5 – 25
4 – 8	Medium	25 – 50
8 – 15	Stiff	50 – 100
15 – 30	Very stiff	100 – 200
> 30	Hard	> 200

Using equation (4.2), the initial shear modulus, G_0, can be determined, from which the initial shear strength, E_0, can be determined through equation (4.3).

$$E_0 = 2(1 + \upsilon)G_0 \tag{4.3}$$

Where υ is the Poisson's ratio.

Although GZ3 is not detectable in the surface wave survey, Laranjo (2013) preformed cross-holes tests between *Cais do Sodré* and *Praça do Comércio* (Figure 4.15), that intercepted the layer *Argilas dos Prazeres* at a depth between 26 and 38 m. The tests resulted in the V_S and the corrected N^*_{SPT} value, N^*_{60}, profiles (Figure 4.16). The N^*_{60} profile (Figure 4.16-a) shows similar results to the ones collected in the MSPA, which can lead to the conclusion that the layer *Argilas dos Prazes* has similar properties in all its extension. The properties determined by Laranjo (2013) are be used to determine the soil parameters of GZ3. Considering the average V_S in Figure 4.16.b, GZ3's V_S will be 650 m/s.

Figure 4.15. Location of Cais do Sodré and Praça do Comércio (yellow markers) compared to MSPA (pink marker) (adapted from GoogleEarth)

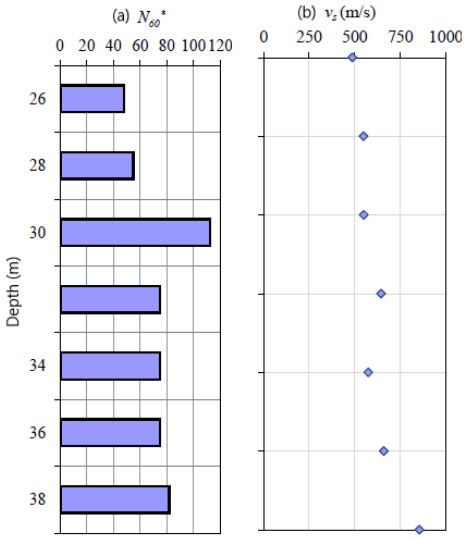

Figure 4.16. (a) N_{60}^{*} and (b) V_S profiles from *Argilas e Calcários dos Prazeres* (adapted from Laranjo, 2013)

Laboratory tests were also performed by Laranjo (2013) resulting in the classification of different samples (Figure 4.17) and the Atterberg limits (Table 4.8).

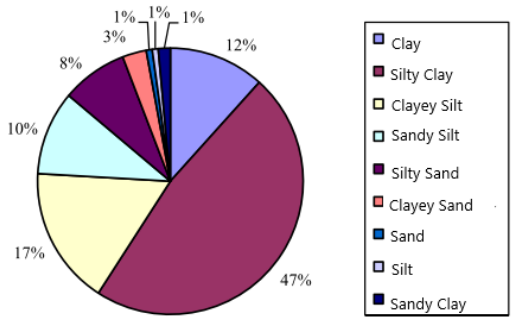

Figure 4.17. Percentages of samples with different classifications for the layer *Argilas e Calcários dos Prazes* (adapted from Laranjo, 2013)

Table 4.8. Statistics for the Atterberg limits of the samples from the layer *Argilas e Calcários dos Prazeres* (adapted from Laranjo, 2013)

	w_L (%)	w_P (%)	PI (%)
Minimum	19	13	3
Maximum	72	57	53
Average	40,8	20,5	20,7
Standard deviation	11,5	4,5	9,2
COV	28%	22%	45%

As concluded from the retrieved samples in the MSPA, Figure 4.17 confirms that *Argilas e Calcários dos Prazeres* is constituted mainly of silty clays (47%). The Atterberg limits (Table 4.8) present an average PI of ~21%, for GZ3 a PI of 20% will be used.

The soil parameters used for the analysis of ground movement of MSPA are presented in Table 4.9.

Table 4.9. Soil parameters

	GZ1	GZ2	GZ3
Field data			
Description	sandy clay with lithic fragments (landfill)	silty and clayey sands, sandy silts ("Areolas da Estefânia")	limestone and silty clays ("Argilas e Calcários dos Prazeres")
N^*_{SPT} median	9	27	60
V_S average (m/s)	350	550	650
γ (kN/m^3)	16	20	25
ρ (kN/m^3)	1,6	2,0	2,5
PI (%)	10	15	20
Data through correlations			
ϕ' (º)	30	35	40
c_u (kN/m^2)	80	200	360
G_0 (kN/m^2)	200 000	586 000	991 000
E_0 (kN/m^2)	480 000	1 410 000	2 377 000

5. Analysis of the wall displacements

This chapter aims to analyse the MSPA displacement pattern and identify possible cause(s). The wall 3D displacements were recorded in two periods: from 2010 until 2012 and from 2017 until 2018, using topographical marks. Inclinometers were also used to record lateral displacement with depth of the MSPA between 2011 and 2016 and in 2017. Finally, vertical displacements of the MSPA area were registered between 2015 and 2018, using the InSAR technique.

5.1. Topographical monitoring overview

To monitor the 3D displacements of the wall, sixteen topographical marks (green points in Figure 5.1) were installed in 2010. N1 to N6 in the East wall (Figure 5.2) and MO1 to MO10 in the North wall (Figure 5.3).

Twenty-six additional topographical marks were installed in 2017 (red points in Figure 5.1), T1 and T1B to T4 and T4B, and T22 in the upper wall, T5 to T12 in the lower wall and T13 to T21 in the wall from *Rua das Taipas*.

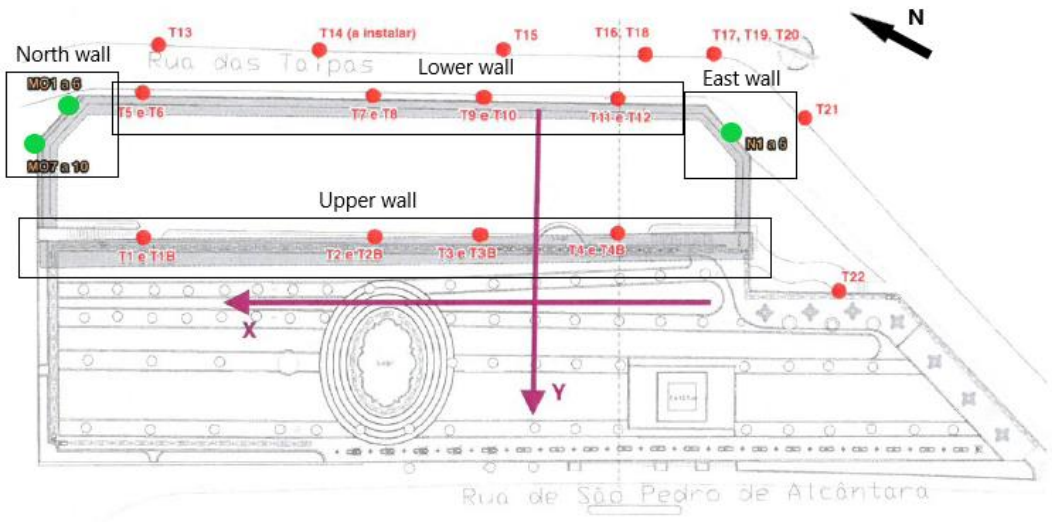

Figure 5.1. Position of the topographical marks (in green the marks installed in 2010, in red the marks installed in 2017) (adapted from Teixeira Duarte, S.A., 2017a) (unscaled)

Figure 5.2. Position of the topographical marks of the East wall (Teixeira Duarte, S.A., 2017a)

Figure 5.3. Position of the topographical marks of the North wall (Teixeira Duarte, S.A., 2017a)

The three directions in which the displacements were measured were longitudinal (x-direction in Figure 5.1), transversal (y-direction), and vertical (z-direction). The displacements measured are presented in Figure 5.4 to Figure 5.9, where the red dashed lines designated by CW corresponds to the period of construction works (between May and October 2017).

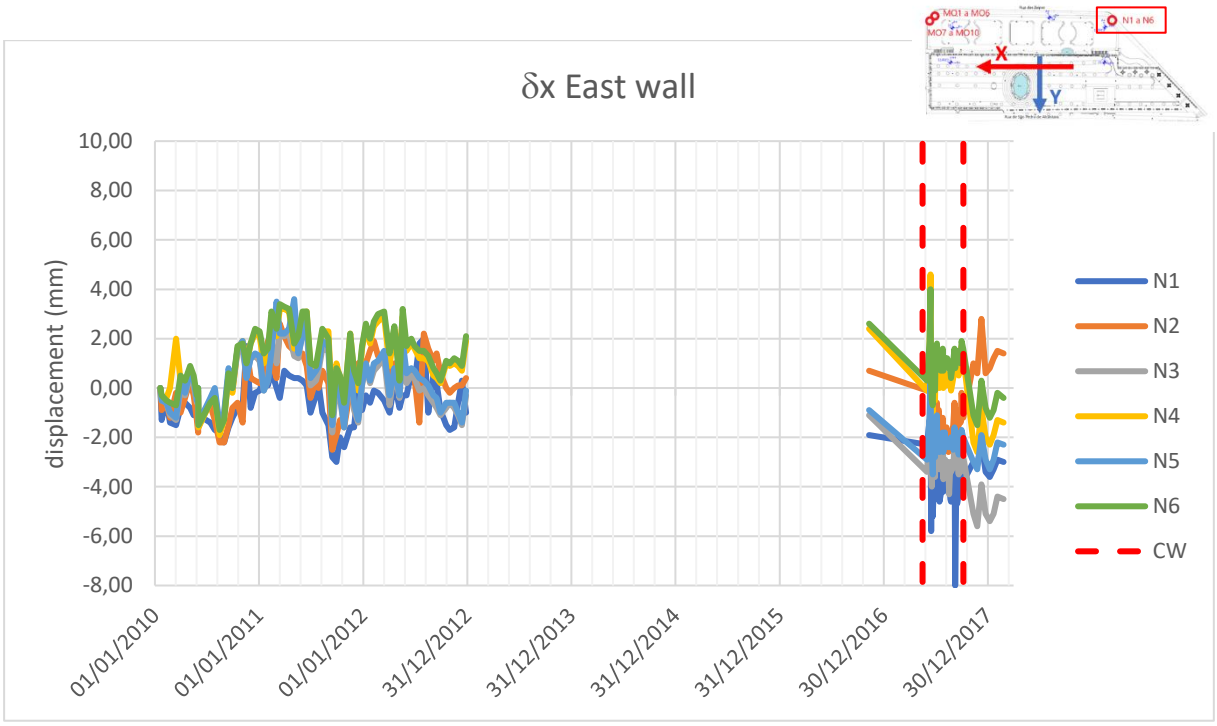

Figure 5.4. Longitudinal (δx) cumulative displacements of the East wall (adapted from Teixeira Duarte, S.A., 2017a)

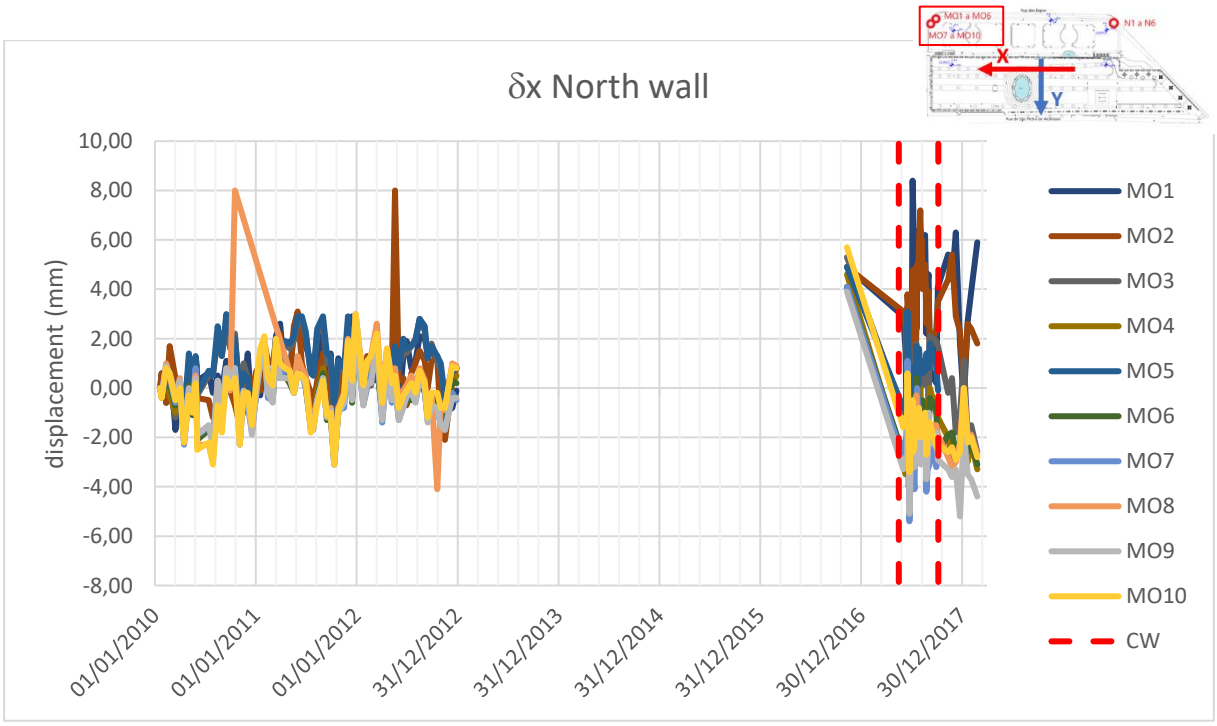

Figure 5.5. Longitudinal (δx) cumulative displacements of the North wall (adapted from Teixeira Duarte, S.A., 2017a)

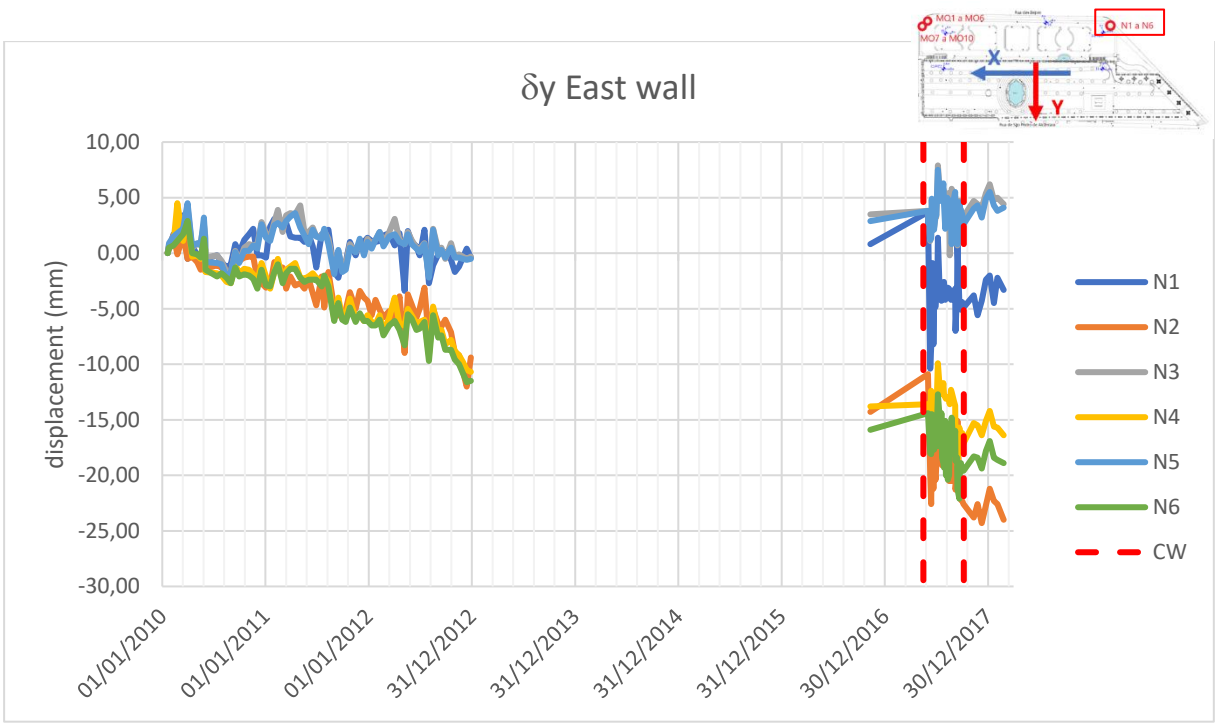

Figure 5.6. Transversal (δy) cumulative displacements of the East wall (adapted from Teixeira Duarte, S.A., 2017a)

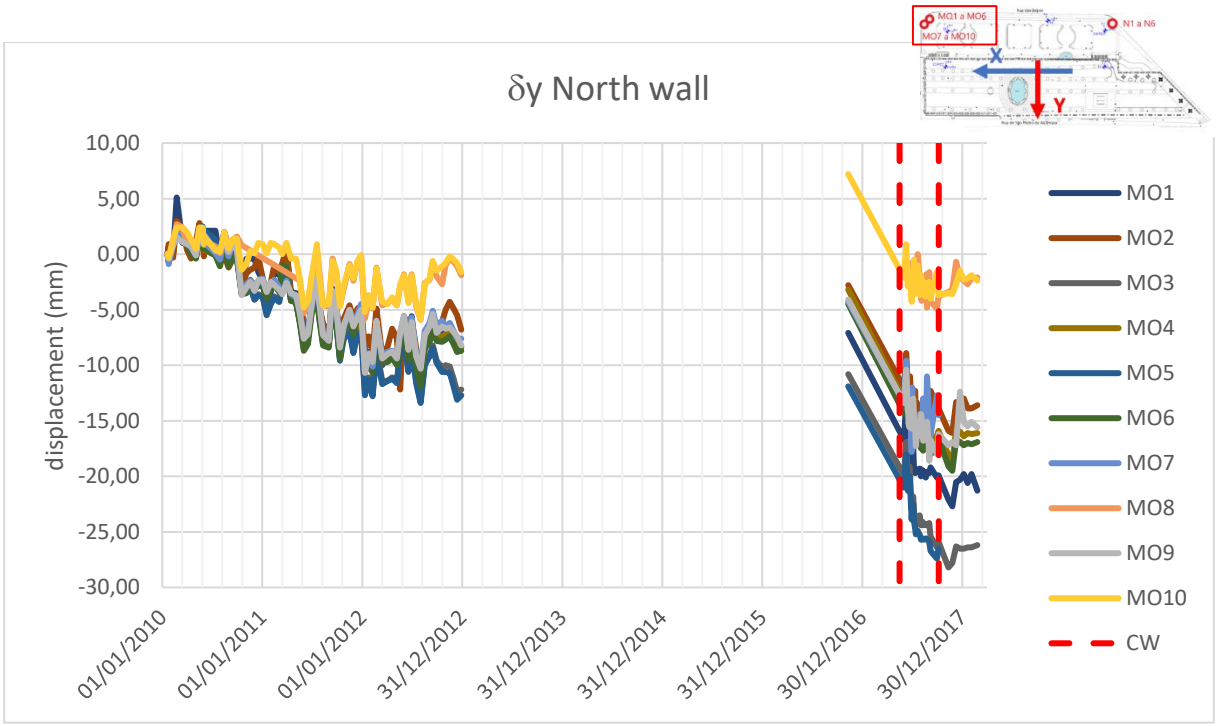

Figure 5.7. Transversal (δy) cumulative displacements of the North wall (adapted from Teixeira Duarte, S.A., 2017a)

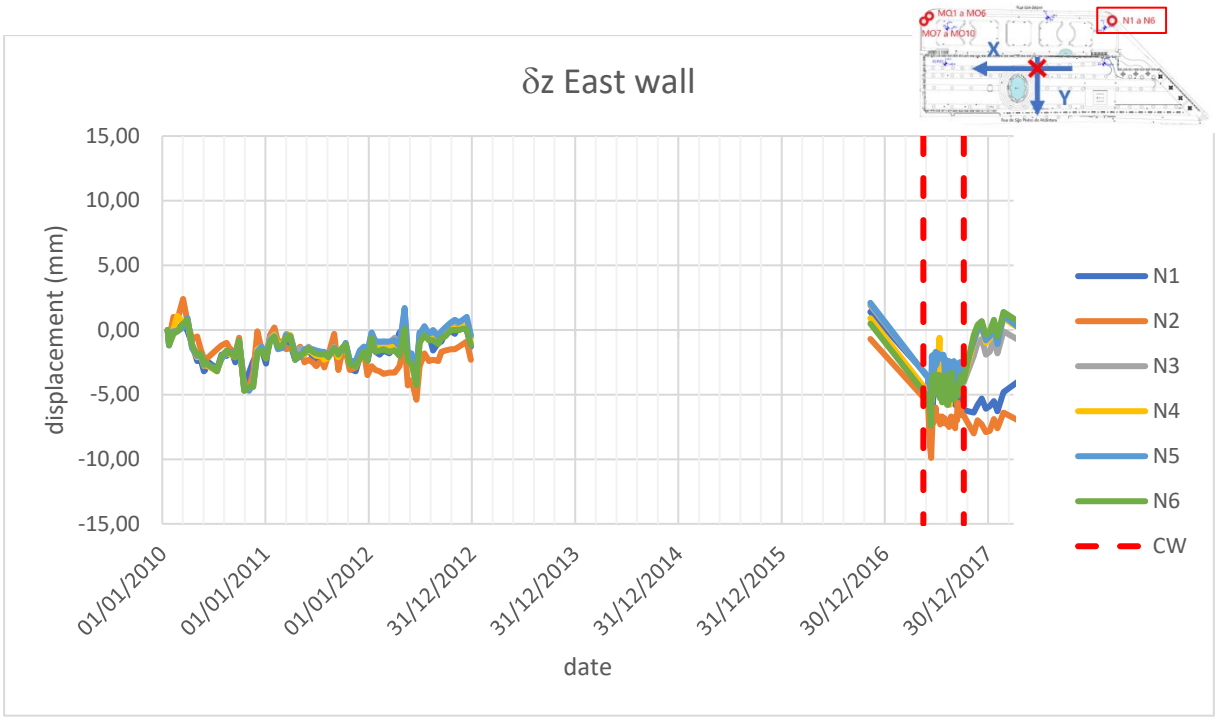

Figure 5.8. Vertical (δz) cumulative displacements of the East wall (adapted from Teixeira Duarte, S.A., 2017a)

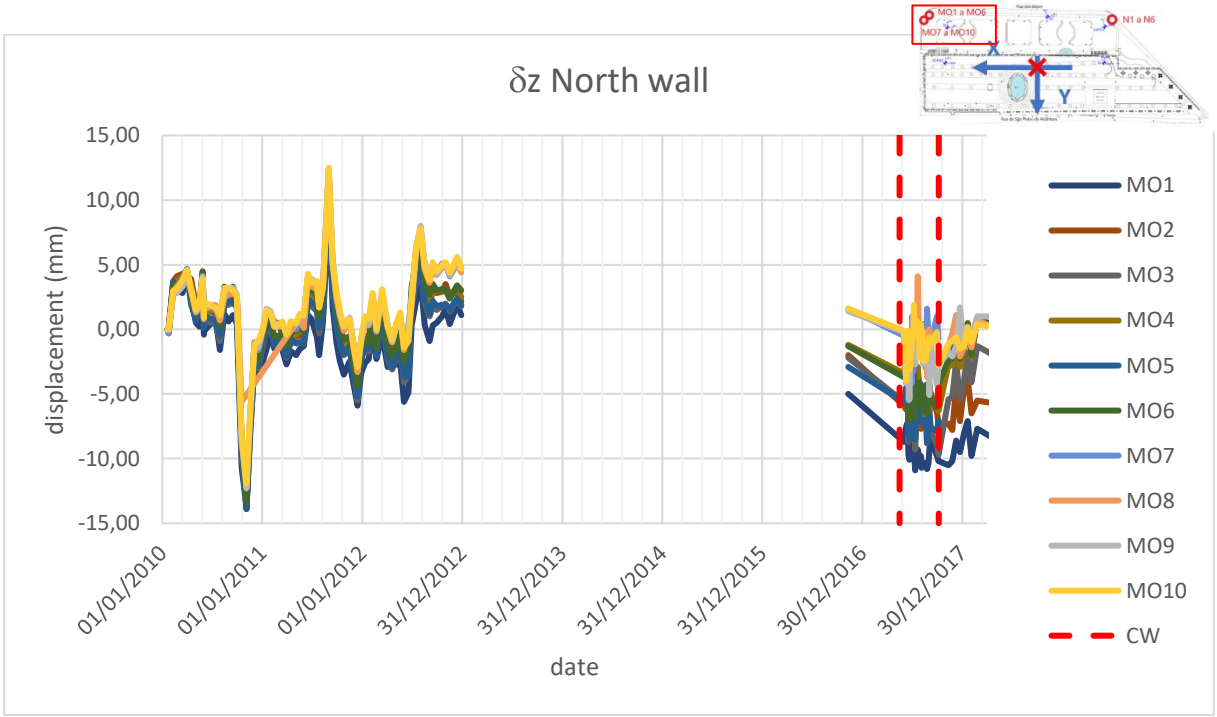

Figure 5.9. Vertical (δz) cumulative displacement of the North wall (adapted from Teixeira Duarte, S.A., 2017a)

To ease the identification of trends, a long-term moving average (LMA) was used to smooth the displacement time series, taking 3 values before and 3 after the instant in analysis, thus using $n = 7$ in equation (5.1):

$$\overline{\delta_t} = \frac{\delta_{t-\frac{n-1}{2}} + \cdots + \delta_t + \cdots + \delta_{t+\frac{n-1}{2}}}{n} \tag{5.1}$$

Where, $\overline{\delta_t}$ is the smoothed displacement at time t and δ_t is the registered movement at time t. The smoothed cumulative displacements are presented in Figure 5.10 to Figure 5.15.

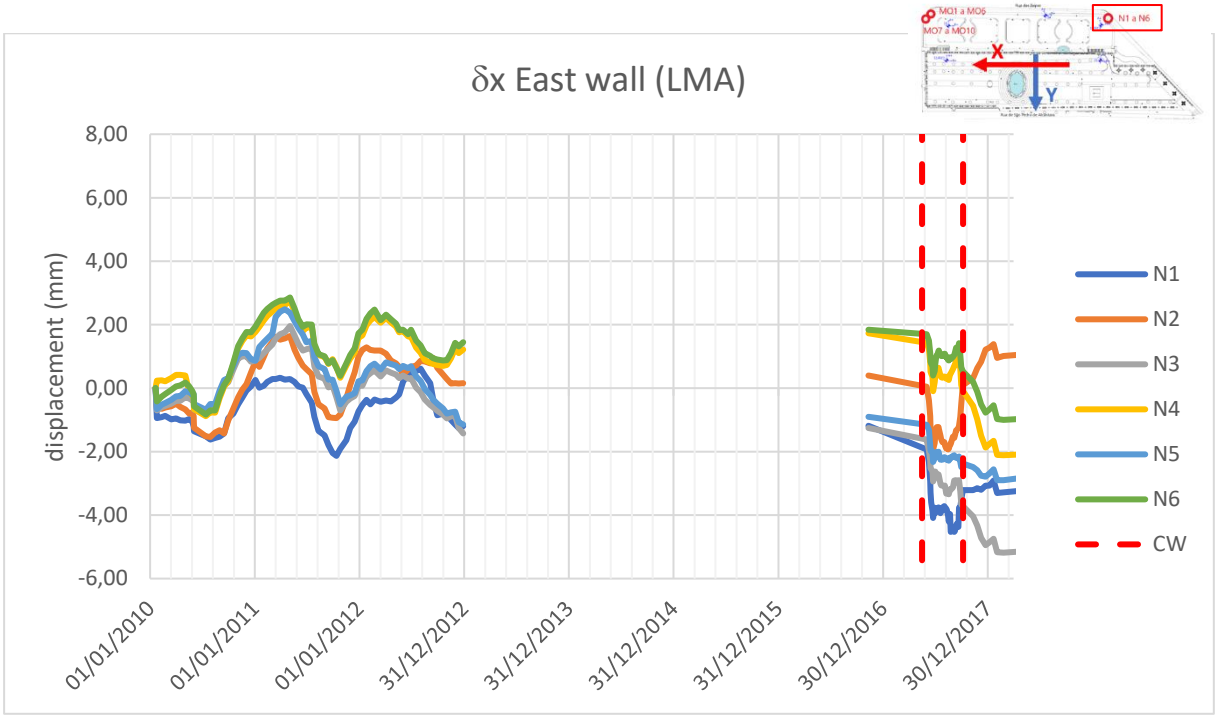

Figure 5.10. Longitudinal (δx) smoothed cumulative displacements of the East wall

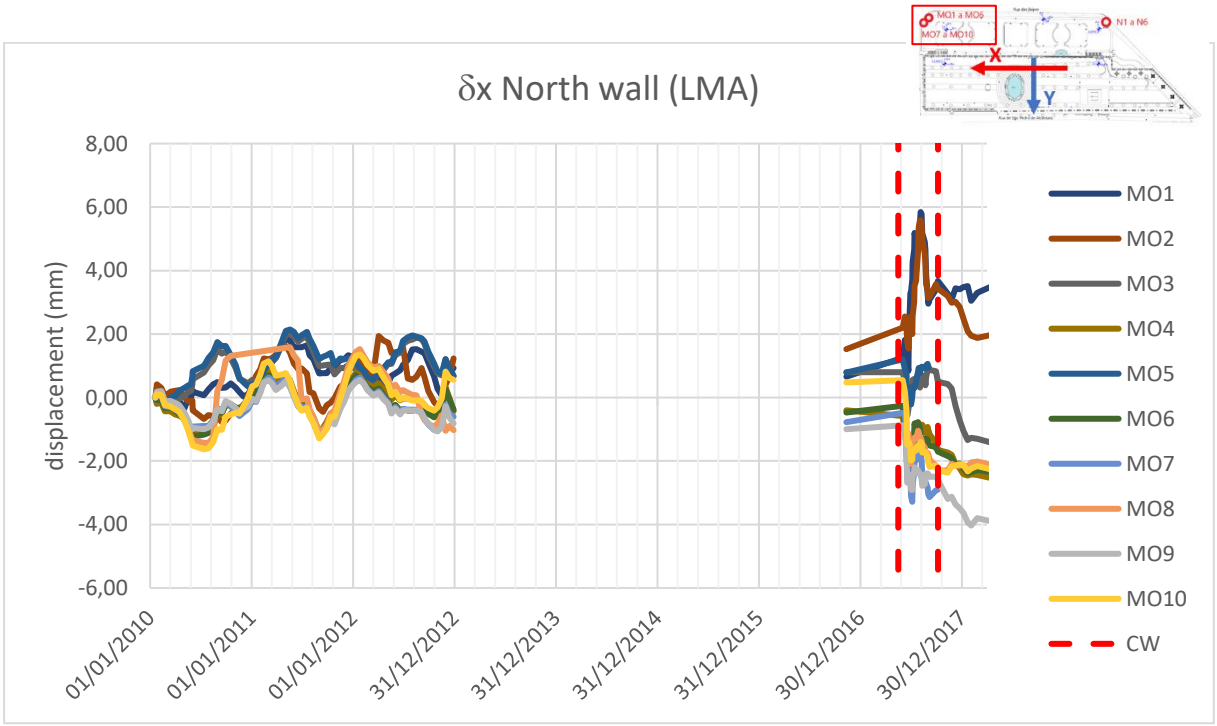

Figure 5.11. Longitudinal (δx) smoothed cumulative displacements of the North wall

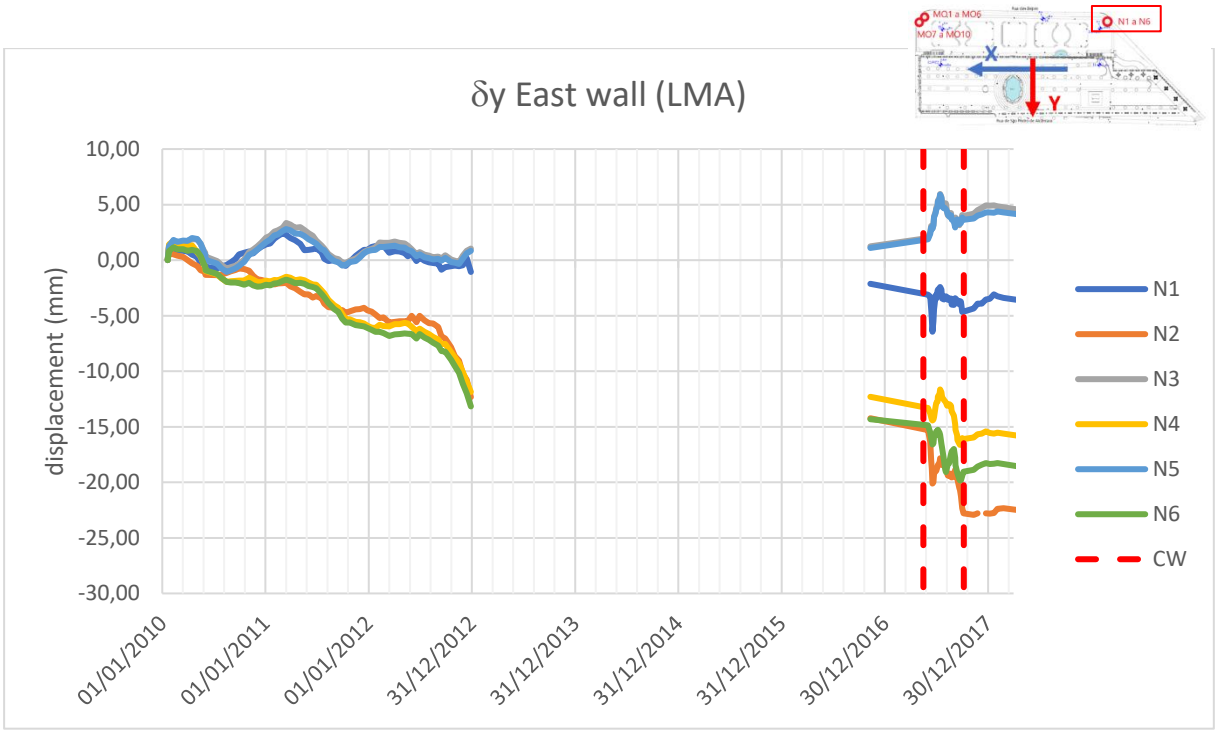

Figure 5.12. Transversal (δy) smoothed cumulative displacements of the East wall

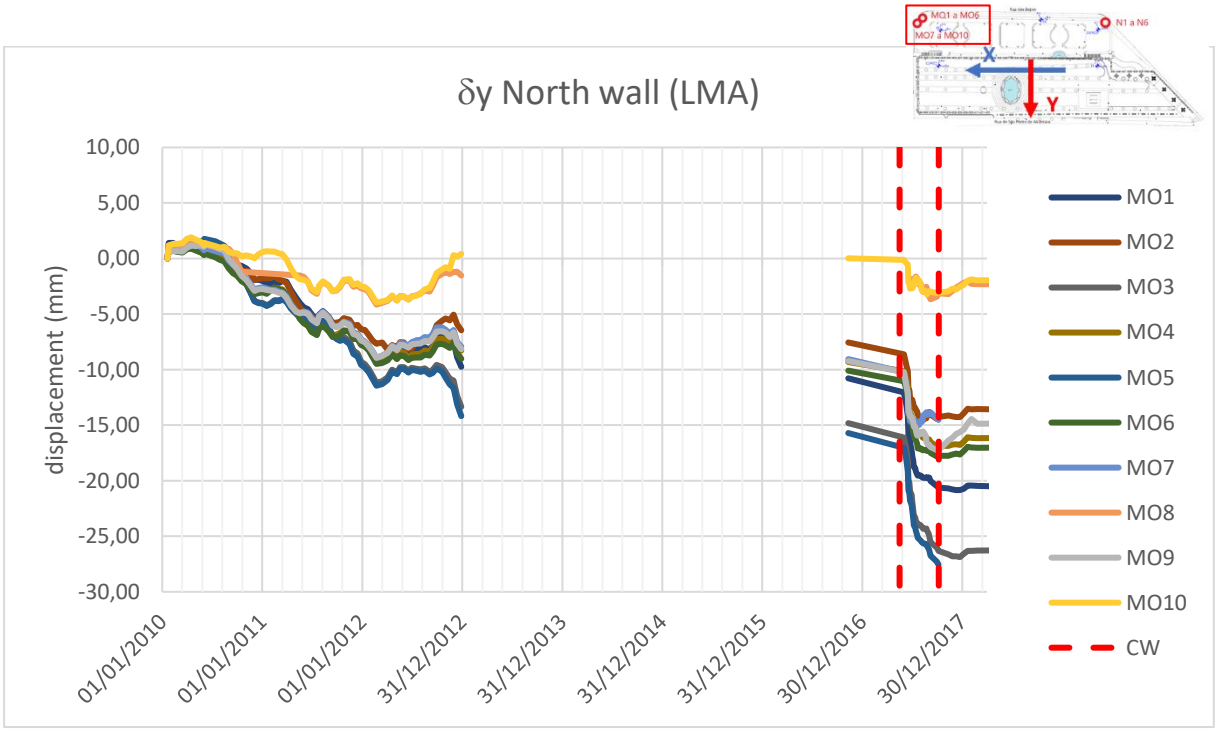

Figure 5.13. Transversal (δy) smoothed cumulative displacements of the North wall

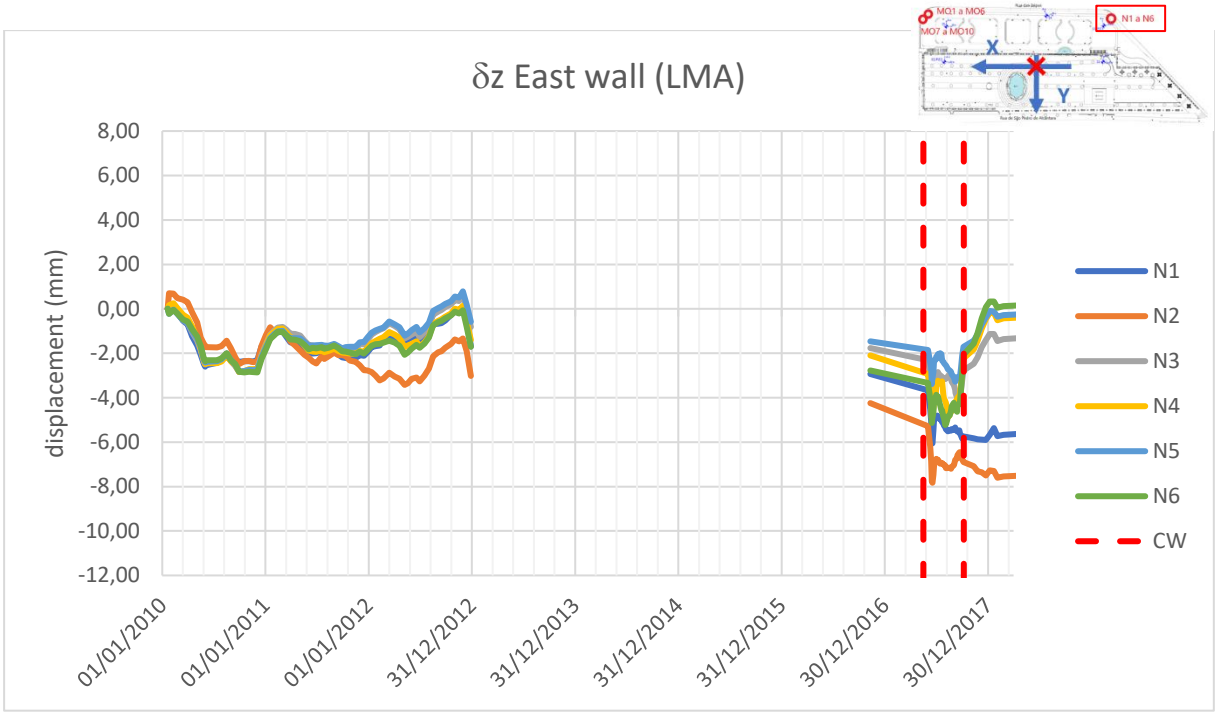

Figure 5.14. Vertical (δz) smoothed cumulative displacements of the East wall

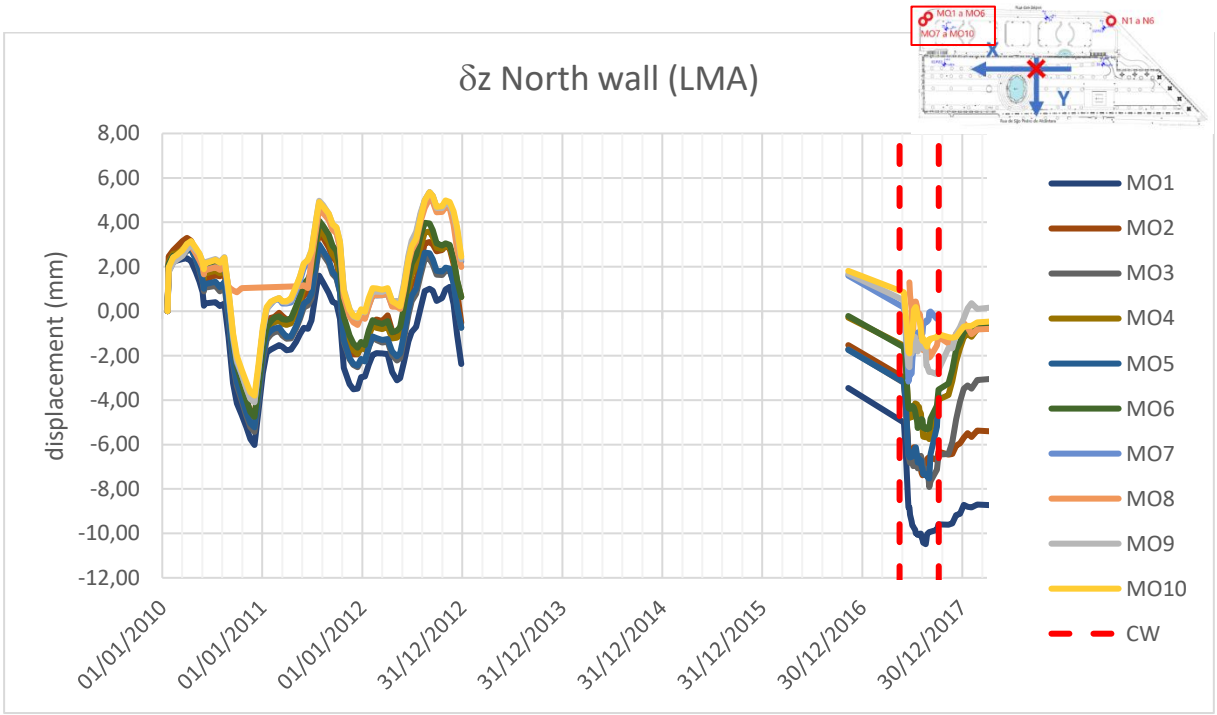

Figure 5.15. Vertical (δz) smoothed cumulative displacements of the North wall

5.1.1. Analysis of displacements from 2010 to 2012

For the longitudinal displacements (Figure 5.10 and Figure 5.11), there seems to be a sinusoidal variation with a period of one year and an amplitude of 1 mm, both in the East and North walls. The highest and lowest cumulative displacements are registered between February and May, and between August and October, respectively. Overall, the cumulative displacements at the end of the year are close to zero.

For the transversal displacements, three patterns of displacement can be identified: two in the East wall and one in the North wall. First, in the East wall (Figure 5.12), the points N1, N3 and N5 present a similar sinusoidal variation as described for the longitudinal displacements. Second, in the East wall (Figure 5.12), the points N2, N4 and N6 present an increasing displacement, with a maximum cumulative displacement of ~13 mm at the end of 2012. It should be noted that there seems to be an opening of the joint in the East wall as the displacements observed from one side of the joint (N1, N3 and N5) are stable, whereas the displacements observed on the other side of the joint show an increasing displacement (N2, N4 and N6) (Figure 5.17). Finally, in the North wall (Figure 5.13), all the points move outwards the wall, with a maximum cumulative displacement of ~14 mm at the end of 2012, except for MO8 and MO10 that seem to stabilize at the beginning of 2012. Just like the East wall there seems to be an opening of the joint in the North wall, as one side of the joint (MO1, MO3 and MO5) presents higher displacements than the other side (MO2, MO4 and MO6), the displacements also seem to be decreasing with depth, not in the joint, but in the wall itself (Figure 5.16).

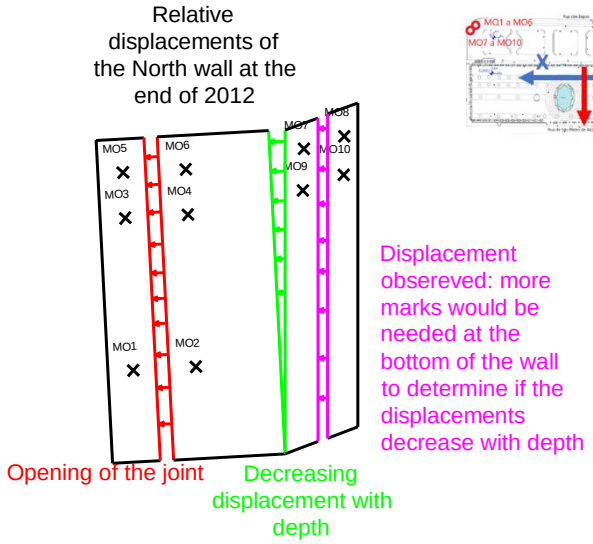

Figure 5.16. Lateral (δy) displacements observed in the North wall between 2010 and 2012

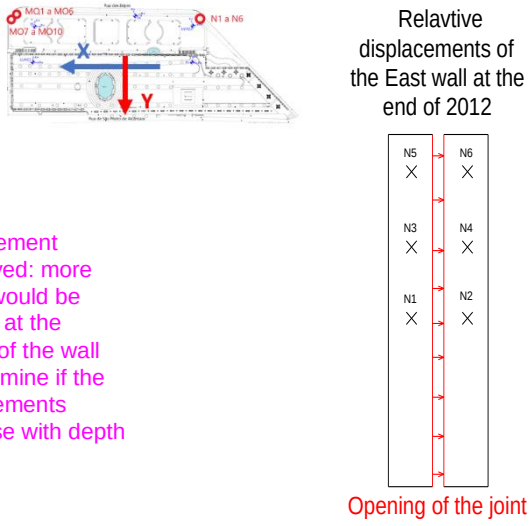

Figure 5.17. Lateral (δy) displacements observed in the East wall between 2010 and 2012

For the vertical displacements, of the East wall (Figure 5.14), there is no clear pattern of displacement, but they remains relatively stable. In the North wall (Figure 5.15), a sinusoidal pattern is noticeable, with the highest and lowest cumulative displacements occurring between August and September, and around December, respectively. Overall, the cumulative displacements at the end of

the year are close to zero. The vertical displacements could be represented, in average, with a period of one year and an amplitude of 3 mm.

Considering the cumulative displacements from 2010 to 2012, the MSPA seems to have seasonal variations of displacement. However, in the transversal direction, there is an increasing displacement that could indicate wall instability.

5.1.2. Analysis of displacements from 2017 to 2018

The displacements measured between 2017 and 2018, plotted in Figure 5.10 to Figure 5.15, are more irregular than the ones between 2010 and 2012, because it includes a single measurement before the construction works, and due to those works. Since there is no data from 2012 to 2017, it is not possible to determine if there was a trend change during this time interval or if this irregularity is only due to the construction works.

Even though a clear pattern of displacement could not be identified, after the end of the construction works, the displacements time history stabilized.

5.2. Analysis of the inclinometers and piezometers

Five inclinometers were installed in 2011, I1 to I5, in the SPT boreholes, S1 to S5 (Figure 5.18 and Table 5.1). Two of these inclinometers, I2 and I3, work simultaneously as piezometers, Pz2 and Pz3, respectively. This allows the monitoring of lateral displacements with depth, as well as the measurement of the piezometric levels.

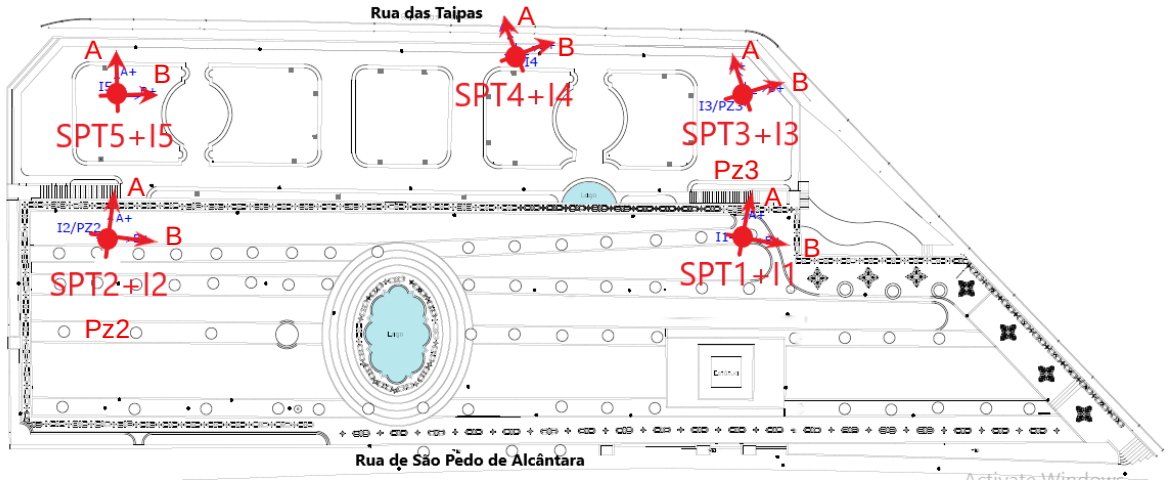

Figure 5.18. Position of the inclinometers (adapted from Geotest, 2011) (unscaled)

Table 5.1. Maximum depth of the inclinometers (Geotest, 2016)

Inclinometer	Maximum depth (m)
I1	32,0
I2	42,0
I3	37,0
I4	38,5
I5	35,0

The water level variations measured by the piezometers Pz2 and Pz3 are presented in Figure 5.19.

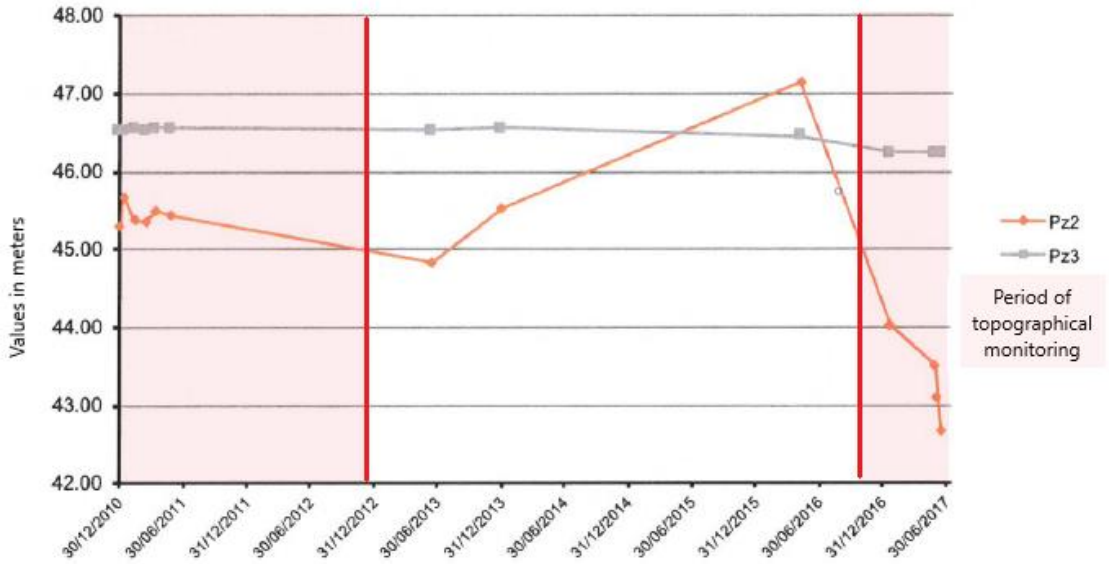

Figure 5.19. Water level variations in Pz2 and Pz3 (adapted from Teixeira Duarte, S.A., 2017a)

Overall, the water level is stable (Figure 5.19), with a higher variation between 2016 and 2017 (4 m). As the water level does not show any major variation during the time the increasing displacements started, it does not seem to be a trigger of movement for the MSPA.

The displacements measured by the inclinometers are compared with the information collected from the SPT tests (§4.3.1.1). The axes of the inclinometers A and B axes correspond approximately with the transversal and longitudinal directions of the wall. The inclinometers measure the lateral displacements that can be compared with the transversal and longitudinal displacements observed in the topographical monitoring, however, the positive displacements measured by the inclinometers correspond to negative displacements in the topographical monitoring.

First are presented the displacements measured by the inclinometers before the construction works (Figure 5.20 to Figure 5.24).

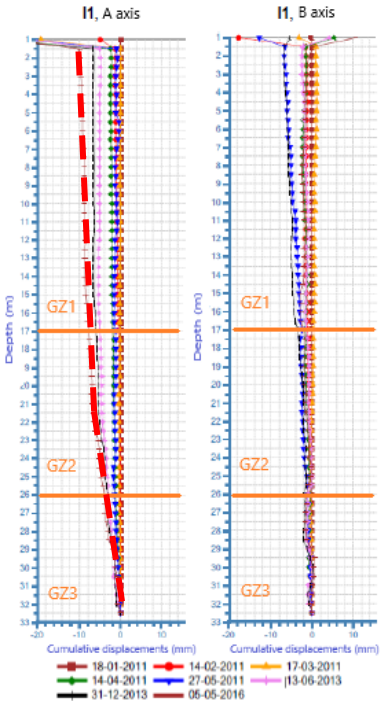

Figure 5.20. Transversal (A axis, δy) and longitudinal (B axis, δx) cumulative displacements of I1 from 2011 to 2016 (adapted from Geotest, 2016)

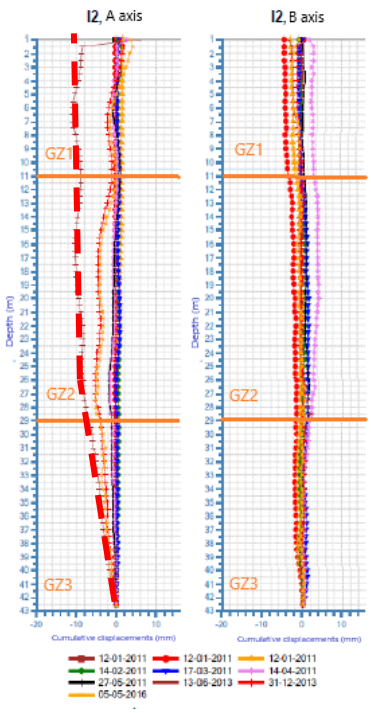

Figure 5.21. Transversal (A axis, δy) and longitudinal (B axis, δx) cumulative displacements of I2 from 2011 to 2016 (adapted from Geotest, 2016)

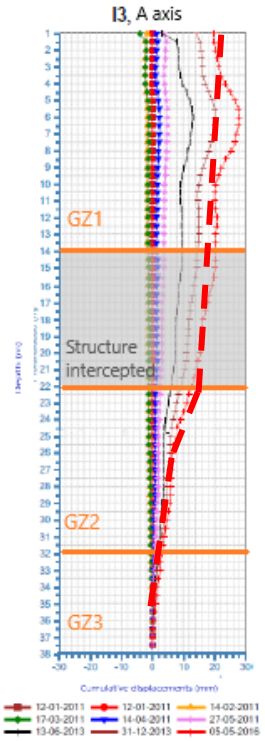

Figure 5.22. Transversal (A axis, δy) cumulative displacement of I3 from 2011 to 2016 (adapted from Geotest, 2016)

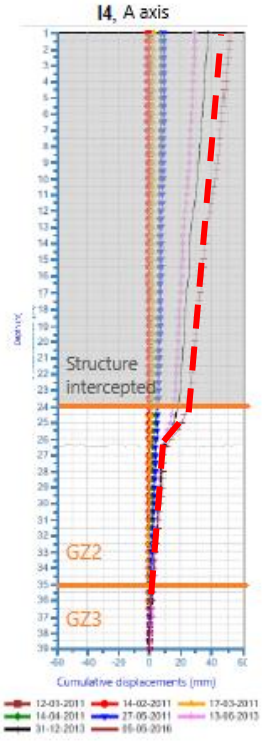

Figure 5.23. Transversal (A axis, δy) cumulative displacement of I4 from 2011 to 2016 (adapted from Geotest, 2016)

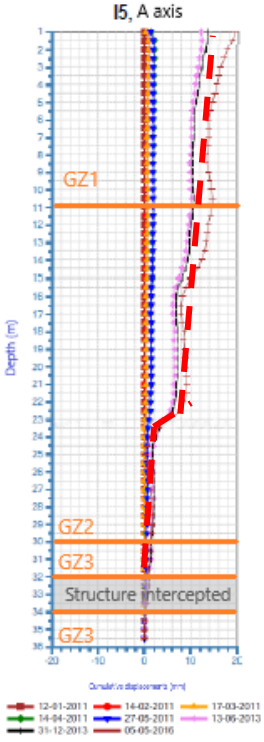

Figure 5.24. Transversal (A axis, δy) cumulative displacement of I5 from 2011 to 2016 (adapted from Geotest, 2016)

Starting with the inclinometers from the upper platform, I1 and I2 (Figure 5.20 and Figure 5.21), there are no relevant displacements in the longitudinal direction (B axis). In the transversal direction (A axis), both in I1 and I2, the maximum displacement is ~10 mm. These displacements tend to increase at the interface between GZ2 and GZ3 which could indicate a possible slip surface.

Analysing now the displacements from the lower platform, I3, I4 and I5 (Figure 5.22, Figure 5.23 and Figure 5.24), only the transversal direction (A axis) is presented, which is the direction that shows an increasing pattern of displacement in the topographical monitoring (§5.1). The displacements are larger than the ones observed in the upper platform, ~25 mm, ~50 mm and ~20 mm for I3, I4 and I5, respectively. In all cases an increment of displacement is observed at a depth of ~24 m that could be related to a slip surface. It should be noticed that for I3 and I4 it corresponds to the interface between the intercepted structures and GZ2, perhaps the structure is sliding. Finally, just like the inclinometers in the upper platform, displacements tend to increase between GZ2 and GZ3, but smother than at 24 m.

The displacements at the beginning of the construction works are also presented (Figure 5.25 to Figure 5.28), between May and June 2017. I5 was damaged and it is no longer used.

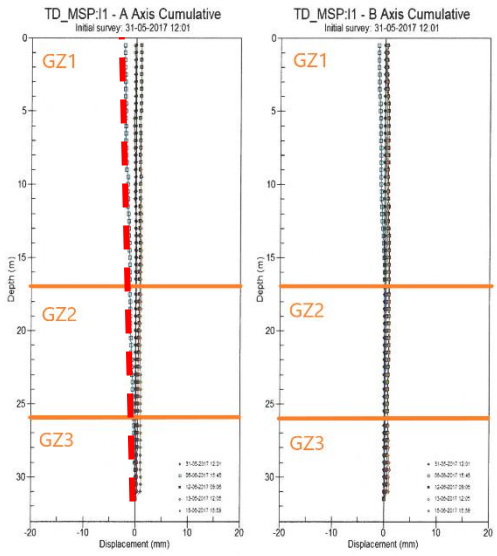

Figure 5.25. Transversal (A axis, δy) and longitudinal (B axis, δx) cumulative displacement of I1, from May to June 2017 (adapted from Teixeira Duarte, S.A., 2017a)

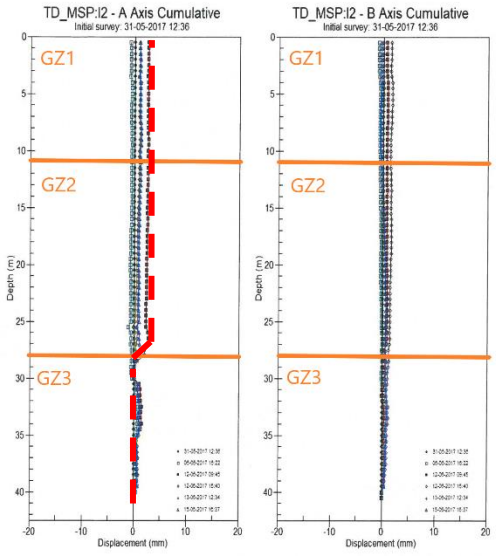

Figure 5.26. Transversal (A axis, δy) and longitudinal (B axis, δx) cumulative displacement of I2, from May to June 2017 (adapted from Teixeira Duarte, S.A., 2017a)

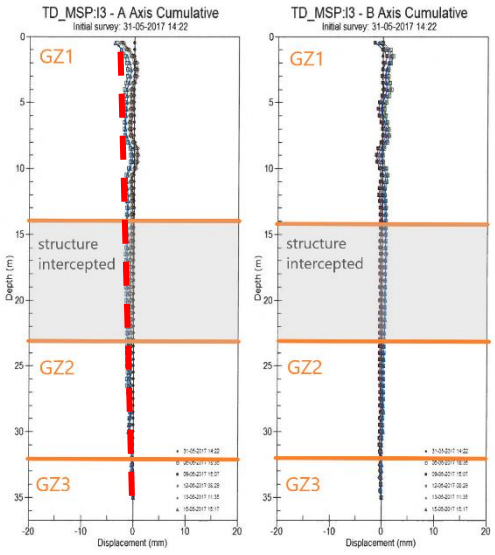

Figure 5.27. Transversal (A axis, δy) and longitudinal (B axis, δx) cumulative displacement of I3, from May to June 2017 (adapted from Teixeira Duarte, S.A., 2017a)

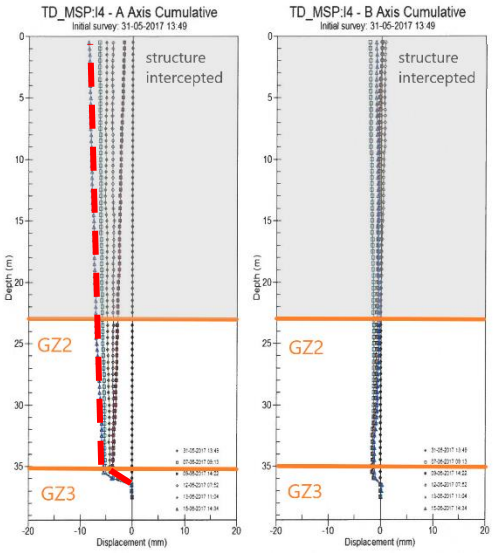

Figure 5.28 Transversal (A axis, δy) and longitudinal (B axis, δx) cumulative displacement of I4, from May to June 2017 (adapted from Teixeira Duarte, S.A., 2017a)

In the longitudinal direction (B axis) there are no relevant displacements in all inclinometers.

In the transversal direction (A axis), in the upper platform inclinometers, I1 and I2 (Figure 5.25 and Figure 5.26), no relevant displacements were measured (maximum displacement ~4 mm for I2). In the lower platform, I3 (Figure 5.27) reaches ~3 mm of maximum displacement in the transversal direction (A axis), the variation of displacements at 24 m are not observed, perhaps since the time of monitoring was not enough to the displacements develop. I4 (Figure 5.28) presents the largest cumulated displacement of all inclinometers, ~8 mm, as in the displacements registered from 2011 to 2016, I4 presents higher displacements then I3. Nevertheless, in all the inclinometers a sharp variation in the displacement measured at the interface level between GZ2 and GZ3 is more noticeable, especially in I2 and I4 (Figure 5.26 and Figure 5.28), emphasising the possibility of a forming slip surface at the interface between GZ2 and GZ3.

Globally, until 2016 the inclinometers show larger displacements at a depth of ~24 m for the inclinometers in the lower platform (Figure 5.22 to Figure 5.24), right below the intercepted structure in I3 and I4. Until 2017 all inclinometers present an increasing displacement at the interface between GZ2 and GZ3, these displacements are especially noticeable between May and June 2017 (Figure 5.25 to Figure 5.28). These can indicate two possible slip surfaces in formation that could explain the increasing displacements of the MSPA.

5.3. Analysis of InSAR data

InSAR is a technique that uses two or more synthetic aperture radar (SAR) images to generate maps of surface deformation or digital elevation. The InSAR technique allows the measurement of millimetre-scale changes over around 6 to 12 days.

Roque (2020) conducted a study on the displacement evolution through InSAR geodesy in the Lisbon area that registered displacements between March 2015 and March 2018. In the MSPA, eight points of displacement measurement were obtained (Figure 5.29). it should be noted that point 8 is not in the MSPA itself, but at the bottom of the lower wall.

Figure 5.29. InSAR points of displacement measurement in the MSPA (adapted from Roque, 2020)

Unfortunately there were no points from Roque (2020) work that coincide with the topographic marks, in order to fill the gap of information between 2012 and 2017 (Figure 5.29). Nevertheless, with the eight points obtained, three patterns of movement are observed: stable points (Figure 5.30), points with upwards displacements (Figure 5.31) and points with downwards displacements (Figure 5.32).

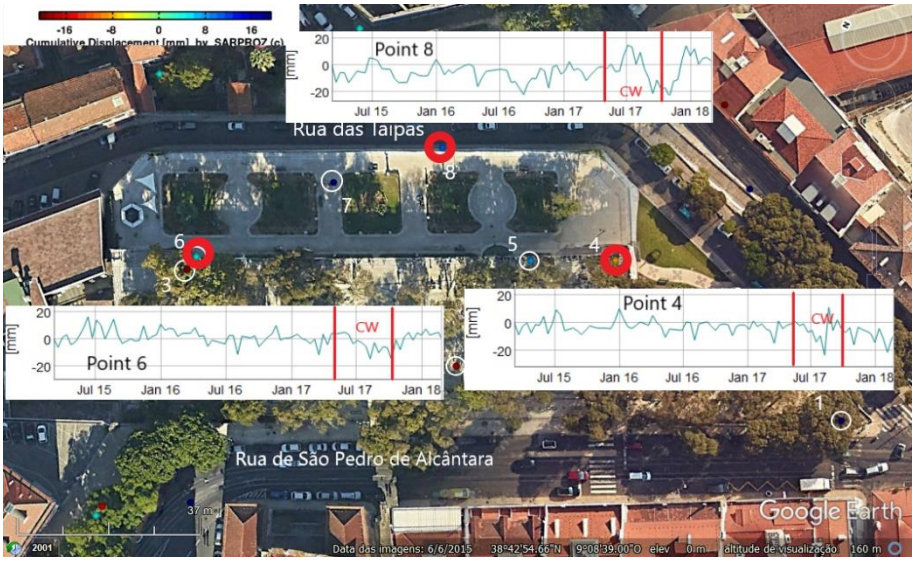

Figure 5.30. InSAR points of stable displacement (adapted from Roque, 2020)

Starting with the stable points (Figure 5.30), 4, 6 and 8 seem to be stable, they don't present any particular sign of instability, except maybe for point 8 that has larger variations in displacement, but those could be consistent with the seasonal displacements observed in the topographical monitoring (§5.1).

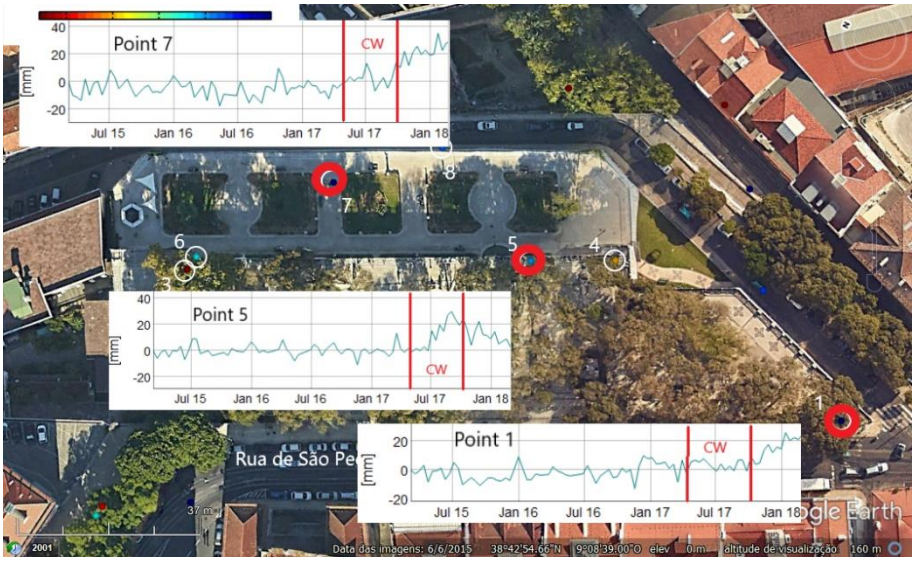

Figure 5.31. InSAR points of upwards displacement (adapted from Roque, 2020)

Now for upwards displacements (Figure 5.31), points 1 and 7 have an increasing displacement starting in September 2017 that could indicate some instability. The cumulative displacements in March 2018 are ~20 mm and ~30 mm for point 1 and 7, respectively. Point 5 also presents positive displacements at the end of June 2017, however, that tendency changes in September 2018 and the cumulative displacements tend to zero in March 2018, it would be important to have the cumulative displacements until today to understand if this trend change can be a sign of instability or if it has stabilized.

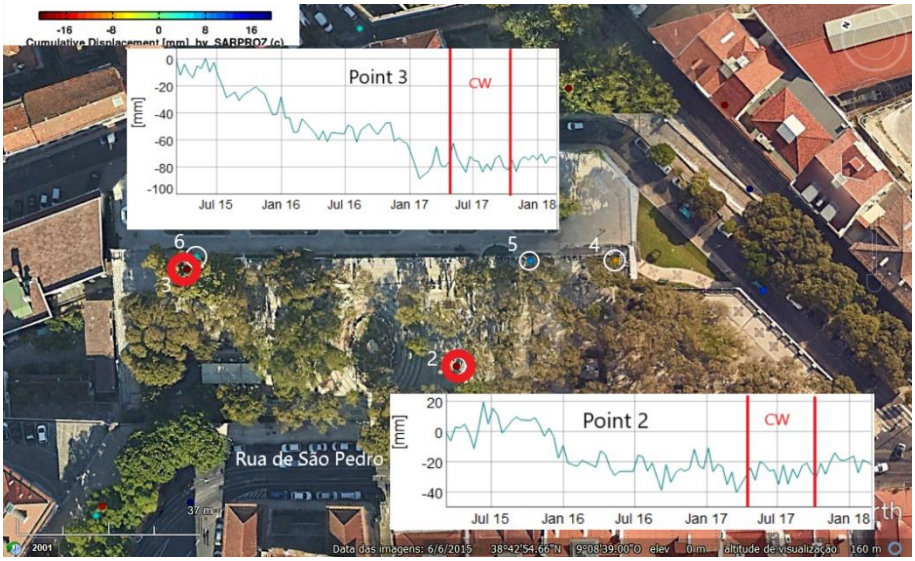

Figure 5.32. InSAR points of upwards displacement (adapted from Roque, 2020)

Finally for the downwards displacements (Figure 5.32), the larger displacement is registered in point 3 with ~75 mm, that had an increasing displacement starting in July 2015 and seemed to stabilize in March 2017. Point 3 is right next to point 6 that is considered as stable (Figure 5.30), which could indicate that point 3 is probably in the upper platform and point 3 in the lower platform. Point 2 also presents an increasing displacement, starting in October 2015 but seems to stabilise in May 2016.

The MSPA would benefit from InSAR monitoring. However, more points would be needed, especially in the retaining walls. From this analysis three points are potentially unstable in March 2018, but more data would be needed to determine if the MSPA is at risk. It should also be mentioned that InSAR technique provides the vertical displacements, and from the topographical monitoring (§5.1) it was determined that the unstable direction was the transversal direction and that the vertical direction did not present signs of instability. That being said, using the InSAR method could help assess if the MSPA had a risk of landslide but would maybe not be enough as it only provides the vertical displacement and few measuring points.

5.4. Analysis of possible displacement causes

From §2.3, it was determined that the triggering factors of a landslide can be divided in two groups: inherent factor and external factors. The aim of this section will be to analyse external factors for slope instability such as precipitation and earthquakes.

5.4.1. Precipitation

Precipitation can generate variations in the pore water pressure that may lead to the reduction of effective stresses, reducing the strength of the soil. To understand the effect of precipitation in the MSPA, the precipitation and the displacements are compared between 2010 and 2012. As the effect of rainfall is not instantaneous, the accumulated displacements were compared with the accumulated precipitation during two months (Figure 5.33 to Figure 5.38).

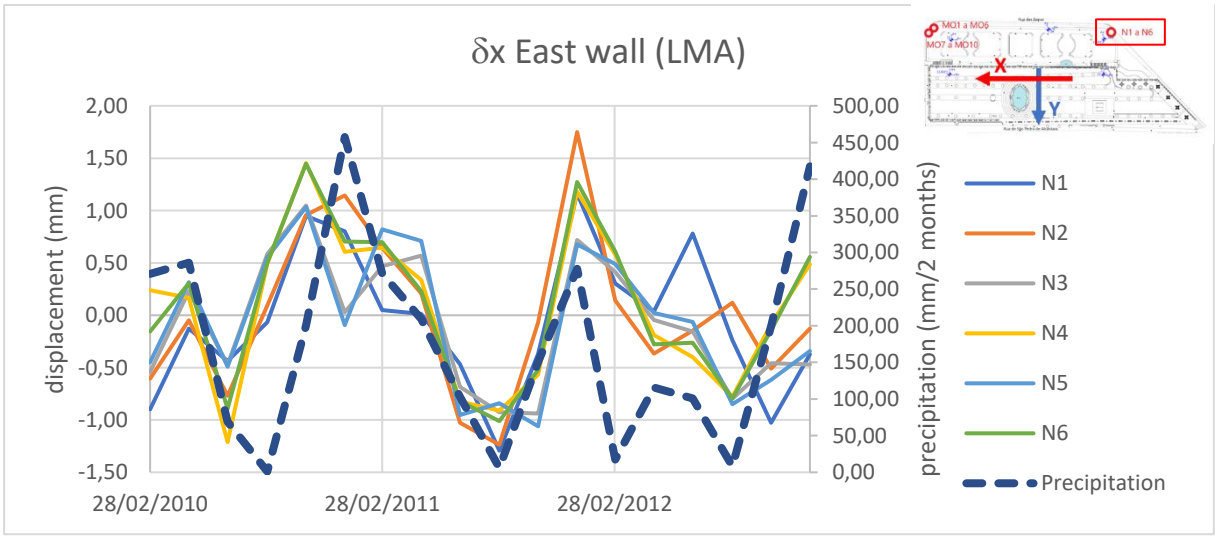

Figure 5.33. Accumulated longitudinal (δx) displacements of the East wall and precipitation for two months

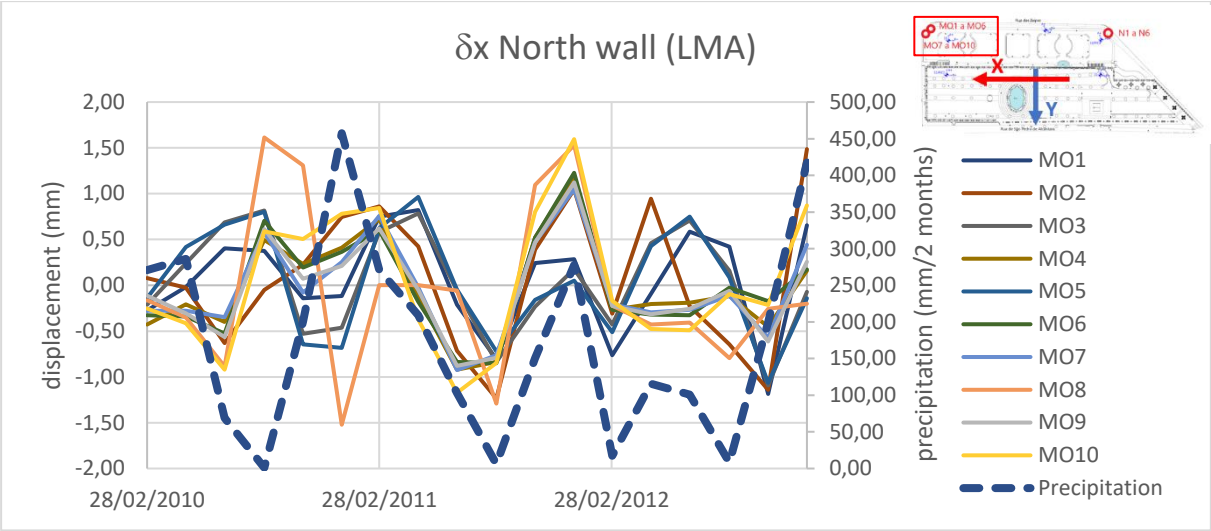

Figure 5.34. Accumulated longitudinal (δx) displacements of the North wall and precipitation for two months

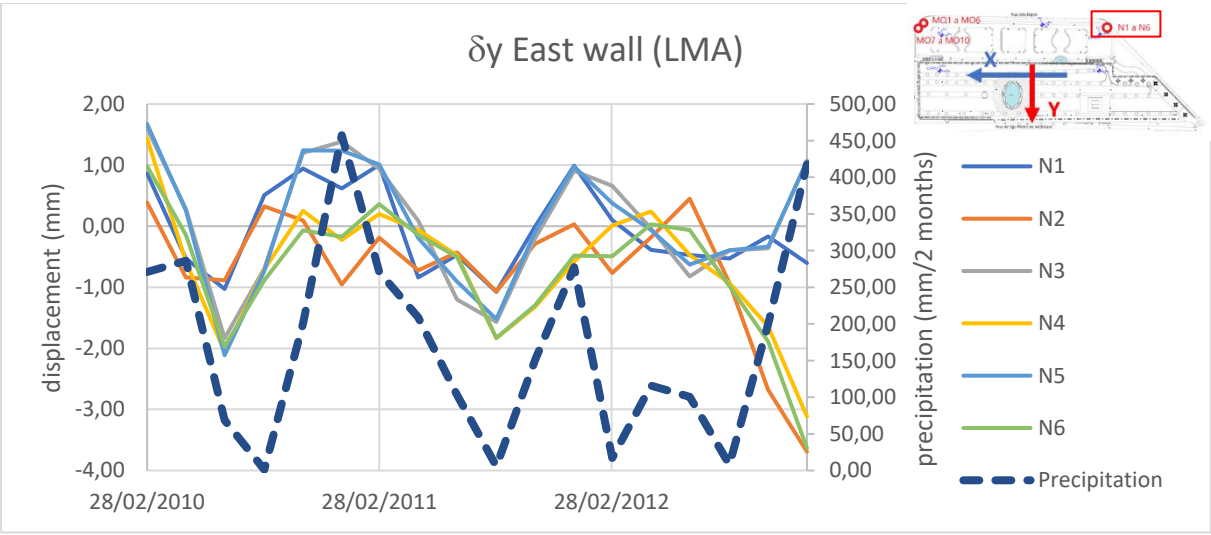

Figure 5.35. Accumulated transversal (δy) displacements of the East wall and precipitation for two months

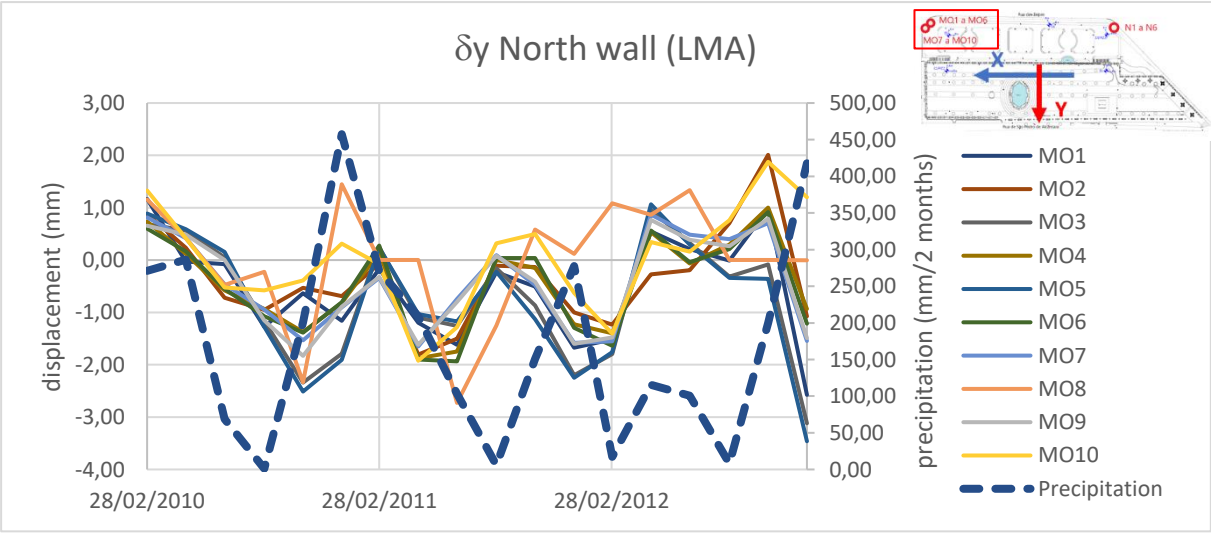

Figure 5.36. Accumulated transversal (δy) displacements of the North wall and precipitation for two months

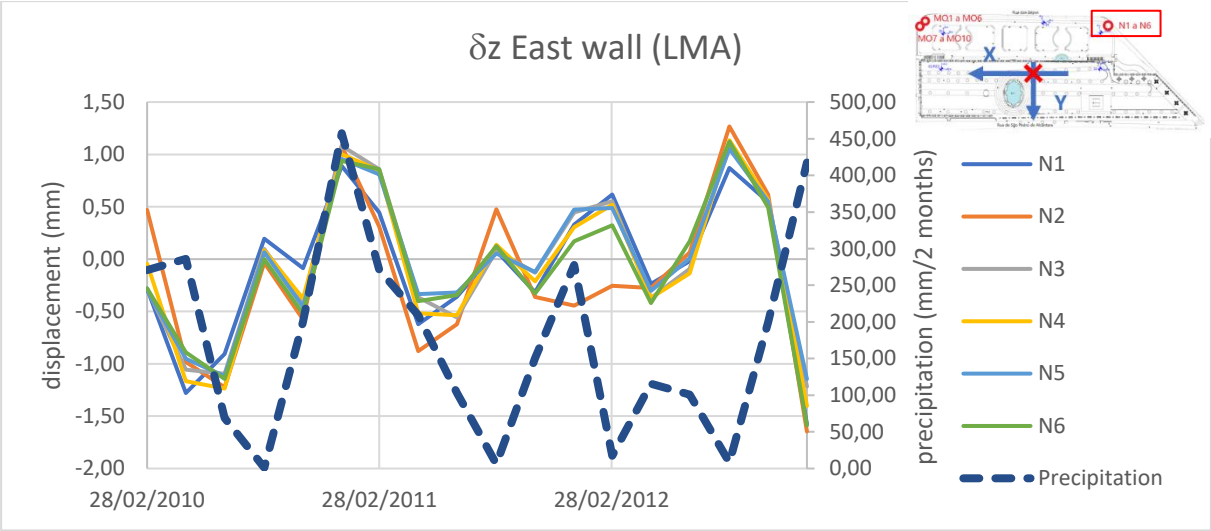

Figure 5.37. Accumulated vertical (δz) displacements of the East wall and precipitation for two months

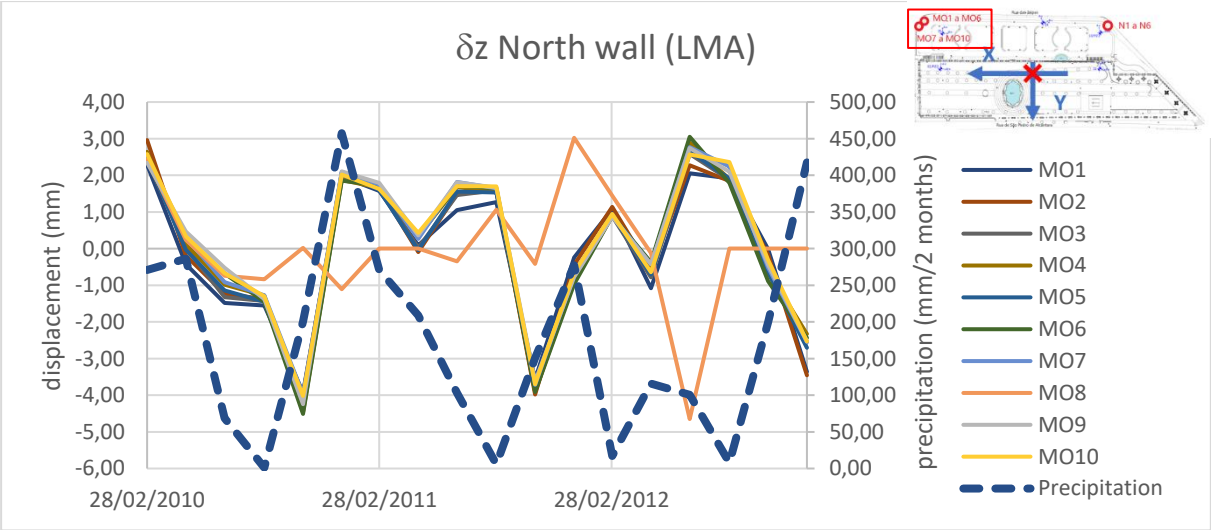

Figure 5.38. Accumulated vertical (δz) displacements of the North wall and precipitation for two months

In all cases the higher values of accumulated precipitation tend to coincide with the larger positive accumulated displacement and the lower accumulated precipitation coincide with the larger negative accumulated displacements. This could indicate a correlation between precipitation and displacements, where displacements increase with precipitation and reduce as the soil dries. The displacements are also plotted versus the precipitation, nevertheless, the data is too dispersed, and no strong correlation can be seen. For further details see figures in annex: Annex B to Annex D.

It can then be concluded that at least part of the seasonal component of the displacements captured by the topographical marks (§5.1) are due to volume variation induced by precipitation, but do not seem to explain the increasing pattern of displacements.

5.4.2. Earthquakes

In the period of analysis of the wall's displacement, a magnitude 4,2 earthquake occurred with a hypocentre at 42 km of the MSPA on the 17 August 2017 (Figure 5.39). The displacements at the time of the earthquake are presented in Figure 5.40 to Figure 5.42, where the instant of the earthquake is indicated by a vertical green dashed line, designated by E.

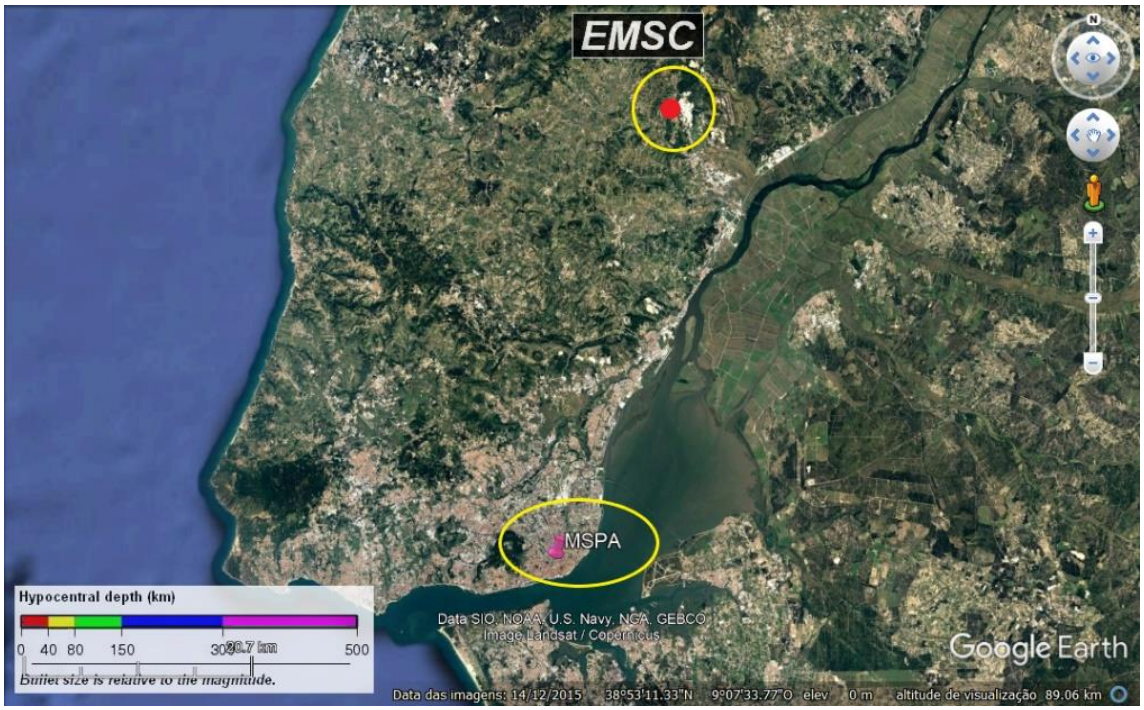

Figure 5.39. Position of the hypocentre of the 17/08/2017 earthquake (adapted from EMSC and GoogleEarth)

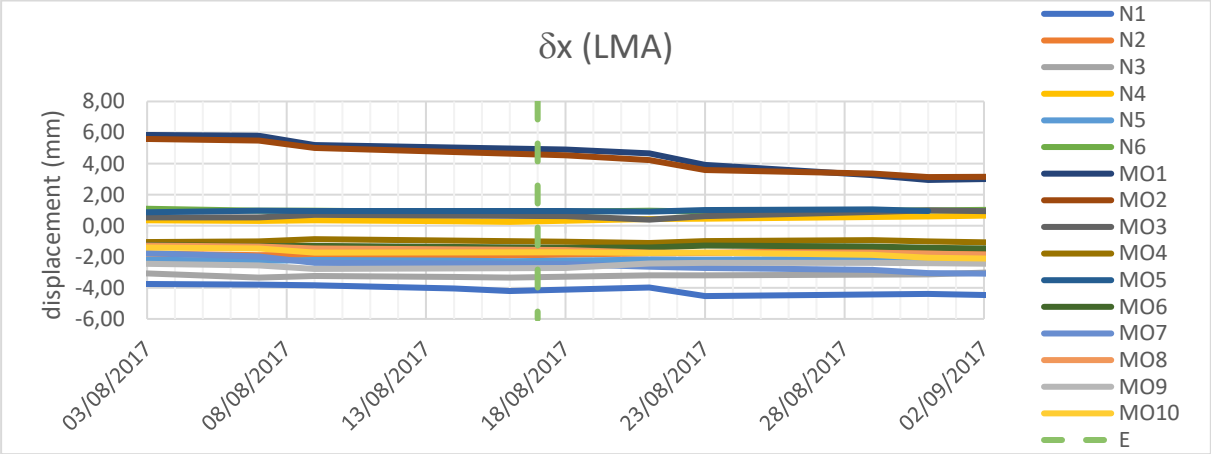

Figure 5.40. Longitudinal cumulative displacement at the time of the earthquake of 17/08/2017

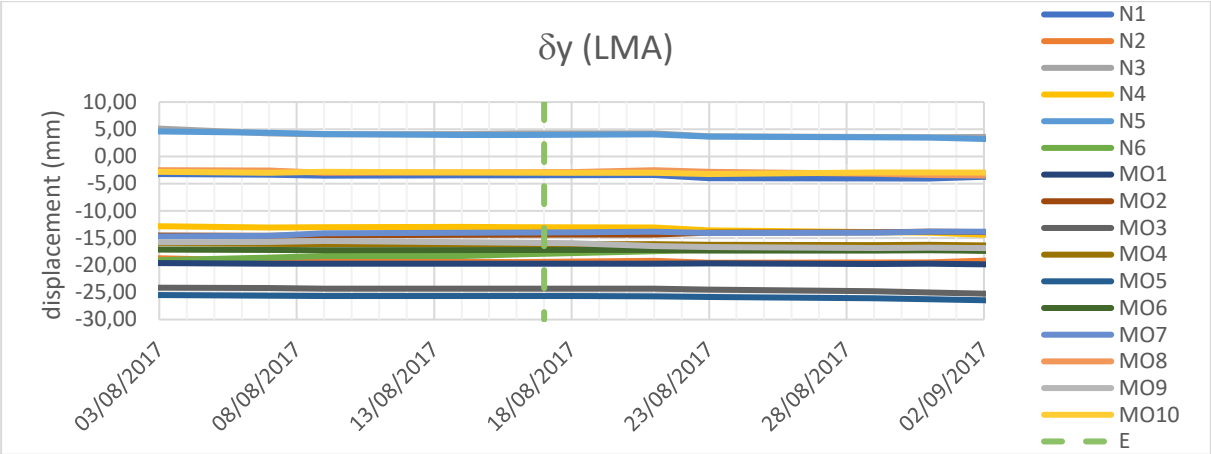

Figure 5.41. Transversal cumulative displacement at the time of the earthquake of 17/08/2017

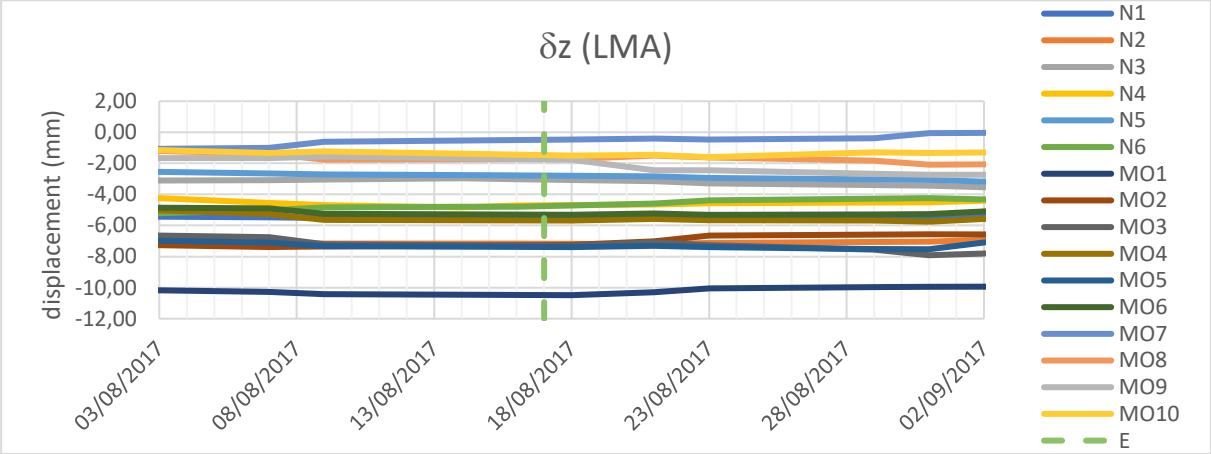

Figure 5.42. Vertical cumulative displacement at the time of the earthquake of 17/08/2017

In all directions (Figure 5.40 to Figure 5.42), the displacements show a straight line between the measurement made before and after the earthquake, meaning that the earthquake did not seem to have had an impact on the displacements measured.

5.5. Forecasting

The initial aim of this dissertation was to use the displacements measured by satellite to fill the gap between 2012 and 2016 of the topographical monitoring, in order to understand if the trend observed until 2012 changed or not and predict whether the MSPA presented a risk of landslide using landslide forecasting methods. As this line of work could not be concluded due to external reasons, the Fukuzono (1985) method is used for the topographical monitoring between 2010 and 2012. The Fukuzono (1985) method is used as it is the method that presented better results (§3).

For this analysis only the displacements of the transversal direction are be used, as it is the only direction that presented a pattern of increasing displacement. Two points of each wall (North and East) that present the larger cumulative displacement were selected for this analysis, MO5 and MO3 for the North wall (~11 mm for both), and N6 and N4 for the East wall (~10 mm and ~9 mm, respectively). As this analysis aims to predict a time of failure, a different LMA was used to smooth the displacement time

series, taking 6 values before the instant in analysis, $n = 7$ in equation (5.2), not letting the values after the instant in analysis interfere with the prediction.

$$\overline{\delta_t} = \frac{\delta_{t-n} + \cdots + \delta_t}{n} \tag{5.2}$$

Where, $\overline{\delta_t}$ is the smoothed displacement at time t and δ_t is the registered movement at time t. The smoothed cumulative displacements of N4, N6, MO3 and MO5 are presented in Figure 5.43.

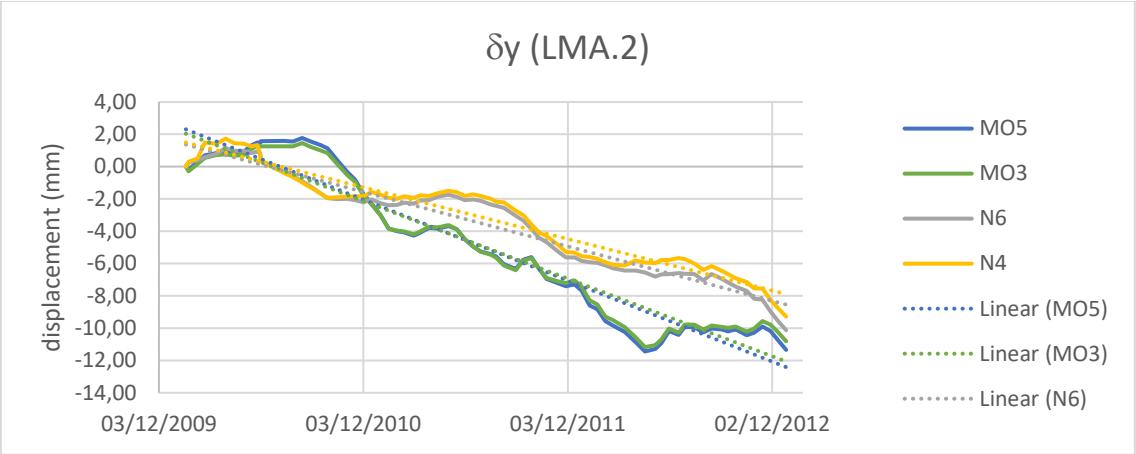

Figure 5.43. Smoothed transversal cumulative displacement of N4, N6, MO3 and MO5 using equation (5.2)

In Figure 5.43 the increasing displacements can clearly be seen, their trend is highlighted by trend lines. Additionally, seasonal variations in the displacement curves of N4 and N6 (grey and yellow lines in Figure 5.43) can also be seen. For MO3 and MO5 (blue and green lines in Figure 5.43), there are no clear seasonal variations. However, both points (MO5 and MO3) present the same progress, there is an increasing displacement starting in September 2010 that seems to stabilize in June 2012 and seems to return to an increasing trend of displacement in November 2012.

As the parameters A and α of the Fukuzono (1985) method (equation 3.4) are unknown, $\alpha = 2$ is considered to perform a linear regression to determine a possible time of failure. To start the inverse velocity is plotted in Figure 5.44.

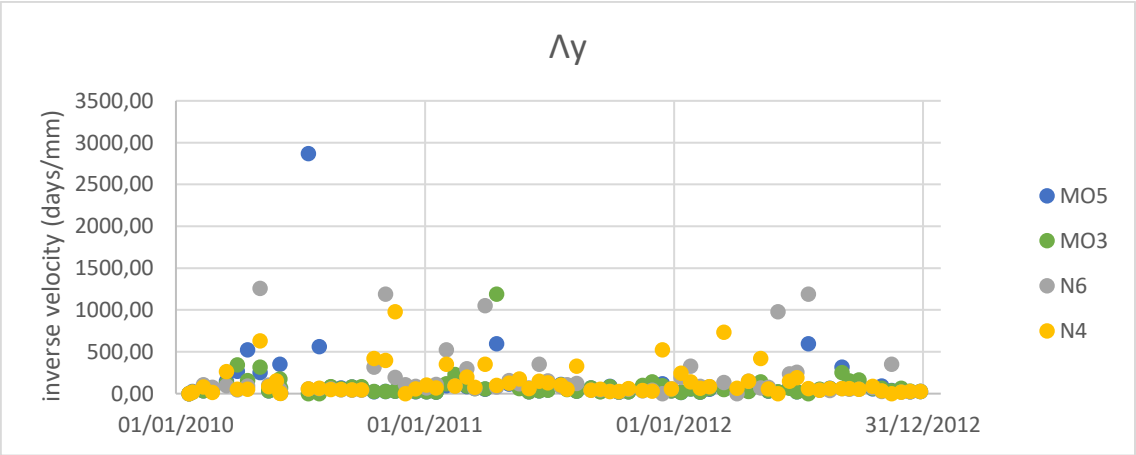

Figure 5.44. Inverse velocity of N4, N6, MO3 and MO5 from 2010 to 2012

In Figure 5.44 it is hard to determine the patterns of decreasing inverse velocity, which is why the inverse velocities from December 2011 to December 2012 are plotted in Figure 5.45 to Figure 5.48: to capture the time where MO5 and MO3 present the higher increase of displacement and one period of the sinusoidal curve described by N6 and N4. The points where a decreasing trend of the inverse velocity at the end of the measurements is observed are highlighted in red, these decreasing trends are observed between two and five months before the end of the time series, depending on the point considered.

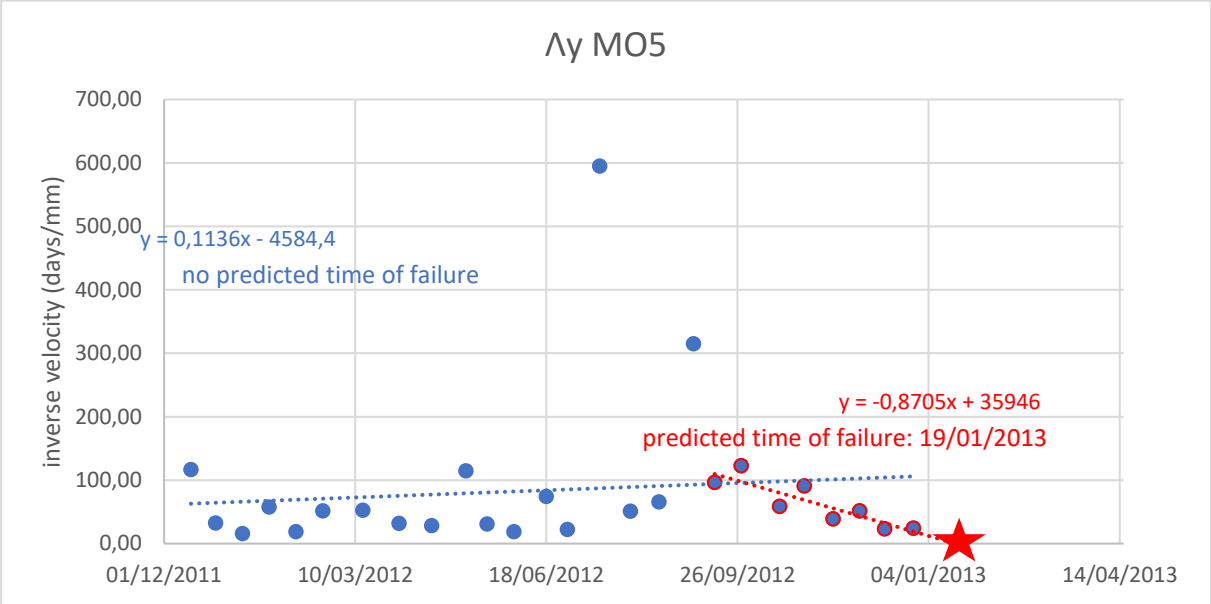

Figure 5.45. Inverse velocity of MO5 from December 2011 to December 2012[2]

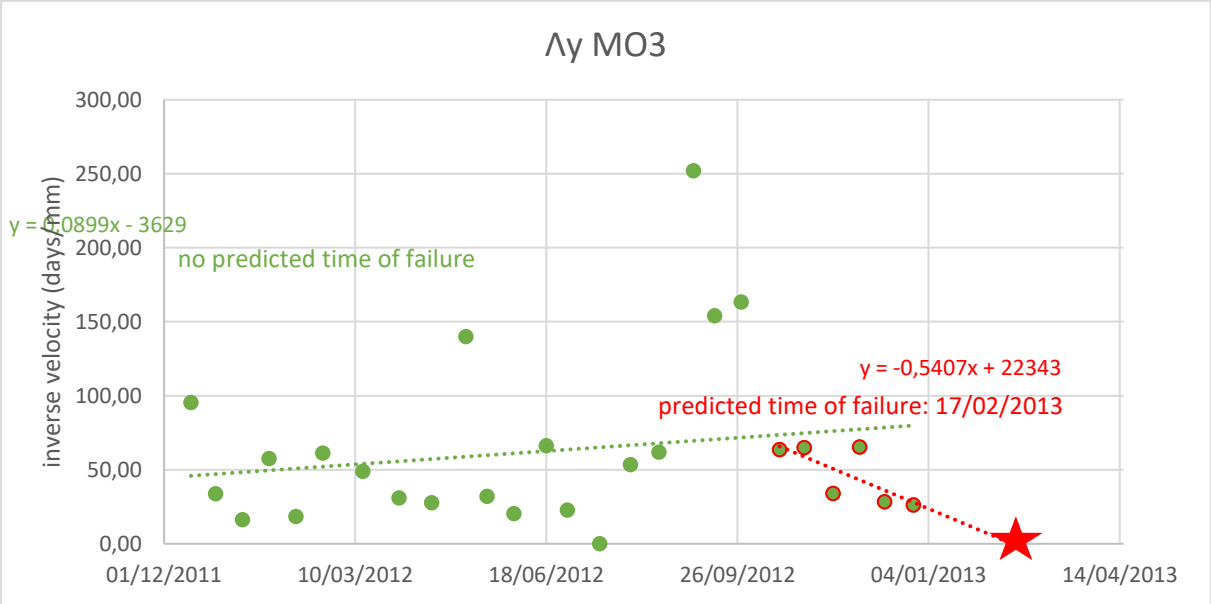

Figure 5.46. Inverse velocity of MO3 from December 2011 to December 2012[2]

[2] 01/12/2011 corresponds to 40878

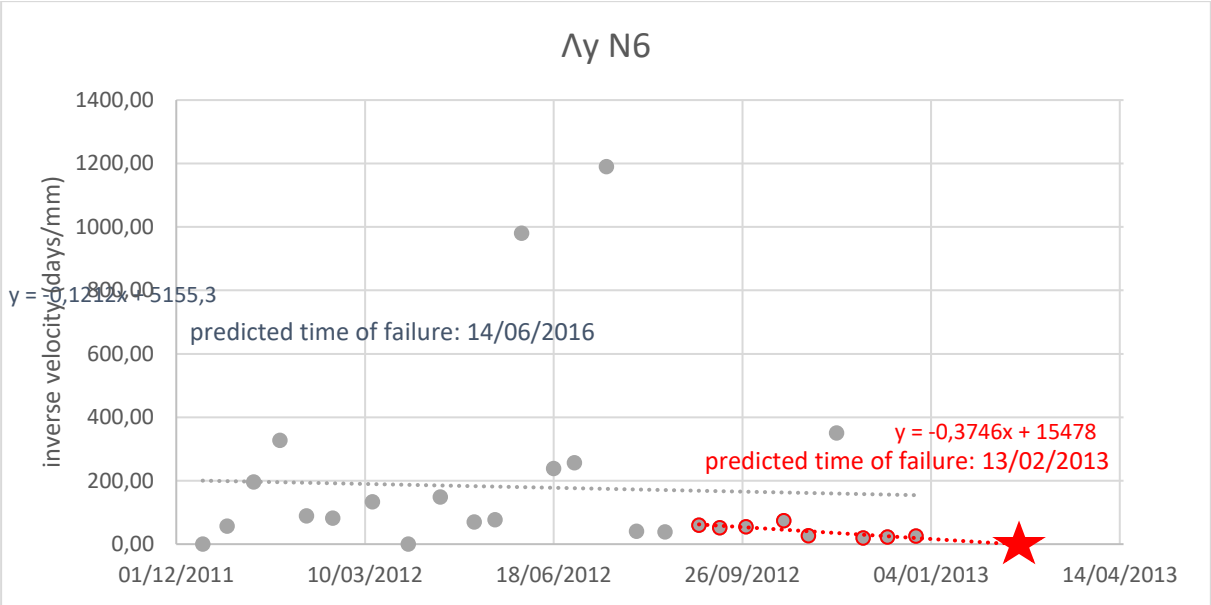

Figure 5.47. Inverse velocity of N6 form December 2011 to December 2012[2]

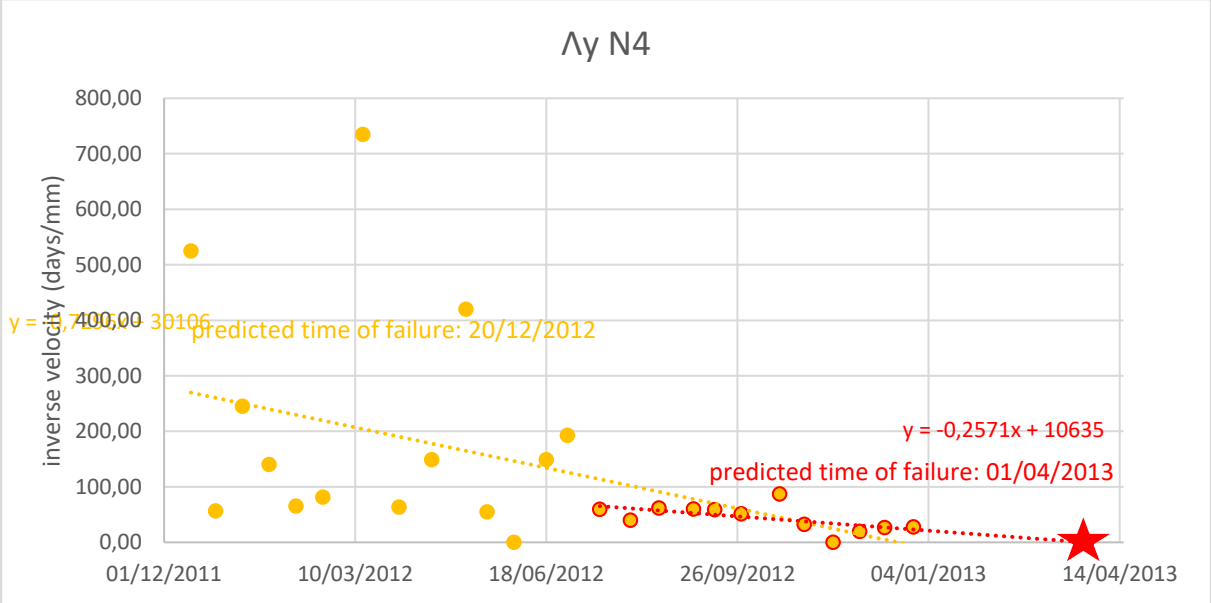

Figure 5.48. Inverse velocity of N4 from December 2011 to December 2012[2]

In the North wall, both for points MO5 and MO3 (Figure 5.45 and Figure 5.46), if the whole time series is considered (December 2011 to December 2012), no landslide is forecasted as the gradients of the trend lines (blue and green) are positive. Nevertheless, if only the points highlighted in red are considered, a predicted time of failure on the 19 January 2013 and 17 February 2013, for MO5 and MO3, respectively.

In the East wall (Figure 5.47 and Figure 5.48), if the whole time series is considered (December 2011 to December 2012), the predicted times of failure of the MSPA would be on the 14 June 2016 and 20 December 2012, for N6 and N4, respectively. In the case of N4, the false alarm would have been detected at the time as it is still in the displacements monitored time series, and the gradient of the trend line is probably more influenced by the high inverse velocity values. However, the points highlighted in

red show a different decreasing trend line, leading to a predicted time of failure on the 13 February 2013 and 1 April 2013, for N6 and N4, respectively.

Generally, the Fukuzono (1985) method can be an advantage to prevent life and material losses in case of a real landslide in the MSPA area. However, as it has been seen with the analysed points above, it is necessary to be cautious using the values of inverse velocity as they need to be constantly updated. In fact, the results observed in Figure 5.45 to Figure 5.48 are all false alarms as the MSPA has not failed until 2017, when stabilization works were performed.

It should also be mentioned that the Fukuzono (1985) method is meant to be used once tertiary stage is reached. Tertiary stage is described by displacements increasing exponentially, different than secondary stage that is described by displacements increasing linearly. In displacements of N4 and N6 (Figure 5.43) there seems to be an exponential increase of displacement. However, after analysing the inverse velocity and comparing the cumulative displacements with their trend line, this exponential increase in most likely due to seasonal variations and do not mean that the point has reached tertiary stage, In displacements of MO5 and MO3 (Figure 5.43) there seems to be an exponential increase of displacement in September 2010, that tended to be linear between June and November 2012, in November 2012 the displacements increased again but since there is few data since that time it is hard to tell if it reached tertiary stage or not. That being said, one of the reasons why the Fukuzono (1985) method “failed” for the MSPA is that perhaps none of the points have reached tertiary stage.

6. Numerical modelling of the *Miradouro de São Pedro de Alcântara*

To simulate the response of the MSPA, the PLAXIS 2D program based on the finite elements method (FEM) is used. In this chapter, the constitutive model used and the model parameters are introduced, as well as the model geometry. Afterwards, a sensitivity study where several causes are individually studies to try to identify the cause that better match the displacements measured in the MSPA, namely: softening of the interface between geotechnical zones and earthquake loading.

6.1. Constitutive models

The stress-strain behaviour of a soil can be simulated by constitutive models with different levels of complexity. Every model has its potentialities and shortcomings, and its choice is an important step towards a meaningful analysis of the problem to be studied.

Commonly, the constitutive models assume that the total incremental deformation associated with a given stress increment can be decomposed into an elastic (recoverable) and a plastic (irrecoverable) components. Elastic deformation can be related with the stress increment, whereas plastic deformations occur when a yield surface is reached.

The Hardening Soil model (HS) is a relatively advanced model, available in the built-in library of constitutive models of PLAXIS, that includes two types of hardening: shear hardening that is used to model irreversible plastic strains due to primary deviatoric loading, and compression hardening that is used to model irreversible plastic strains due to primary compression. The HS model adopts the hyperbolic relationship between the vertical strain, ε_1, and the deviatoric stress, q, in primary triaxial loading (Figure 6.1). The HS model assumes elastic material behaviour during unloading and reloading.

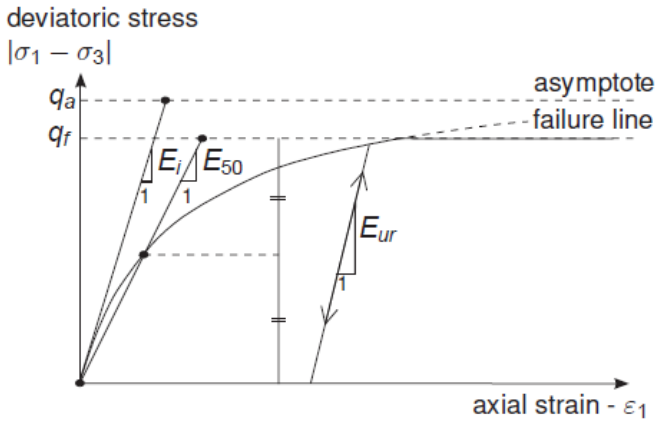

Figure 6.1. Hyperbolic stress-strain relation in primary loading for HS model (Brinkgreve et al., 2019)

The parameters used in the HS model are:

- Failure parameters related to Mohr-Coulomb failure criteria:
  - c': Effective cohesion (kN/m^2) (for drained analysis)
  - φ': Effective angle of internal friction (º) (for drained analysis)

- ψ: Angle of dilatancy (º) (for drained analysis)
- c_u: Undrained resistance (kN/m2) (for undrained analysis)

- Basic parameters for soil stiffness:
  - E_{50}^{ref}: Secant stiffness in standard drained triaxial test at 50% of failure load (kN/m²)
  - E_{oed}^{ref}: Tangent stiffness for primary oedometer loading (kN/m²)
  - E_{ur}^{ref}: Unloading / reloading stiffness (default $E_{ur}^{ref} = 3E_{50}^{ref}$) (kN/m²)
  - m: Power for stress-level dependency of stiffness
- Advanced parameters:
  - ν_{ur}: Poisson's ratio for unloading-reloading (default $\nu_{ur} = 0{,}2$)
  - p^{ref}: Reference stress for stiffness (default $p^{ref} = 100\ kN/m^2$) (kN/m²)
  - K_0^{nc}: K_0-value for normally consolidated soils (default $K_0^{nc} = 1 - \sin\varphi$)
  - R_f: Failure ration q_f/q_a (default $R_f = 0{,}9$)
  - $\sigma_{tension}$: Tensile strength (default $\sigma_{tension} = 0$ stress units) (kN/m²)

The range in which a soil can be considered truly elastic is very small. In fact, the soil's stiffness decays nonlinearly with increasing strain amplitude (Figure 6.2), which is why the Hardening Soil with small strain-stiffness model (HSsmall) is used to model the MSPA behaviour. Because the displacement level measured in the MSPA is small, in this work was adopted the HSsmall model because it more accurately simulates the stiffness of the soil in the small strain range.

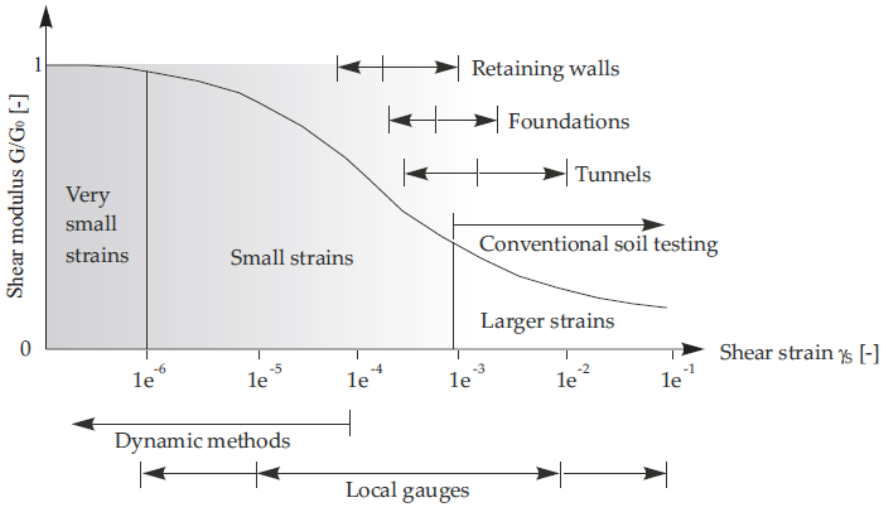

Figure 6.2. Characteristic stiffness-strain behaviour of soil (Brinkgreve et al., 2019)

The HSsmall model is based on the HS model, as it uses the same input parameters and two additional ones to describe the soil behaviour in the small strains range:

- G_0^{ref}: Reference shear modulus at very small strains ($\varepsilon < 10^{-6}$)
- $\gamma_{0.7}$: Threshold shear strain at which the secant shear modulus $0.722G_0$

Considering the default reference stress for stiffness, $p^{ref} = 100\ kN/m^2$, the parameters for soil stiffness: the secant stiffness in standard drained triaxial test, E_{50}^{ref}, the tangent stiffness for primary

oedometer loading, E_{oed}^{ref} and the unloading / reloading stiffness, E_{ur}^{ref}, are determined by equations (6.1), (6.2) and (6.3), respectively.

$$E_{50}^{ref} = E_{50} / \left(\frac{c' \cos\varphi - \sigma_3' \sin\varphi}{c' \cos\varphi - p^{ref} \sin\varphi} \right)^m \tag{6.1}$$

Where the power for stress-level dependency of stiffness, m, is considered 0,5.

$$E_{oed}^{ref} = E_{50}^{ref} \tag{6.2}$$

$$E_{ur}^{ref} = 3E_{50}^{ref} \tag{6.3}$$

The parameters that describe the soil behaviour in the small strains range: the reference shear modulus at very small strains, G_0^{ref}, and the threshold shear strain, $\gamma_{0.7}$, are determined by equations (6.4) and (6.5), respectively.

$$G_0^{ref} = G_0 / \left(\frac{c' \cos\varphi - \sigma_3' \sin\varphi}{c' \cos\varphi - p^{ref} \sin\varphi} \right)^m \tag{6.4}$$

$$\gamma_{0.7} \approx \frac{1}{9G_0} [2c'(1 + \cos(2\varphi')) - \sigma_1'(1 + K_0)\sin(2\varphi')] \tag{6.5}$$

6.2. Model Geometry

The aim of the finite elements (FE) model is to simulate the response of the MSPA that shows an increasing pattern of displacement in the transversal direction (§5). For that reason, the FE model simulates the MSPA in the transversal direction, in a cross-section that has exhibited larger displacements and intercepts two inclinometers. The chosen cross section is represented in Figure 6.3 as it is the cross section with more field data: the V_S profile and the boreholes S1 and S3 (Table 6.1).

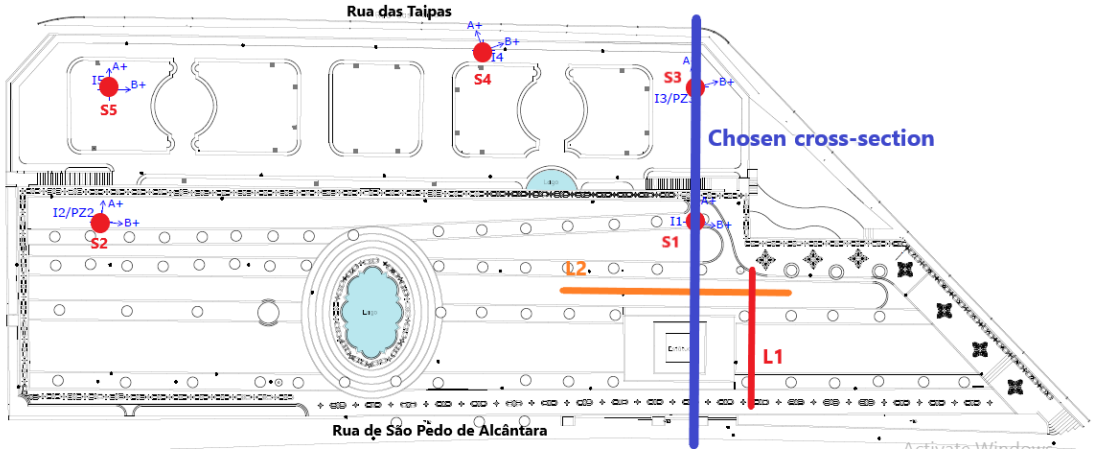

Figure 6.3. Position of the chosen cross-section

Table 6.1. Field data from the V_S profile and the boreholes S1 and S3

	V_S profile	S1	S3
GZ1 thickness (m)	7	17	14
GZ2 thickness (m)	(-)	9	9
GZ3 thickness (m)	(not reached)	(-)	(-)

The geometry used for the model is presented in Figure 6.4.

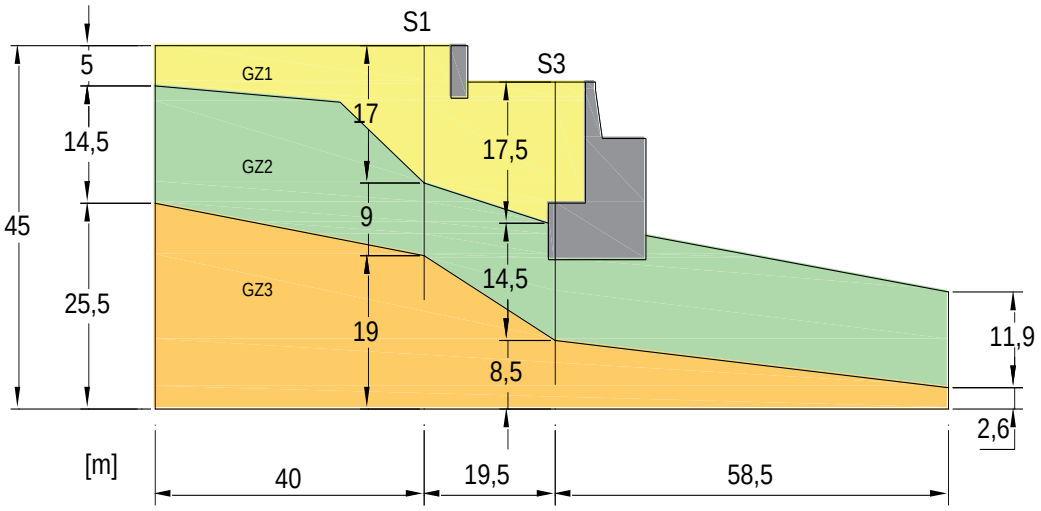

Figure 6.4. Geometry of the FE model

6.3. Model parameters

To determine the model parameters described in §6.1, the soil parameters determined in §4.3.3.2 and average thicknesses of each GZ are used (Table 6.2).

Table 6.2. Soil parameters of the MSPA and characteristics of the chosen profile

	GZ1	GZ2	GZ3
Soil characteristics			
γ (kN/m^3)	16	20	25
PI (%)	10	15	20
ϕ' (º)	30	35	40
c' (kN/m^2)	0	0	0
c_u (kN/m^2)	80	200	360
G_0 (kN/m^2)	200 000	586 000	991 000
E_0 (kN/m^2)	480 000	1 410 000	2 377 000
Profile characteristics			
Thickness (m)	7	23	15
K_0	0,50	0,43	0,29
σ_1' (kN/m2)	56	342	604
σ_3' (kN/m2)	28	145	177

There is no direct relationship between E_0 and E_{50}. Nevertheless, it was noticed that the rato E_0/E_{50} varies from 3,5 to 18 depending on the preconsolidation ratio (Obrzud & Truty, 2018).

Considering the parameters presented in Table 6.2, the equations (6.6) to (6.9), from Ishibashi & Zhang (1993) to describe the stiffness-strain and the stress-strain behaviour of the soil.

$$\frac{G}{G_0} = K(\gamma, PI)(p')^{m(\gamma,PI)-m_0} \tag{6.6}$$

Where,

$$K(\gamma, PI) = 0{,}5\left[1 + \tanh\left(\ln\left(\frac{0{,}000102 + n(PI)}{\gamma}\right)^{0{,}492}\right)\right] \tag{6.7}$$

$$m(\gamma, PI) - m_0 = 0{,}272\left[1 - \tanh\left(\ln\left(\frac{0{,}000556}{\gamma}\right)^{0{,}4}\right)\right] e^{-0{,}0145PI^{1{,}3}} \tag{6.8}$$

$$n(PI) = \begin{cases} 0 \; if \; PI = 0 \\ 3{,}37 \times 10^{-6} \times PI^{1{,}404} \; if \; 0 < PI \leq 15 \\ 7{,}0 \times 10^{-7} \times PI^{1{,}976} \; if \; 15 < PI \leq 70 \\ 2{,}7 \times 10^{-5} \times PI^{1{,}115} \; if \; PI > 70 \end{cases} \tag{6.9}$$

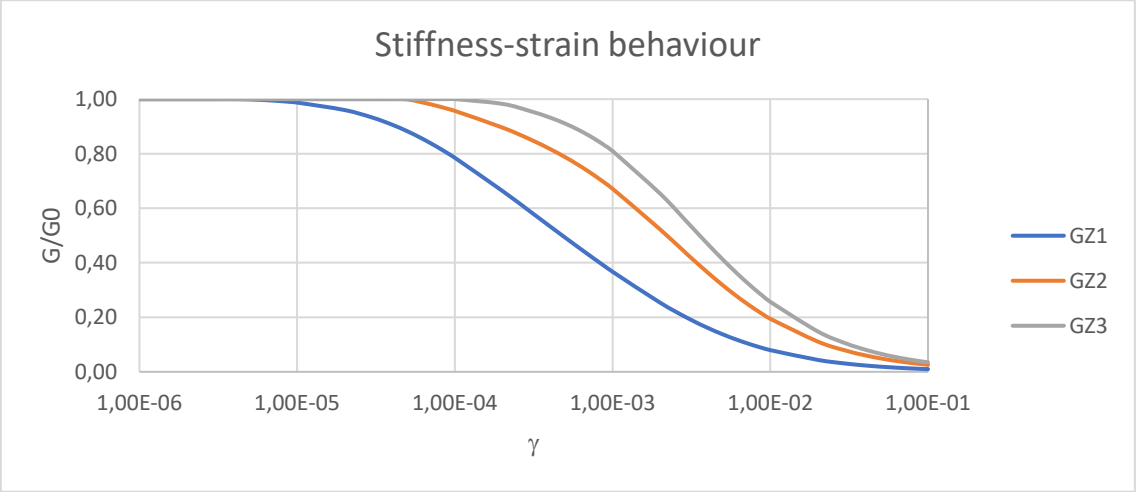

Figure 6.5. Stiffness-strain behaviour of the soil

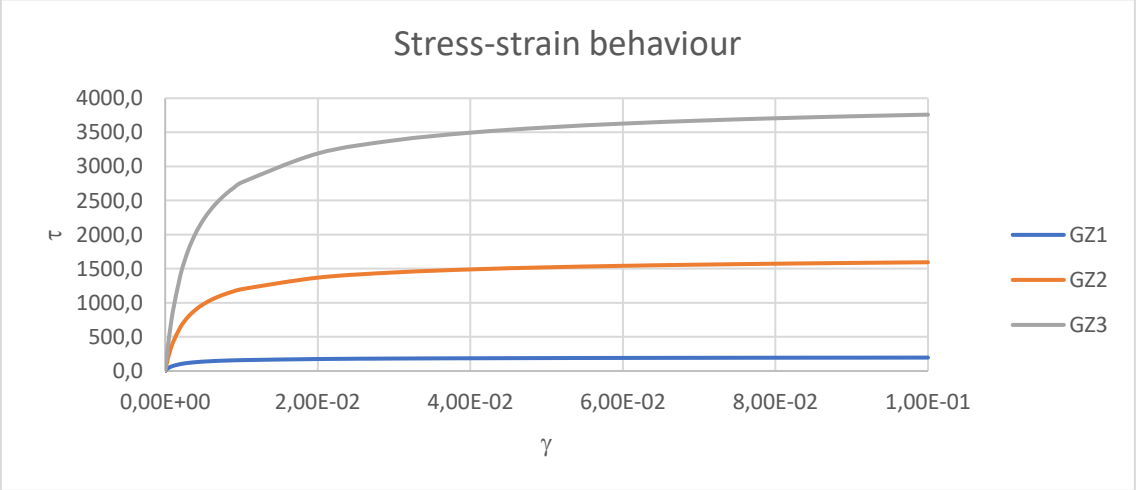

Figure 6.6. Stress-strain behaviour of the soil

In the three GZ, the ratio $E_0/E_{50} \approx 4$, value used to determine the soil parameters for the model that are presented in Table 6.3, and the triaxial tests simulation are presented in Figure 6.7

Table 6.3. Model parameters

	GZ1	GZ2	GZ3
Soil parameters			
γ_{unsat} (kN/m^3)	16	20	25
γ_{sat} (kN/m^3)	16	20	25
ϕ' (º)[1]	30	35	40
c' (kN/m^2)[1]	0	0	0
c_u (kN/m^2)[2]	80	200	360
Parameters for soil stiffness			
E_{50}^{ref} (kN/m^2)	227 000	307 000	486 000
E_{oed}^{ref} (kN/m^2)	227 000	307 000	486 000
E_{ur}^{ref} (kN/m^2)	680 000	921 000	1 458 000
Parameters to describe soil behaviour in the small strains range			
G_0^{ref} (kN/m^2)	3 780 000	511 000	809 000
$\gamma_{0.7}$ (-)	$4{,}0 \times 10^{-5}$	$8{,}3 \times 10^{-5}$	$8{,}1 \times 10^{-5}$

[1] parameters used for drained analysis
[2] parameters used for undrained analysis

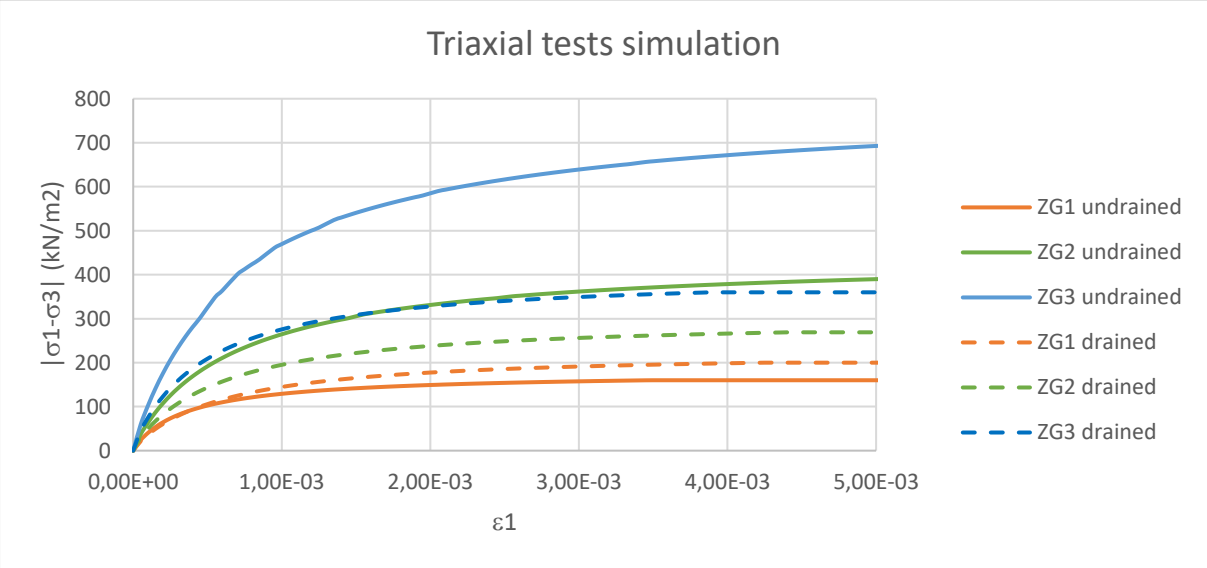

Figure 6.7. Triaxial tests simulation

For the masonry retaining walls, nonspecific test was performed. To model the retaining walls of the MSPA a linear elastic is used with typical parameters for the material, presented in Table 6.4.

Table 6.4. Parameters of the retaining walls

γ (kN/m^3)	22
E (kN/m^2)	30×10^6
ν (-)	0,3

6.4. Simulation sequence

To model the behaviour of the MSPA, first is calculated the initial stresses of the model caused by the application of gravity, using the calculation type “Gravity loading”.

After, hypotheses to explain the displacements measured in the MSPA are tested. As discussed in §5.2, two possible slip surfaces could explain the displacements observed in the transversal direction of the MSPA, one between GZ2 and GZ3 and another one between GZ2 and the lower retaining wall. These two potential slip surfaces are modelled, simulating two interfaces: interface 1 and interface 2, that correspond to the potential slip surfaces between GZ2 and GZ3, and between GZ2 and the lower retaining wall, respectively (Figure 6.8). The following cases are simulated:

A. Movement along interface 1

B. Movement along interface 2

C. Movement along both interfaces

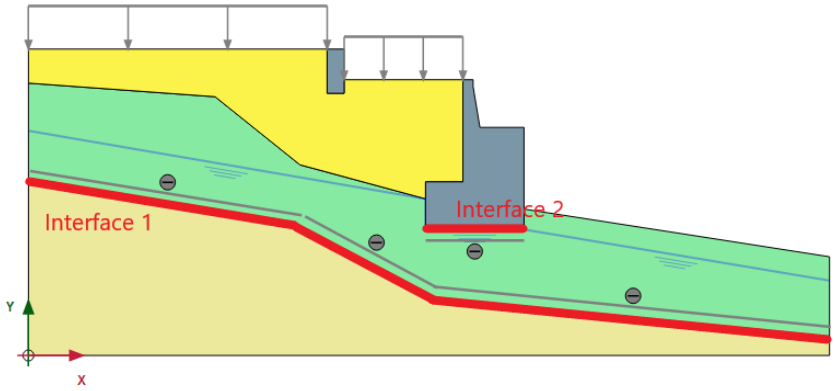

Figure 6.8. Position of the interfaces

To model the softening interface effect, the strength reduction factor, R_{inter}, is reduced from 1 to 0,7 and 0,5 assess its impact on the displacements in the MSPA.

Additionally, a pseudo-static analysis is preformed to evaluate the stability of the MSPA under seismic action.

The sequences stated are tested in PLAXIS 2D trough phases of analysis (Table 6.5).

Table 6.5. Phases of analysis in PLAXIS 2D

Phase	Name	Start from phase	Calculation type	Description
1	Gravity activation	-	Gravity loading (to be used for non-horizontal layers)	Calculation of initial stresses, only considering the force of gravity. The displacements are then reset for the next phases.
2	Interface 1	1	Plastic	Calculation of displacements with 1kN/m loading[1] at the top of the MSPA, and the effects of interface 1 (Figure 6.8).
3	Interface 2	1	Plastic	Calculation of displacements with 1kN/m loading[1] at the top of the MSPA, and the effects of interface 2 (Figure 6.8).
4	Interface 1+2	1	Plastic	Calculation of displacements with 1kN/m loading[1] at the top of the MSPA, and the effects of interface 1 and 2 (Figure 6.8).
5	Pseudo-static analysis	1	Plastic	Calculation of displacements with a horizontal acceleration of 0,004g to assess the impact of the M4.2 earthquake (§5.4.2) and 0.50g to determine the failure surface induced by a M8 earthquake.

[1] this loading simulates a frequent service load over the MSPA area.

Due to the uncertainty on the type of load, saturation level and grain size distribution of the soils in the MSPA area, the simulations are done assuming drained and undrained responses, to determine which behaviour better fits the response of the MSPA. To model the undrained behaviour of soils, PLAXIS 2D allows two types of analysis:

- Undrained A, where stiffness and strength are defined in terms of effective properties. It is usually used when consolidation and long term analysis are a requirement (Karstunen, 2011).
- Undrained B, where stiffness is defined in terms of effective properties and strength is defined as undrained shear strength. It is useful for stability problems in undrained conditions, however it does not represent the true behaviour of soil before rupture (Karstunen, 2011).

The simulations performed in this work are far from failure, thus for simplicity it was chosen to adopt “Undrained B” option.

6.5. Numerical simulation

6.5.1. Case A – Movement along interface 1

The transversal calculated displacements for I1 and I3 are presented in Figure 6.9 and Figure 6.10, respectively.

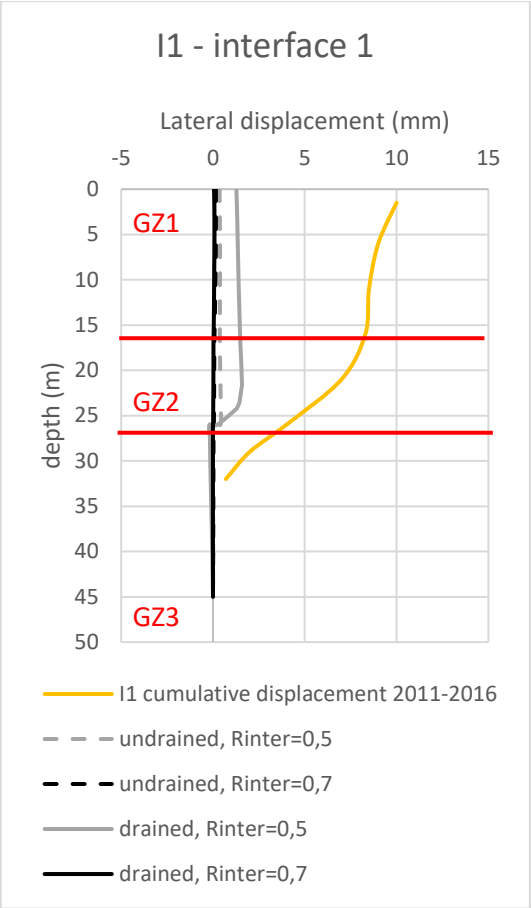

Figure 6.9. Case A - calculated transversal displacements of I1

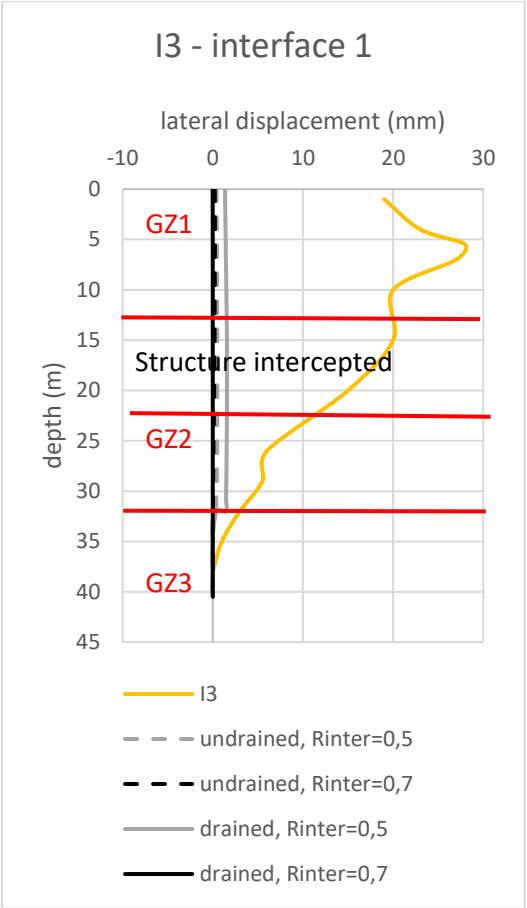

Figure 6.10. Case A - calculated transversal displacements of I3

Overall, the calculated displacements (grey and black lines in Figure 6.9 and Figure 6.10) do not reach the amplitude of the displacements measured on site (yellow line in Figure 6.9 and Figure 6.10), the maximum calculated displacement is ~1,6 mm whereas the maximum measured displacement by the inclinometers is ~30 mm, and ~14 mm in the topographical monitoring (§5.1). Nevertheless, the trend of the displacements is analysed.

Starting with the cases where $R_{inter} = 0{,}5$ (grey lines in Figure 6.9 and Figure 6.10), both I1 and I3, and in the undrained and drained cases, it is noticeable a sharp increase of displacements at the interface GZ2/GZ3, which is not is observed in the measured displacements.

For the cases where $R_{inter} = 0{,}7$ (black lines in Figure 6.9 and Figure 6.10), both I1 and I3, and the undrained and drained cases describe a gradual decrease of displacement with depth which is closer to what is observed in the inclinometers.

Globally, the transversal displacements calculated with $R_{inter} = 0{,}5$ are not representative of the displacements measured by the inclinometers and the displacements calculated with $R_{inter} = 0{,}7$ the undrained case seems to present a better fit to the displacements measured on site. Nevertheless, the calculated displacements are close to zero, which could indicate that there are more actions playing in the MSPA that increase the displacements.

The overall behaviour of the model is now analysed comparing the total displacements, total strains and plastic points distributions. total displacements to understand the displacement mechanism to understand how the slope is moving. The total strains to understand if the slope is behaving in a elastic or plastic range. The plastic points show the stress points that are in a plastic state, the plastic points that occurred during these simulations are:

- Hardening points (green pyramid) that represent points on the shear hardening envelope
- Tension cut-off points (white cube) where the tension cut-off criterion was applied, meaning that the normal tension is not allowed to exceed a pre-set tensile tension (default: 0 kN/m^2).
- Failure points (red cube) that indicate that the stresses lie on the surface of the failure envelope
- Cap points (blue upside-down pyramid) that represent a state of normal consolidation where the pre-consolidation stress is equivalent to the actual stress state
- Cap + hardening points (brown diamond) that represent points that are on the shear hardening and cap envelope

Starting with the undrained behaviour, the total displacements (Figure 6.11 and Figure 6.12), total cartesian strains (Figure 6.13 and Figure 6.14) and plastic points (Figure 6.15 and Figure 6.16) are presented in smaller figures to show an overall view on the displacement mechanism and plastic points.

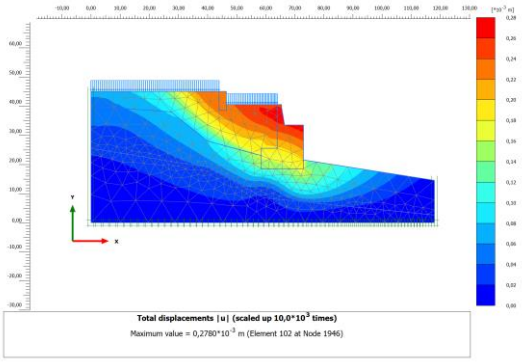

Figure 6.11. Case A - calculated total displacements for undrained behaviour and $R_{inter} = 0{,}5$

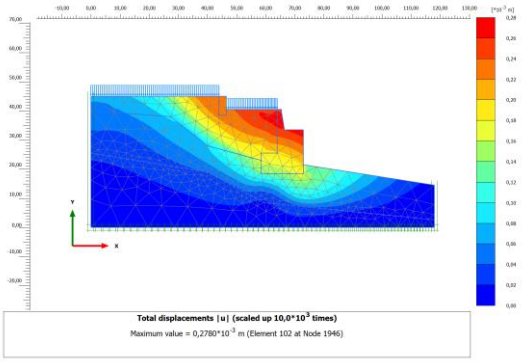

Figure 6.12. Case A - calculated total displacements for undrained behaviour and $R_{inter} = 0{,}7$

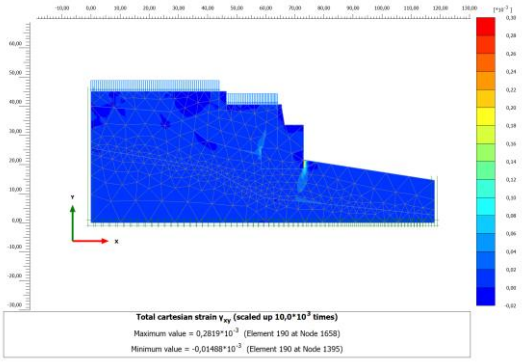

Figure 6.13. Case A - calculated total cartesian strains for undrained behaviour and $R_{inter} = 0{,}5$

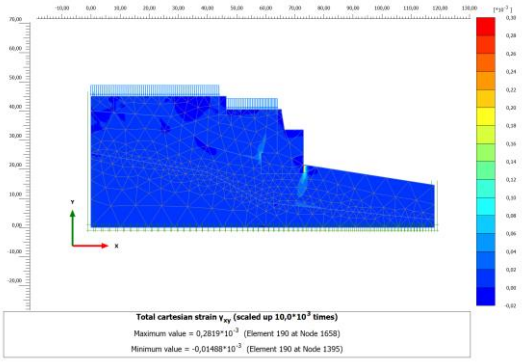

Figure 6.14. Case A - calculated total cartesian strains for undrained behaviour and $R_{inter} = 0{,}7$

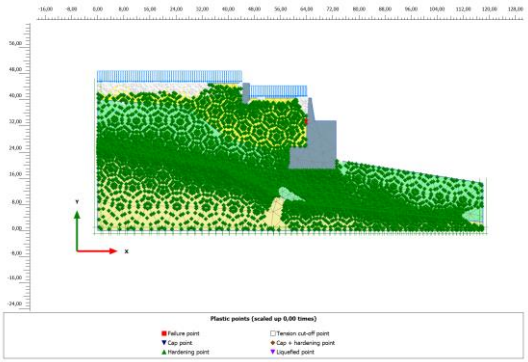

Figure 6.15. Case A - plastic points for undrained behaviour and $R_{inter} = 0{,}5$

Figure 6.16. Case A - plastic points for undrained behaviour and $R_{inter} = 0{,}7$

From the total displacements (Figure 6.11 and Figure 6.12) it can be seen that the displacements are mostly concentrated at the top of the lower platform and tend to reduce with depth, the larger displacement being ~0,3 mm both in the cases where $R_{inter} = 0{,}5$ and $0{,}7$. It can also be seen that there is a compound slip surface is forming: a plane surface right under the MSPA, and after the lower retaining wall it tends to be more circular.

For the total strains (Figure 6.13 and Figure 6.14) the maximum value is $\sim 0{,}3 \times 10^{-3}$ in both cases of R_{inter} indicating that the MSPA is in the small strain range, with larger stains at the bottom of the lower retaining wall.

The plastic points (Figure 6.15 and Figure 6.16) present similar distributions in both cases of R_{inter} with hardening points distributed almost throughout the extent of the model and particularly concentrated at the interface GZ2/GZ3 as it would be expected since it is the area where the strength is reduced, therefor the displacements increase, result of increase straining. Failure points are also present next to the lower retaining wall at the level of *Rua das Taipas*.

Considering now the drained behaviour, the total displacements (Figure 6.17 and Figure 6.18), total cartesian strains (Figure 6.19 and Figure 6.20) and plastic points (Figure 6.21 and Figure 6.22) are presented in smaller figures to show an overall view on the displacement mechanism and plastic points.

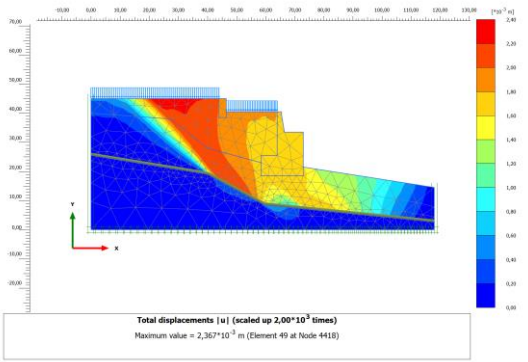

Figure 6.17. Case A - calculated total displacements for drained behaviour and $R_{inter} = 0{,}5$

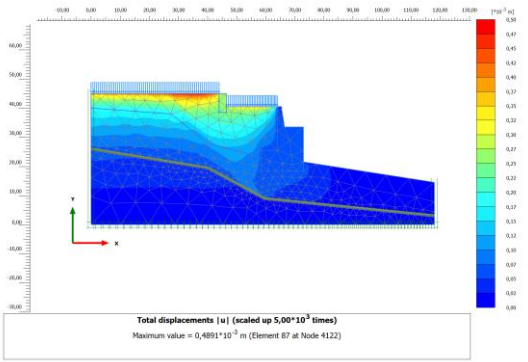

Figure 6.18. Case A - calculated total displacements for drained behaviour and $R_{inter} = 0{,}7$

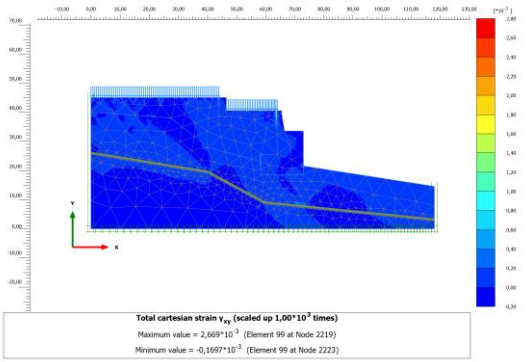

Figure 6.19. Case A - calculated total cartesian strains for drained behaviour and $R_{inter} = 0{,}5$

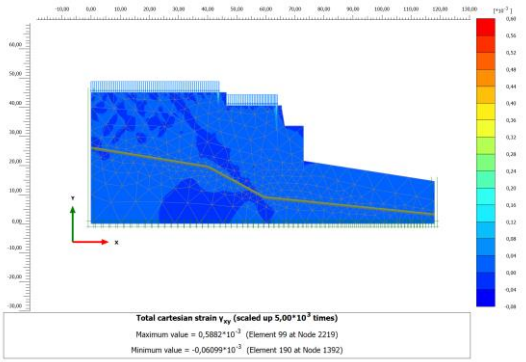

Figure 6.20. Case A - calculated total cartesian strains for drained behaviour and $R_{inter} = 0{,}7$

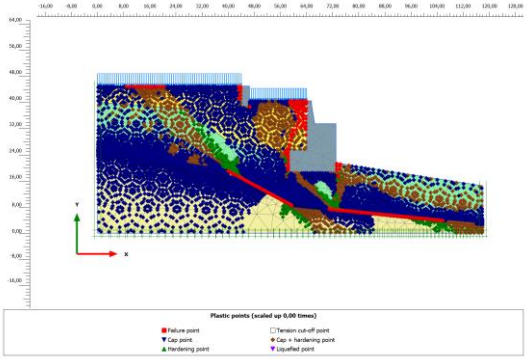

Figure 6.21. Case A - plastic points for drained behaviour and $R_{inter} = 0{,}5$

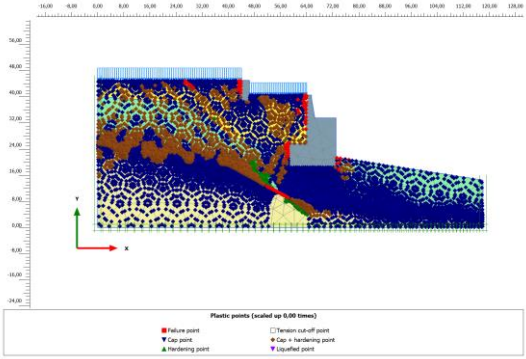

Figure 6.22. Case A - plastic points for drained behaviour and $R_{inter} = 0{,}7$

Contrary to the case where undrained behaviour is considered, in the cases of drained behaviour, the total displacements and the total stains show different results. In the case where $R_{inter} = 0{,}5$, there is a clear planar slip surface where the displacements are larger right below the MSPA (Figure 6.17) and the maximum strain (Figure 6.19) is $\sim 2{,}7 \times 10^{-3}$ indicating the start of large strains, the larger strains being concentrated at the top of the lower retaining wall. In the case where $R_{inter} = 0{,}7$, the displacements are larger in the upper platform (Figure 6.18), however, no particular slip surface is observed, and the maximum strain (Figure 6.19) is $\sim 0{,}6 \times 10^{-3}$ indicating the model is in the small strains range, the larger strains being concentrated at the top of the upper and lower retaining walls.

In the distribution of plastic points (Figure 6.21 and Figure 6.22) cap and cap + hardening points are concentrated at the interface GZ2/GZ3 as it would be expected, and failure points are present next to the two retaining wall and at the interface GZ2/GZ3, more numerous in the case where $R_{inter} = 0{,}5$.

6.5.2. Case B – Movement along interface 2

The transversal calculated displacements for I1 and I3 are presented in Figure 6.23 and Figure 6.24, respectively.

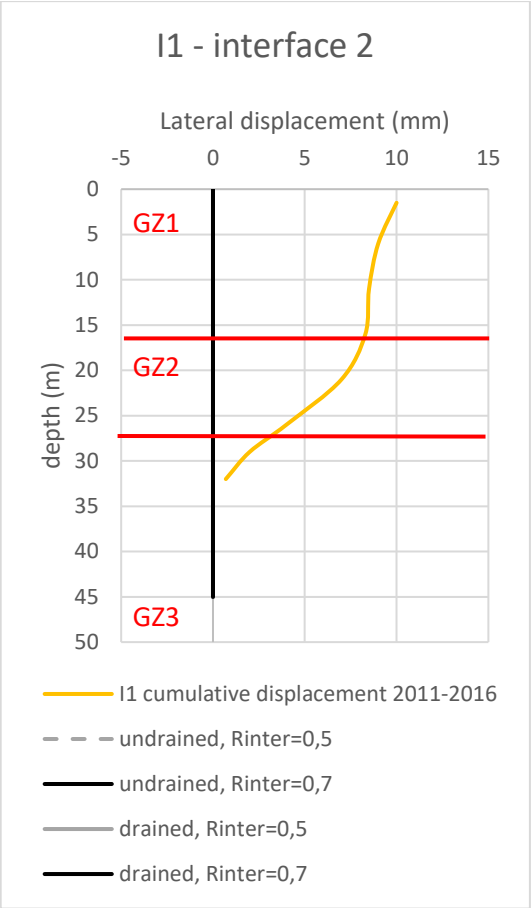

Figure 6.23. Case B - calculated transversal displacements of I1

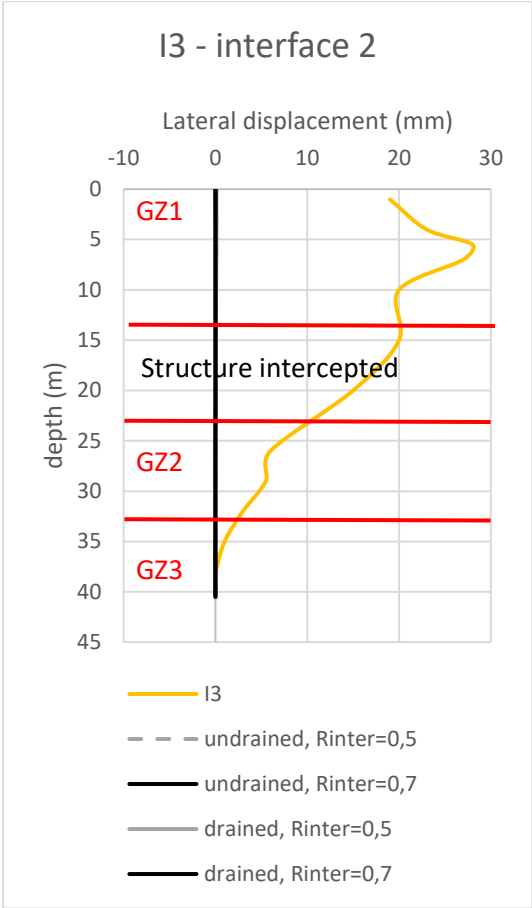

Figure 6.24. Case B - calculated transversal displacements of I3

As it was seen in case A (§6.5.1), the calculated displacements (grey and black lines in Figure 6.23 and Figure 6.24) do not reach the amplitude of the displacements measured by the inclinometers (yellow line in Figure 6.23 and Figure 6.24), the maximum calculated displacement is ~0,05 mm whereas the maximum measured displacement by the inclinometers is ~30 mm, and ~14 mm in the topographical monitoring (§5.1). However, different behaviours are observed in the calculated displacements for case B: in all cases displacement seems to decrease with depth and no sharp or increased displacement is observed meaning that the hypothesis of a possible slip surface between the structure of the lower wall and GZ2 does not represent what is observed on site.

The overall behaviour of the model is now analysed comparing the total displacements, total strains and plastic points distributions. total displacements to understand the displacement mechanism to understand how the slope is moving. The total strains to understand if the slope is behaving in an elastic or plastic range.

Starting with the undrained behaviour, the total displacements (Figure 6.25 and Figure 6.26), total cartesian strains (Figure 6.27 and Figure 6.28) and plastic points (Figure 6.29 and Figure 6.30) are presented in smaller figures to show an overall view on the displacement mechanism and plastic points.

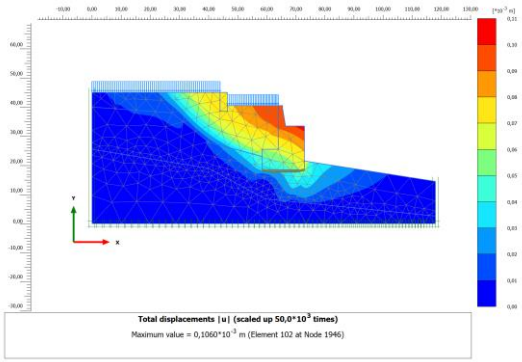

Figure 6.25. Case B - calculated total displacements for undrained behaviour and $R_{inter} = 0{,}5$

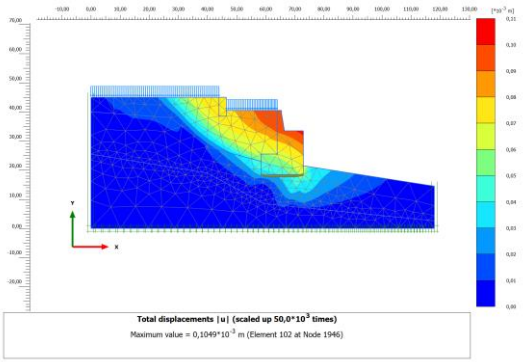

Figure 6.26. Case B - calculated total displacements for undrained behaviour and $R_{inter} = 0{,}7$

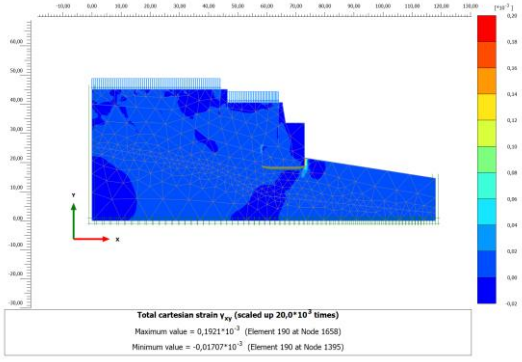

Figure 6.27. Case B - calculated total cartesian strains for undrained behaviour and $R_{inter} = 0{,}5$

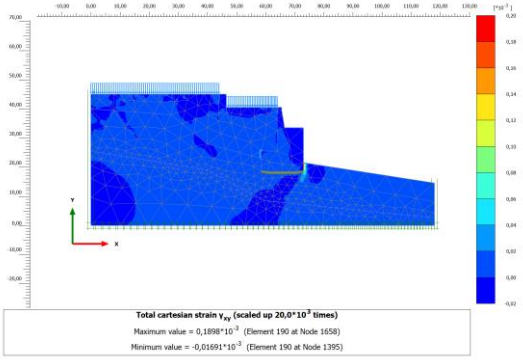

Figure 6.28. Case B - calculated total cartesian strains for undrained behaviour and $R_{inter} = 0{,}7$

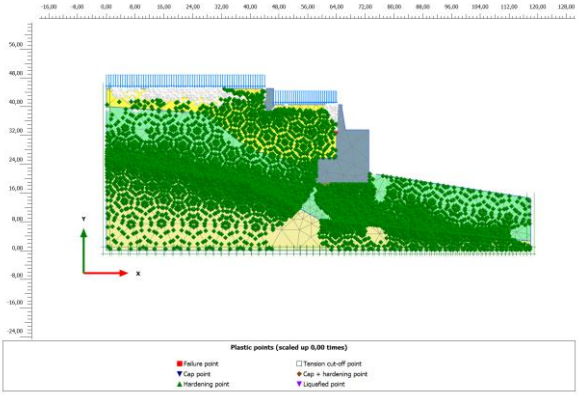

Figure 6.29. Case B - plastic points for undrained behaviour and $R_{inter} = 0{,}5$

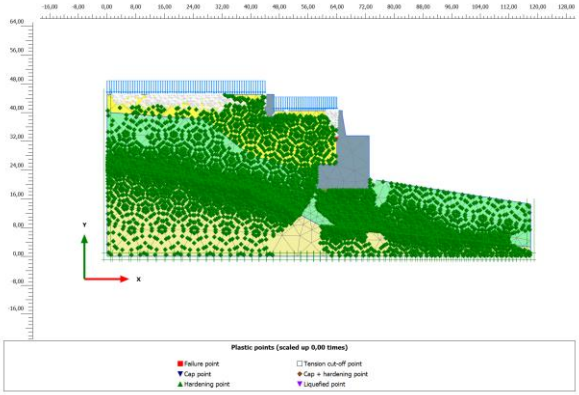

Figure 6.30. Case B - plastic points for undrained behaviour and $R_{inter} = 0{,}7$

The total displacements (Figure 6.25 and Figure 6.26) present a similar distribution, with larger displacements in the lower platform, and the displacement are more concentrated GZ1 with a compound slip surface: a plane surface right under the MSPA, and after the lower retaining wall it tends to be more circular. The total strains (Figure 6.27 and Figure 6.28) also present a similar distribution with the maximum strain $\sim 0{,}2 \times 10^{-3}$ indicating that the model is in the small strains range, and the larger strains are concentrated at the bottom of the lower retaining wall.

The failure points occur in a very small number (Figure 6.29 and Figure 6.30), similarly to in case A (§6.5.1).

Considering now the drained behaviour, the total displacements (Figure 6.31 and Figure 6.32), total cartesian strains (Figure 6.33 and Figure 6.34) and plastic points (Figure 6.35 and Figure 6.36) are presented in smaller figures to show an overall view on the displacement mechanism and plastic points.

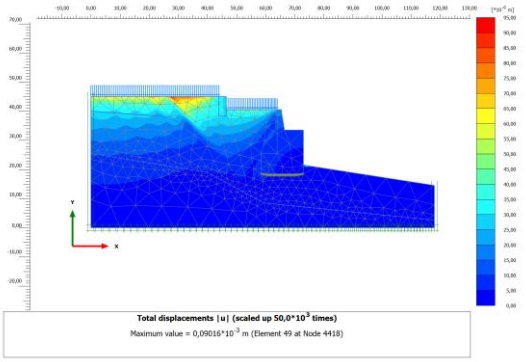

Figure 6.31. Case B - calculated total displacements for drained behaviour and $R_{inter} = 0{,}5$

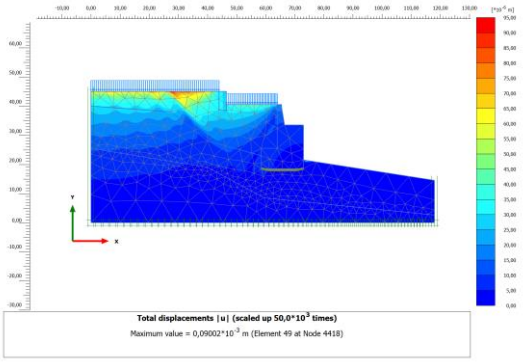

Figure 6.32. Case B - calculated total displacements for drained behaviour and $R_{inter} = 0{,}7$

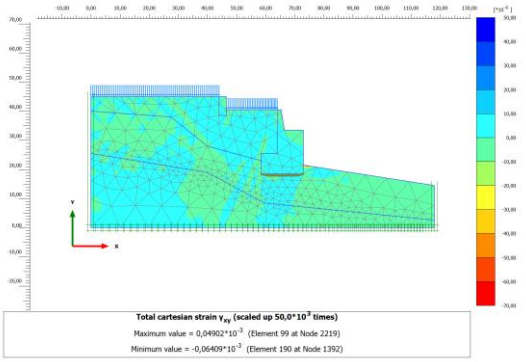

Figure 6.33. Case B - calculated total cartesian strains for drained behaviour and $R_{inter} = 0{,}5$

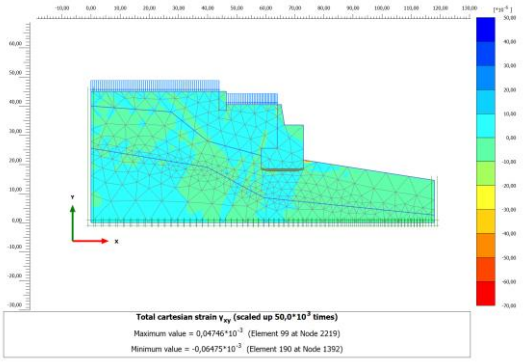

Figure 6.34. Case B - calculated total cartesian strains for drained behaviour and $R_{inter} = 0{,}7$

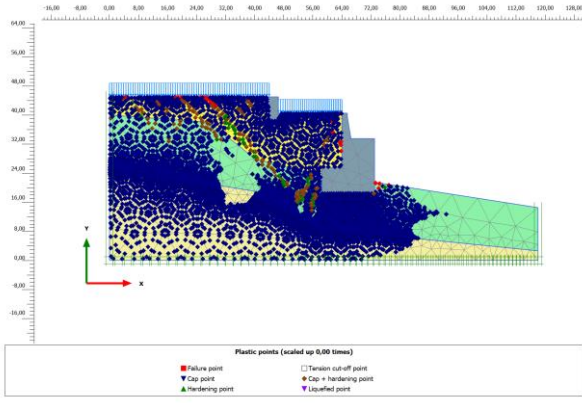

Figure 6.35. Case B - plastic points for drained behaviour and $R_{inter} = 0{,}5$

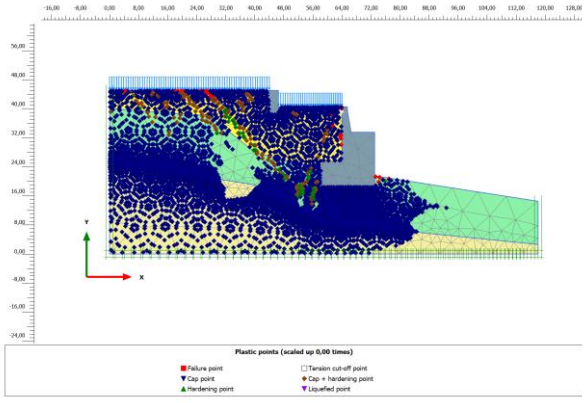

Figure 6.36. Case B - plastic points for drained behaviour and $R_{inter} = 0{,}7$

The total displacement (Figure 6.31 and Figure 6.32) present similar distributions with larger displacements in the upper platform and a planar slip surface starting in the upper platform and almost reaching the lower retaining wall. The total strains (Figure 6.27 and Figure 6.28) also present a similar distribution with the maximum strain $\sim 0{,}5 \times 10^{-2}$ indicating that the model is in the small strains range, and the larger strains are concentrated at the bottom of the lower retaining wall.

The plastic points distribution (Figure 6.35 and Figure 6.36) present a similar distribution in both cases with cap points specially concentrated in the upper and lower platform and in the interface GZ2/GZ3. Failure point can also be seen in the area where the planar slip surface is forming as well as next to the lower retaining wall.

6.5.3. Case C – Movement along interface 1 and 2

The transversal calculated displacements for I1 and I3 are presented in Figure 6.37 and Figure 6.38, respectively.

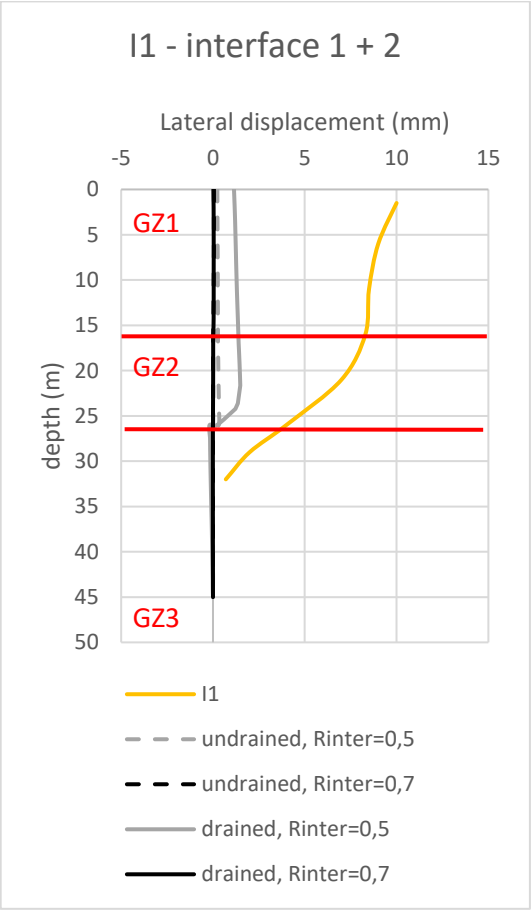

Figure 6.37. Case C - calculated transversal displacements of I1

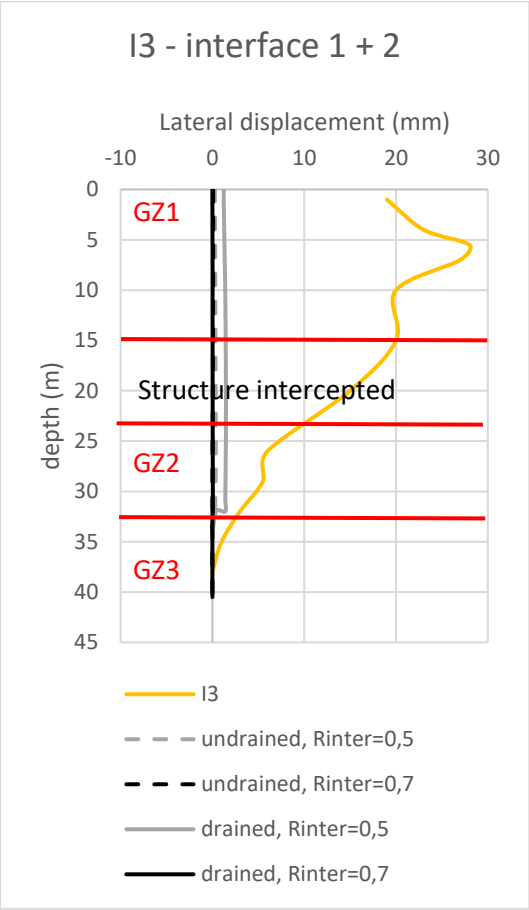

Figure 6.38. Case C - calculated transversal displacements of I3

As it was seen in case A (§6.5.1), the calculated displacements (grey and black lines in Figure 6.23 and Figure 6.24) do not reach the amplitude of the displacements measured by the inclinometers (yellow line in Figure 6.23 and Figure 6.24), the maximum calculated displacement is ~1,5 mm whereas the maximum measured displacement by the inclinometers is ~30 mm, and ~14 mm in the topographical monitoring (§5.1). The trend of the calculated displacements for case C is also the trend of calculated displacements for case A (§6.5.1). The cases where $R_{inter} = 0{,}5$ (grey lines in Figure 6.37 and Figure 6.38), both in the undrained and drained cases, a sharp increase of displacements occur at the interface GZ2/GZ3, which is not is observed in the measured displacements.

For the cases where $R_{inter} = 0{,}7$ (black lines in Figure 6.37 and Figure 6.38), both the undrained and drained cases describe a gradual decrease of displacement with depth which is closer to what is observed in the inclinometers.

Globally, case C presents similar displacements as case A (§6.5.1). However, case C presents smaller displacements that case A.

Starting with the undrained behaviour, the total displacements (Figure 6.39 and Figure 6.40), total cartesian strains (Figure 6.41 and Figure 6.42) and plastic points (Figure 6.43 and Figure 6.44) are presented in smaller figures to show an overall view on the displacement mechanism and plastic points.

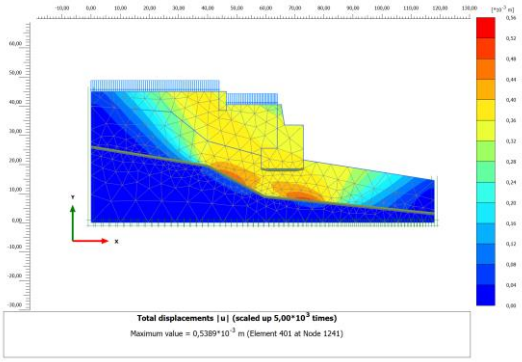

Figure 6.39. Case C - calculated total displacements for $R_{inter} = 0{,}5$

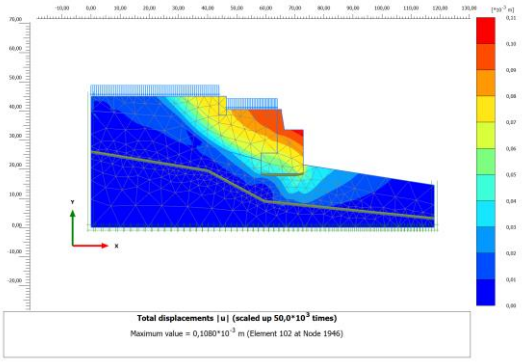

Figure 6.40. Case C - calculated total displacements for $R_{inter} = 0{,}7$

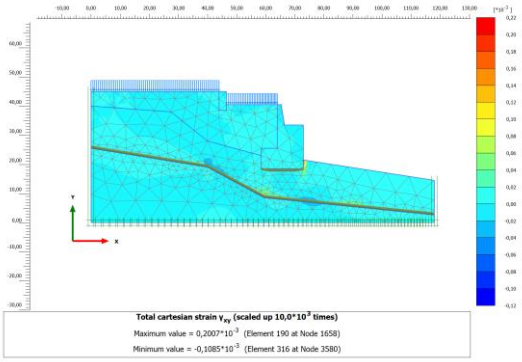

Figure 6.41. Case C - calculated total cartesian strains for undrained behaviour and $R_{inter} = 0{,}5$

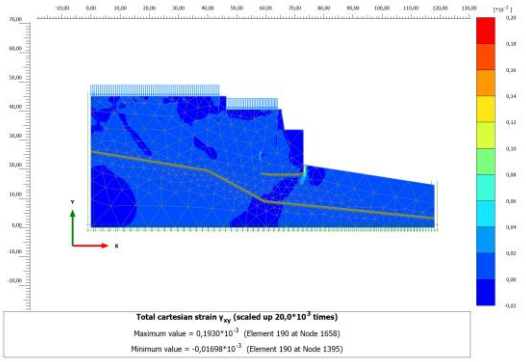

Figure 6.42. Case C - calculated total cartesian strains for undrained behaviour and $R_{inter} = 0{,}7$

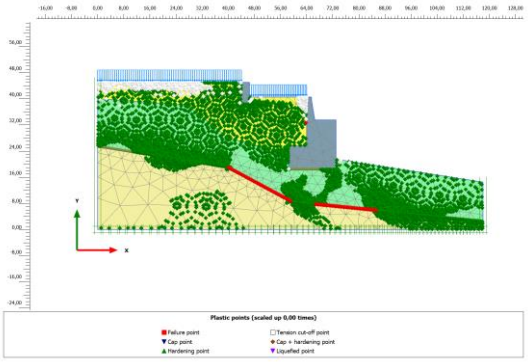

Figure 6.43. Case C - plastic points for undrained behaviour and $R_{inter} = 0{,}5$

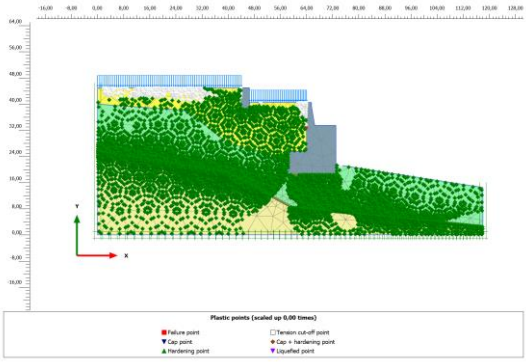

Figure 6.44. Case C - plastic points for undrained behaviour and $R_{inter} = 0{,}7$

The total displacement show two different behaviours, in the case where $R_{inter} = 0{,}5$ (Figure 6.39), there is a circular slip surface that stops at the interface GZ2/GZ3. For the case where $R_{inter} = 0{,}7$ (Figure 6.40), a compound slip surface is observed as for case A and B (§6.5.1 and §6.5.2): planar below the MSPA and circular after the lower retaining wall.

The total strains (Figure 6.41 and Figure 6.42) both present a maximum strain $\sim 0{,}2 \times 10^{-3}$ and the larger strains are concentrated below the lower retaining wall. However, in the case where $R_{inter} = 0{,}5$, larger strains are also concentrated at the interface GZ2/GZ3.

For the failure points, in the case where $R_{inter} = 0{,}5$ (Figure 6.43), they are distributed along the interface ZG2/ZG3. In the case where $R_{inter} = 0{,}7$ (Figure 6.44), few failure points are in back of the lower retaining wall.

Considering now the drained behaviour, the total displacements (Figure 6.45 and Figure 6.46), total cartesian strains (Figure 6.47 and Figure 6.48) and plastic points (Figure 6.49 and Figure 6.50) are presented in smaller figures to show an overall view on the displacement mechanism and plastic points.

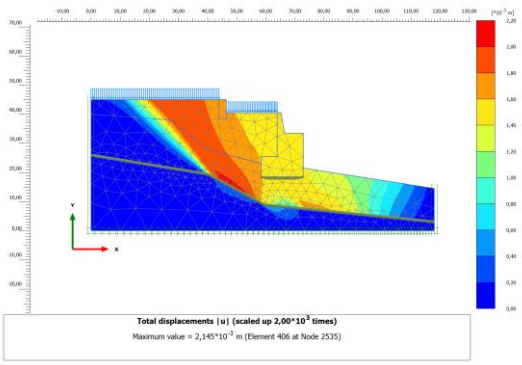

Figure 6.45. Case C - calculated total displacements for drained behaviour and $R_{inter} = 0{,}5$

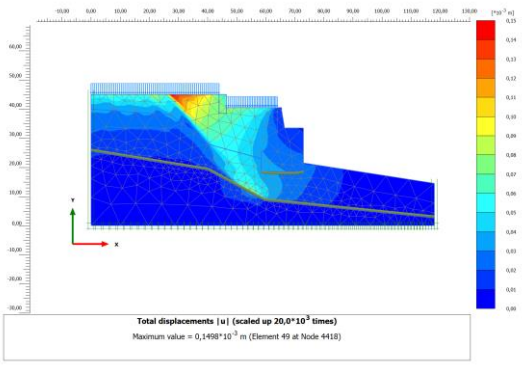

Figure 6.46. Case C - calculated total displacements for drained behaviour and $R_{inter} = 0{,}7$

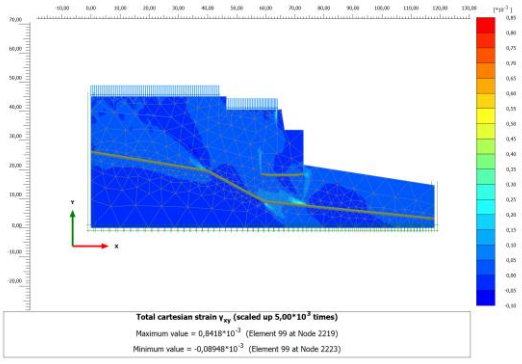

Figure 6.47. Case C - calculated total cartesian strains for drained behaviour and $R_{inter} = 0{,}5$

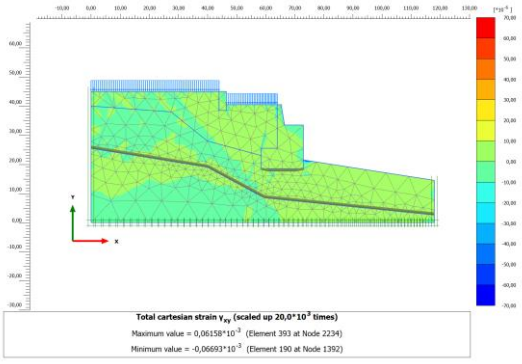

Figure 6.48. Case C - calculated total cartesian strains for drained behaviour and $R_{inter} = 0{,}7$

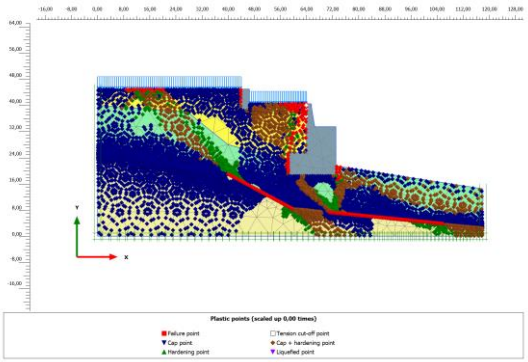

Figure 6.49. Case C - plastic points for drained behaviour and $R_{inter} = 0{,}5$

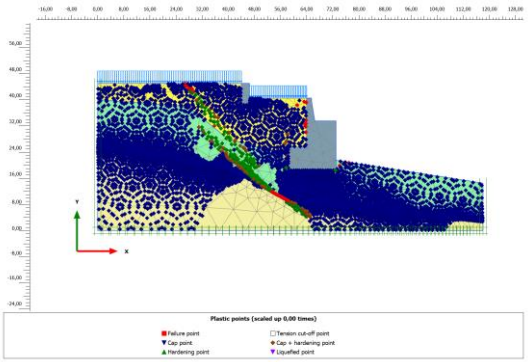

Figure 6.50. Case C - plastic points for drained behaviour and $R_{inter} = 0{,}7$

In both cases, the displacements show a planar slip surface. However, in the case where $R_{inter} = 0{,}5$ (Figure 6.45), the displacements are larger alongside that planar slip surface, whether in the case where $R_{inte} = 0{,}7$ (Figure 6.46), the displacements are more concentrated at the top of that surface.

For the total strains, they both are in small strain range with a maximum strain of $\sim 0{,}8 \times 10^{-3}$ for $R_{inter} = 0{,}5$ (Figure 6.47) and $\sim 0{,}6 \times 10^{-2}$ for $R_{inter} = 0{,}7$ (Figure 6.48). Nevertheless, for $R_{inter} = 0{,}5$ the larger strains are concentrated around the lower retaining wall an along the interface GZ2/ GZ3, whether for $R_{inte} = 0{,}7$, the strains are evenly distributed.

Failure points are along the planar interface described in the displacements for both cases. In the case where $R_{inter} = 0{,}5$ (Figure 6.49) failure points are also present around both retaining walls, especially in the lower platform, and at the interface GZ2/GZ3, whether in the case where $R_{inter} = 0{,}7$ (Figure 6.50), fewer points are present in the interface GZ2/GZ3 and along the lower retaining wall.

6.5.4. Comparison of the cases A, B and C

From the cases A, B and C (§6.5.1, §6.5.2 and §6.5.3), the simulation that better describes the response measured at the MSPA is case A, considering an undrained behaviour of the soil and a $R_{inter} = 0{,}7$, as it is the one that for the transversal displacements better fit the trend observed in the measured displacements of the inclinometers, a gradual increase of displacement at the surface and an increment of displacement at the interface GZ2/GZ3. Nevertheless, the strength reduction at the interface GZ2/GZ3 seems to generate sharp displacements at that area rather than a linear increase of displacement in that area, highlighted by the purple dashed line in Figure 6.51 and Figure 6.52.

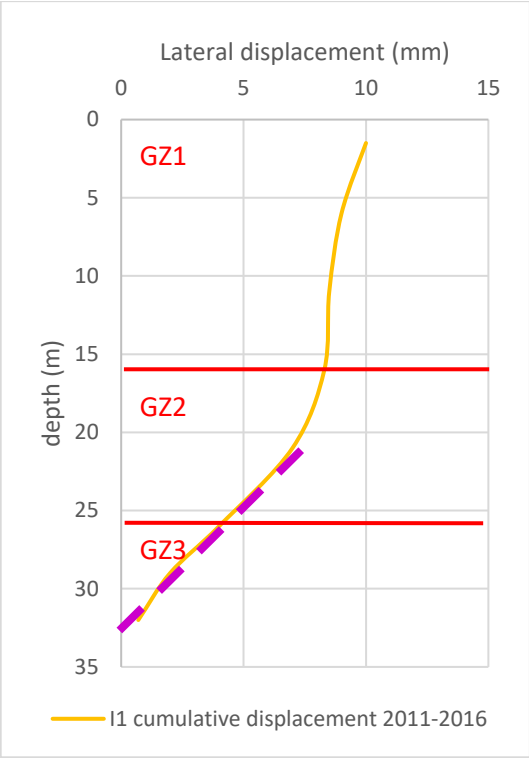

Figure 6.51. Cumulative transversal displacements of I1 between 2011 and 2016

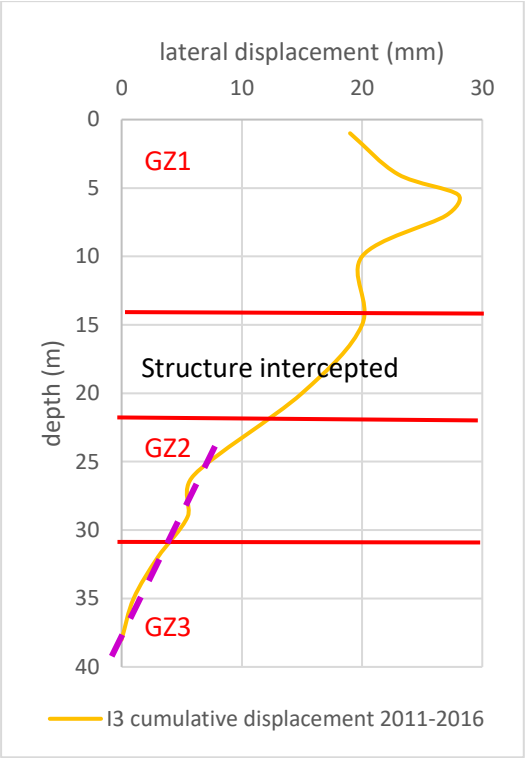

Figure 6.52. Cumulative transversal displacements of I3 between 2011 and 2016

In fact, what could explain this increase of displacement throughout GZ2 could be a stiffness reduction of the layer.

6.5.5. Analysis of stiffness reduction in GZ2

In §4.3.3.2, the stiffness parameters of GZ2 were determined using the average V_S. But, based on the analysis of the inclinometers profile, it was decided to test the hypothesis of GZ2 with lower stiffness. Several Vs values were tested, and it was identified that when $V_S = 300\ m/s$, the results were the ones that better fit the displacements measured in the inclinometers. The soil parameters used for that case are presented in Table 6.6, and the total displacements and strain distribution, as well as plastic points are presented in Figure 6.53, Figure 6.55 and Figure 6.57 respectively.

Table 6.6. Model parameters considering $V_S = 300\ m/s$ for GZ2

	GZ1	GZ2	GZ3
Soil parameters			
γ_{unsat} (kN/m^3)	16	20	25
γ_{sat} (kN/m^3)	16	20	25
ϕ' (º)[1]	30	35	40
c' (kN/m^2)[1]	0	0	0
c_u (kN/m^2)[2]	80	200	360
Parameters for soil stiffness			
E_{50}^{ref} (kN/m^2)	227 000	91 000	486 000
E_{oed}^{ref} (kN/m^2)	227 000	91 000	486 000
E_{ur}^{ref} (kN/m^2)	680 000	273 000	1 458 000
Parameters to describe soil behaviour in the small strains range			
G_0^{ref} (kN/m^2)	3 780 000	152 000	809 000
$\gamma_{0.7}$ (-)	$4{,}0 \times 10^{-5}$	$2{,}8 \times 10^{-4}$	$8{,}1 \times 10^{-5}$

[1] parameters used for drained analysis
[2] parameters used for undrained analysis

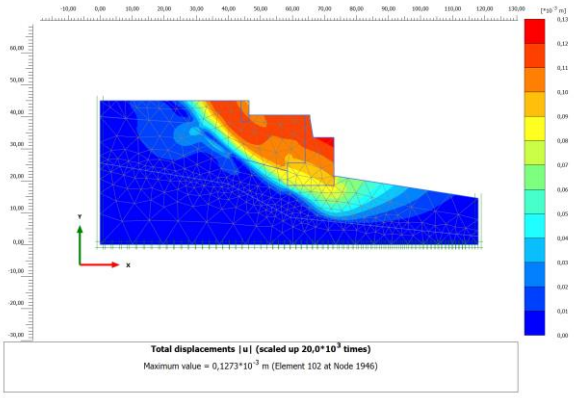

Figure 6.53. Calculated total displacements for $V_S = 300\ m/s$ in GZ2 with undrained behaviour

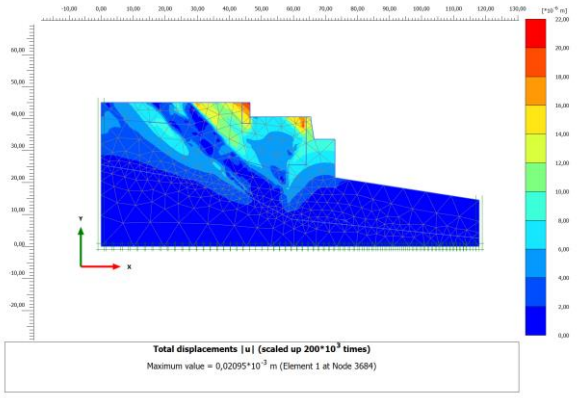

Figure 6.54. Calculated total displacements for $V_S = 300\ m/s$ in GZ2 with drained behaviour

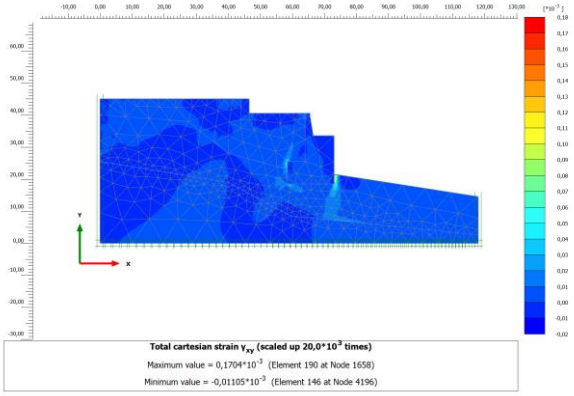

Figure 6.55. Calculated total cartesian strains for $V_S = 300\ m/s$ in GZ2 with undrained behaviour

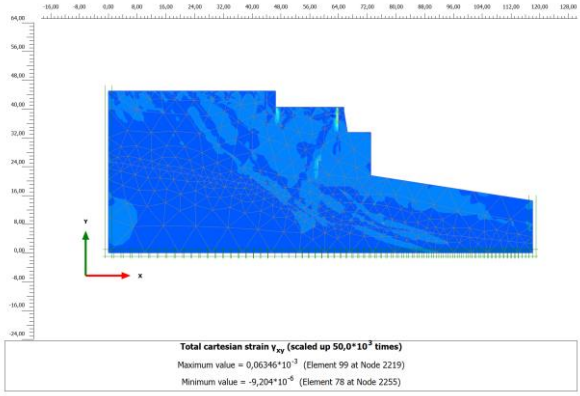

Figure 6.56. Calculated total cartesian strains for $V_S = 300\ m/s$ in GZ2 with drained behaviour

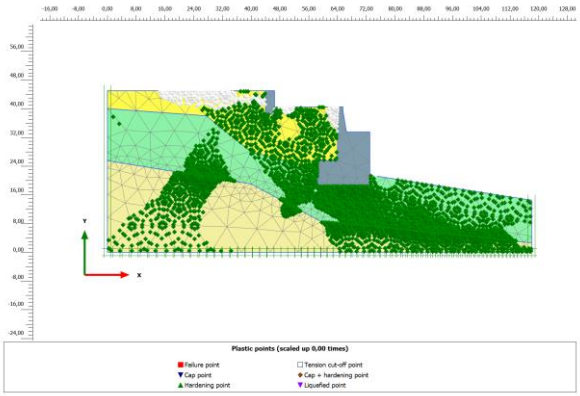

Figure 6.57. Plastic points for $V_S = 300\ m/s$ in GZ2 with undrained behaviour

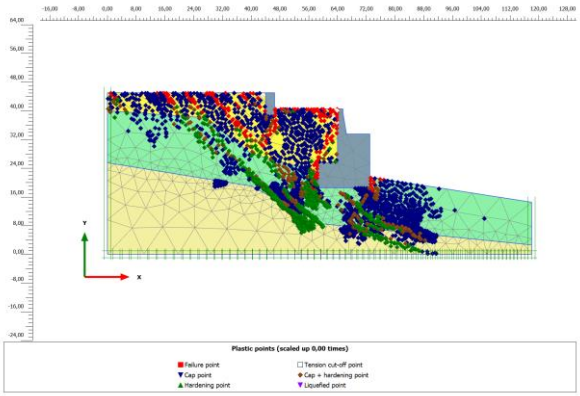

Figure 6.58. Plastic points for $V_S = 300\ m/s$ in GZ2 with drained behaviour

The maximum calculated displacement is ~0,1 mm, considering undrained behaviour (Figure 6.53), and negligible displacement for drained behaviour (Figure 6.54). These dosplacements are still smaller that the displacements observed in the topographical monitoring (§5.1) ~14 mm. A compound slip surface is observed in the undrained case and a more planar slip surface is observed in the drained case. The maximum total strain in $\sim 0{,}2 \times 10^{-3}$ in the undrained case (Figure 6.55) indicating that the model is in the small strain range, and the larger strains are present at the bottom of the lower retaining wall. For the drained case, the maximum total strain is $\sim 0{,}2 \times 10^{-3}$ (Figure 6.56) indicating small strain range and the larger strains are present at the top of the lower retaining wall and the bottom of the upper retaining wall.

The hardening points for the undrained case (Figure 6.57) are mostly concentrated below the lower retaining wall, where the larger strains are observed, as well as at the interface GZ2/GZ3, and no failure points are observed. In the drained case, failure points are present in the areas of larger displacement and strain.

The transversal calculated displacements for I1 and I3 are presented in Figure 6.59 to Figure 6.62.

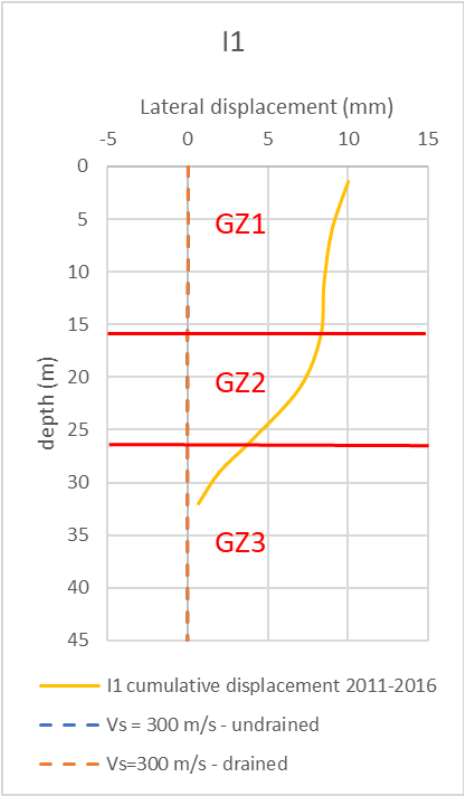

Figure 6.59. Calculated transversal displacements of I1 for $V_S = 300\ m/s$ in GZ2, and cumulative displacement 2011-2016

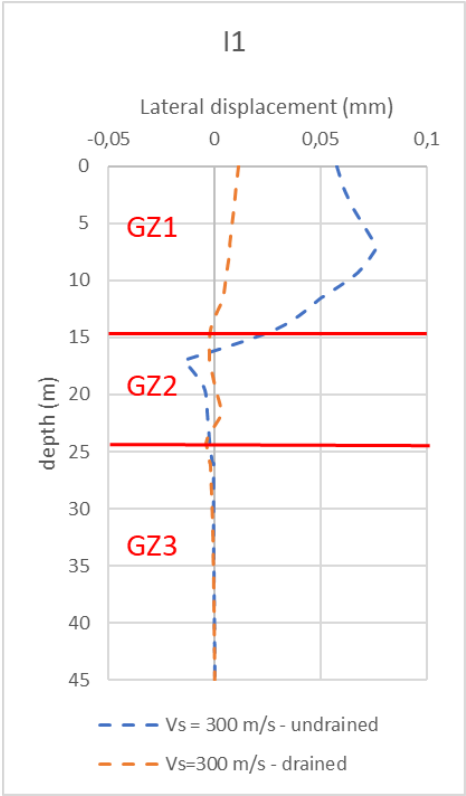

Figure 6.60. Calculated transversal displacements of I1 for $V_S = 300\ m/s$ in GZ2

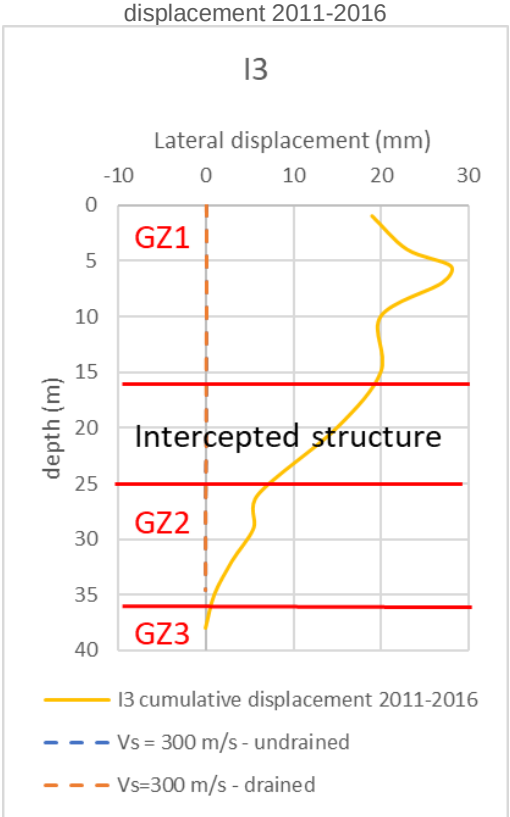

Figure 6.61. Calculated transversal displacements of I3 for $V_S = 300\ m/s$ in GZ2, and cumulative displacement 2011-2016

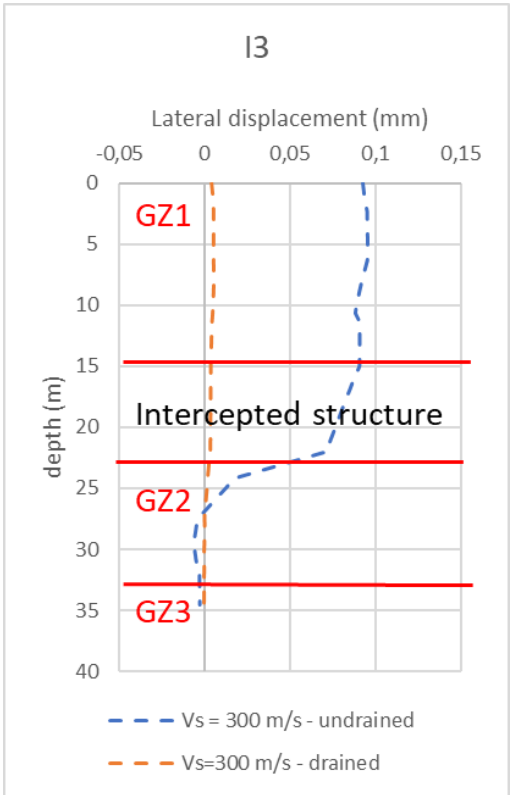

Figure 6.62. Calculated transversal displacements of I3 for $V_S = 300\ m/s$ in GZ2

As for cases A, B and C (§6.5.1, §6.5.2 and §6.5.3) the calculated displacements did not reach the amplitude of the measured displacements (Figure 6.59 and Figure 6.61). Yet, the trend of the calculated displacements is similar to the trend of displacements observed, as a linear increase of displacement at the interface GZ2/GZ3 is present now, especially in the case I3 (Figure 6.62).

Comparing now drained and undrained behaviour, with undrained behaviour (blue line in Figure 6.60 and Figure 6.62) presents a higher amplitude than with the drained behaviour (orange line in Figure 6.60 and Figure 6.62). Nevertheless, if total displacements are compared, the undrained behaviour (Figure 6.53) exhibits larger displacements in the lower retaining wall than in the upper retaining wall, which is what is observed on site.

6.5.6. Seismic action (pseudo-static analysis)

In §5.4.2, the hypothesis of M4,2 earthquake occurred on the 17/08/2017 induced movement in the MSPA was also simulated. To analyse the effect in the MSPA of the earthquake, a pseudo-static analysis was conducted in the undrained model of the MSPA, as it is the one that better represents the behaviour of the MSPA and seismic actions tend to have short term effects. For that a horizontal acceleration of 0,004g, that was the maximum acceleration measured in the nearest seismic station (IPMA, n.d.), was applied to the model without any interface properties reduction.

First, the plastic points of the MSPA are analysed not considering any interface (Figure 6.63).

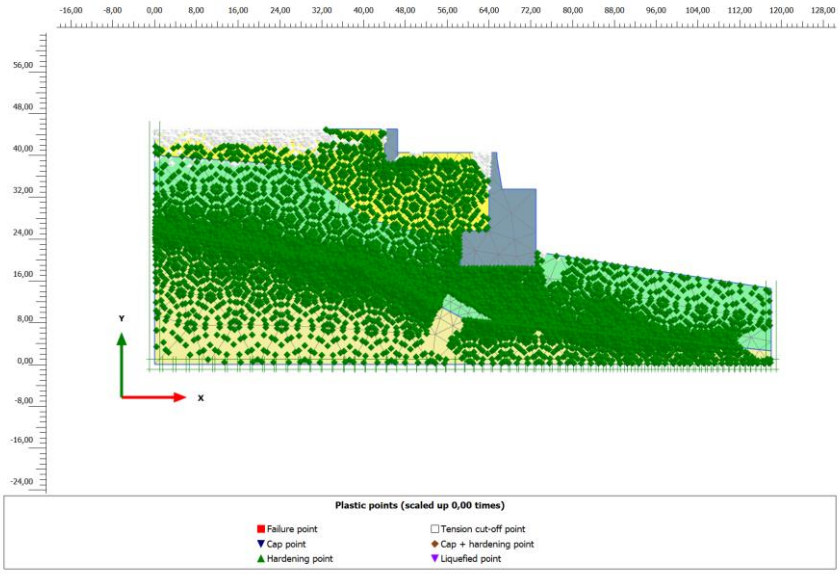

Figure 6.63. Plastic points of the MSPA not considering interfaces with a horizontal acceleration of 0,004g

The plastic points distribution (Figure 6.63) is similar to the one presented in §6.5.4 with none failure point. Next, the total displacements and strains distributions of the MSPA are analysed not considering any interface (Figure 6.64 and Figure 6.65).

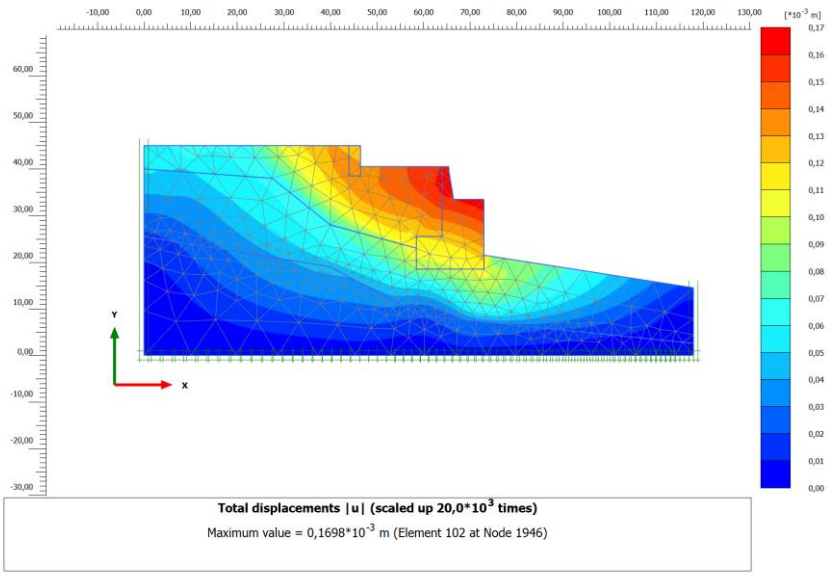

Figure 6.64. Total displacements of the MSPA not considering interfaces with a horizontal acceleration of 0,004g

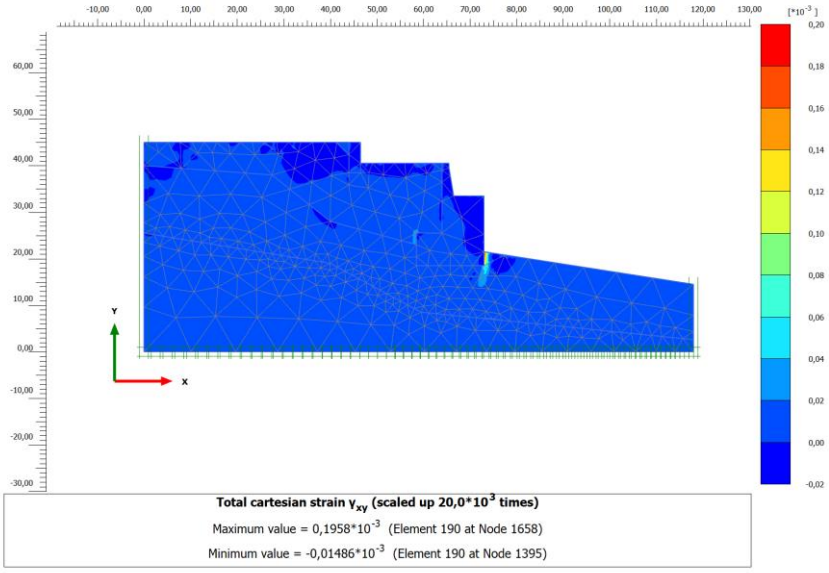

Figure 6.65. Total cartesian strains of the MSPA not considering interfaces with a horizontal acceleration of 0,004g

The total displacements (Figure 6.64) present similar patterns as the displacements presented n §6.5.4, and both show larger displacements in the lower platform and in GZ1, as well as a similar compound slip surface, planar bellow the MSPA and circular after the lower retaining wall. Nevertheless, the acceleration of 0,004g does not lead to major displacements in MSPA, the maximum displacement is ~0,2 mm. the maximum strain is $\sim 0{,}2 \times 10^{-3}$ indicating small strain range, and the larger strains appear at the bottom of the lower retaining wall.

The horizontal acceleration is then increased until the model reaches failure. Failure was only obtained for a horizontal acceleration of 0,50g, that corresponds to an earthquake of a magnitude 8 or 9. As interface 1 does not seem to have an impact in the MSPA stability in the case of an earthquake, the

analysis was only preformed for the case where no interfaces are considered. The total displacement and strain distributions are presented in Figure 6.66.

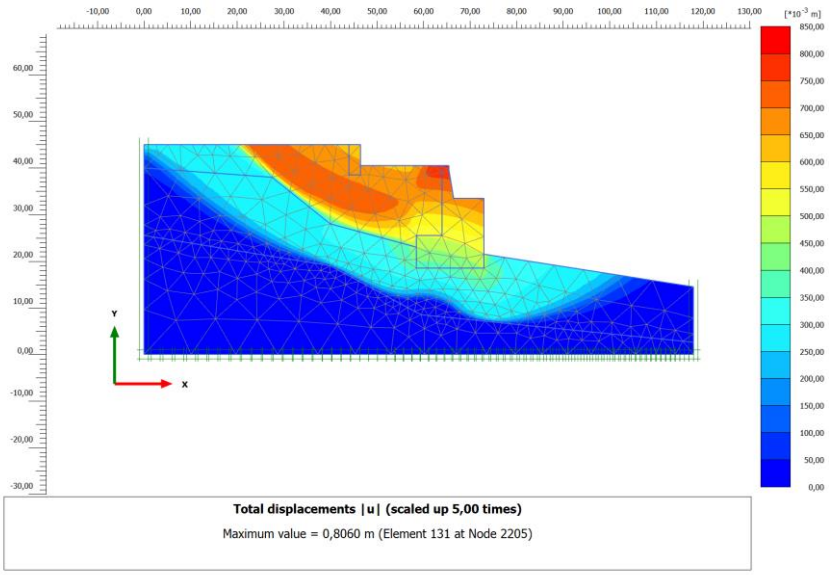

Figure 6.66. Total displacements of the MSPA not considering interfaces with a horizontal acceleration of 0,50g

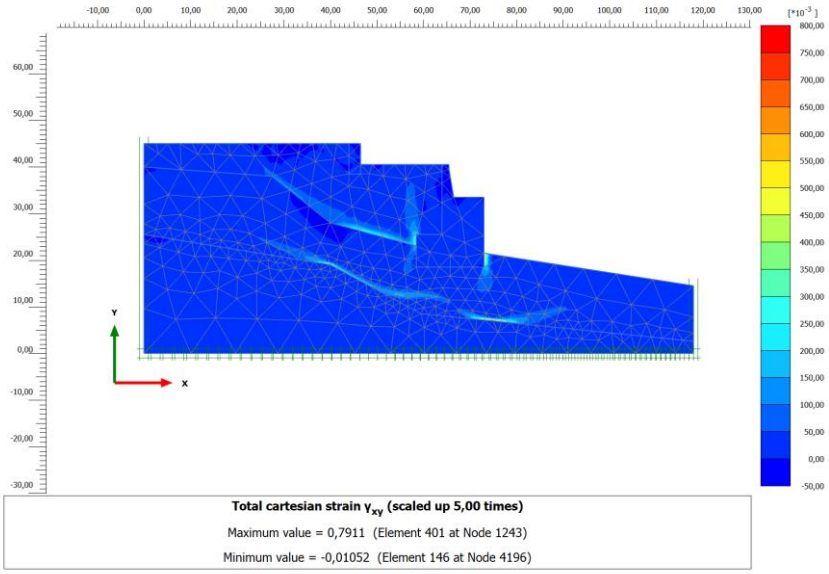

Figure 6.67. Total cartesian strains of the MSPA not considering interfaces with a horizontal acceleration of 0,50g

The maximum calculated displacement for a horizontal acceleration of 0,50g is ~0,81 m, that will probably not be reached as the MSPA would probably collapse before this amplitude of displacement is reached. Nevertheless, in Figure 6.66 it can be seen that the same compound slip surface appears, and there are no major displacements detected in GZ3. In fact, the larger displacements appear in GZ1, which indicated that in case of failure, GZ1 would be the one that slides. The maximum strain is ~0,8 (Figure 6.67) indicating large strain range, and the larger strains appear at the interface of each GZ, underlining the compound slip surface observed in the total displacements, which is typical of slides (§2.2).

7. Concluding remarks

7.1. Conclusions

The lower retaining wall of the MSPA presents two main patterns of movement were observed between 2010 and 2012. The patterns are (i) sinusoidal variations with a period of one year, and (ii) an increasing displacement in the transversal direction, accumulating ~14 mm displacement in three years. Additionally, the inclinometers identified relative motion ~24 m deep near the interface between two geotechnical zones. Comparing the displacements observed with the states of activity of a landslide (§2.4), between 2010 and 2012, the MSPA seems to be in active state, as the displacements are not fully stable but are not exponential either.

Using the Fukuzono (1985) method to assess the eventual time of failure, it was difficult to find a clear trend, as the seasonal response could have masked the trend. This result, highlighting difficulty to predict the time of failure and the importance of monitoring other variables than displacements (e.g. soil water content, soil expansibility).

The possible causes for these displacements and its analysis are summarized in Table 7.1.

Table 7.1. Possible causes of displacement of the MSPA

Causes of movement	Comments
Precipitation	Precipitation seems to be the origin of the seasonal displacements observed. However, it does not seem to be the cause of the increasing displacements observed in the transversal direction.
Earthquakes	Based on the measured displacements (§5.4.2), the M4,2 earthquake did not had an impact on the MSPA displacements. In the numerical simulation (§6.5.6) the maximum calculated displacement for the maximum acceleration generated by that M4.2 earthquake is ~0,2 mm, which is compatible with the measurements. The numerical model proposed for the MSPA collapses for accelerations over 0,50g that corresponds to very strong earthquake.
Forming slip surface between GZ2 and GZ3	In the displacements measured by the inclinometers (§5.2) a possible slip surface between GZ2 and GZ3 was identified, and it impact on the MSPA displacements was confirmed by the numerical model (§6.5). Although this can slip surface explains in part the trend of the displacements it does not explain their amplitude. The cause for a weaker interface is not easy to explain, because the area was built more than a century ago.
Stiffness reduction in GZ2	The stiffness reduction in GZ2 generates a displacement profile similar to the one measured in the inclinometers in shape, but the amplitude of the displacements is significantly smaller.

Although there are various causes for the increasing displacements in the MSPA, all these hypotheses lead to a similar compound slip surface: planar bellow the MSPA and circular after the lower retaining wall with larger displacements in the lower platform and GZ1, concluding that in case of rupture this slip surface is the more likely to occur.

7.2. Future developments

For future developments, the following topics are proposed:

- Improve the numerical simulation of the MSPA, for example:
    - develop a 3D model of the case study
    - perform dynamic analysis
    - consider variations in the water level
    - reduce the stiffness of the soil, especially in ZG1
- Perform additional site investigation, including laboratory test as triaxial tests, in situ measurement of water content, and characterization of the materials in composing GZ2 as well as the interface ZG2/ZG3, as well as better define the geometry of the lower retaining wall
- Perform addition site investigation in sites where *Areolas da Estefânia* are present to better characterize this geological layer.
- To monitor the displacements of the MSPA, topographical monitoring is important to determine the 3D displacements of the walls. Nevertheless, it could be interesting to perfect the InSAR monitoring with perhaps better-quality images to obtain more points of measurement and define not only the displacements of the retaining walls, but also the displacements of the ground. The InSAR monitoring could provide a way to monitor the displacements of the MSPA with more regularity, the monitoring can be done from a distance and even create an Early Warning System in case of landslide.

References

Angeli, M. G., Gasparetto, P., Pasuto, A., & Silvano, S. (1989). Examples of landslide instrumentation (Italy). *12th International Conference on Soil Mechanics and Foundation Engineering, 3*, 1531–1534.

Asaoka, A. (1978). Observational Procedure of Settlement Prediction. *Soils and Foundations*, 18(4), 87–101.

Azimi, C., Biarez, J., & Desvarreux, P. (1988). Prévision d'éboulement en terrain gypseux. *5th International Symposium on Landslides*, 1, 531–536.

Brinkgreve, R. B. J., Zampich, L. M., & Ragi Manoj, N. (Eds.). (2019). PLAXIS Material Models. In *PLAXIS CONNECT Edition V20*.

Carvalho, N. (2017). *Soluções de Estabilização de Taludes em Meio Urbano*. Instituto Superior Técnico, Universidade de Lisboa. Master Thesis

Casagli, N., Tibaldi, A., Merri, A., Del Ventisette, C., Apuani, T., Guerri, L., Fortuny-Guasch, J., & Tarchi, D. (2009). Deformation of Stromboli Volcano (Italy) during the 2007 eruption revealed by radar interferometry, numerical modelling and structural geological field data. *Journal of Volcanology and Geothermal Research, 182*(3–4), 182–200.

Cheng, Y., Huo, A., Zhang, J., & Lu, Y. (2015). Early warning of meteorological geohazard in the Loess Plateau: a study in Huangling County of Shaanxi Province in China. *Environmental Earth Sciences, 73*(3), 1057–1065.

Chinese Government. (2017). *Top leaders urge all-out rescue efforts in SW China landslide*. Retrieved April 12, 2020 http://english.www.gov.cn/news/top_news/2017/06/24/content_281475696976294.htm

Cruden, D. M. (1991). A Simple Definition of a Landslide. In *Bulletin of the International Association of Engineering Geology Nº43* (pp. 27–29).

Dok, A., Fukuoka, H., Katsumi, T., & Inui, T. (2011). Tertiary Creep Reproduction in Back-Pressure-Controlled Test to Understand the Mechanism and Final Failure Time of Rainfall-Induced Landslides. *Disaster Prevention Research Institute Annuals*, 54(B), 263–270.

EMSC (European-Mediterranean Seismological Centre). (n.d.). *Search for earthquakes*. Retrieved August 9, 2020, from https://www.emsc-csem.org/Earthquake/?filter=yes

Eurocode 8. (2010). Design of structures for earthquake resistance—Part 1: General rules, seismic actions and rules for buildings (EN 1998-1: 2010). In *European Committee for Normalization*.

Foti, S., Hollender, F., Garofalo, F., Albarello, D., Asten, M., Bard, P.-Y., Comina, C., Cornou, C., Cox, B., Di Giulio, G., Forbriger, T., Hayashi, K., Lunedei, E., Martin, A., Mercerat, D., Ohrnberger, M., Poggi, V., Renalier, F., Sicilia, D., & Socco, V. (2018). Guidelines for the good practice of surface wave analysis: a product of the InterPACIFIC project. *Bulletin of Earthquake Engineering, 16*(6), 2367–2420.

Froude, M. J., & Petley, D. N. (2018). Global fatal landslide occurrence from 2004 to 2016. *Natural Hazards and Earth System Sciences, 18*, 2161–2181.

Fukui, K., & Okubo, S. (1997). Life expectancy and tertiary creep for rock. *Fall Meeting of Mining and Materials Processing Institute of Japan*, 91–94.

Fukuzono, T. (1985). A method to predict the time of slope failure caused by rainfall using the inverse number of velocity of surface displacement. *Journal of Japan Landslide Society, 22*(2), 8–13.

Fukuzono, T. (1984). A method for predicting the failure time of a sandy soil slope using the inverse number of velocity. *23rd Meeting of Japan Landslide Society*, 80–81.

Fukuzono, T., & Terashima, H. (1982). Experimental study of the process of failure in cohesive soil slope caused by rainfall. *Nat. Disaster Res. Rep., 29*, 103–122.

Geotest. (2011). *Miradouro de S. Pedro de Alcântara - Lisboa Estudo Geológico e Geotécnico Relatório*.

Geotest (2016). *Relatório VIII de Leituras em Tubos Inclinométricos e Piezométricos*.

Gigli, G., Fanti, R., Canuti, P., & Casagli, N. (2011). Integration of advanced monitoring and numerical modeling techniques for the complete risk scenario analysis of rockslides: The case of Mt. Beni (Florence, Italy). *Engineering Geology, 120*(1–4), 48–59.

Guzzetti, F., Peruccacci, S., Rossi, M., & Stark, C. P. (2007). Rainfall thresholds for the initiation of landslides in central and southern Europe. *Meteorology and Atmospheric Physics, 98*(3–4), 239–267.

Hayashi, S., Komamura, F., Park, B., & Yamamori, T. (1988). On the forecast of time to failure of slope—approximate forecast in the early period of the tertiary creep. *Journal of Japan Landslide Society, 25*(3), 11–16.

Hutchinson, J. N. (1967). The Free Degradation of London Clay cliffs. *Geotechnical Conference on Shear Strength Properties of Natural Soils and Rocks, 1*, 113–118.

Intrieri, E., Carlà, T., & Gigli, G. (2019). Forecasting the time of failure of landslides at slope-scale: A literature review. *Earth-Science Reviews, 193*, 333–349.

Intrieri, E., & Gigli, G. (2016). Landslide forecasting and factors influencing predictability. *Natural Hazards and Earth System Sciences, 16*(12), 2501–2510.

Intrieri, E., Raspini, F., Fumagalli, A., Lu, P., Conte, S., Farina, P., Allievi, J., Ferretti, A., & Casagli, N. (2018). The Maoxian landslide as seen from space: detecting precursors of failure with Sentinel-1 data. *Landslides, 15*(1), 123–133.

Iovine, G., Petrucci, O., Rizzo, V., & Tansi, C. (2006). The March 7 2005 Cavallerizzo (Cerzeto) landslide in Calabria -. *10th IAEG Congress, 785*, 1–12.

Ishibashi, I., Zhang, X. (1993). Unified dynamic shear moduli and damping ratios of sand and clay. *Soils and Foundations, 3*(1), 182-191.

IPMA (Instituto Portugês do Mar e da Atmosféra). (n.d.). *Portugal ShakeMap: Estimated Instrumental Intensity*. Retrieved August 9, 2020, from http://shakemap.ipma.pt/2017081706445801/intensity.html

Jiang, S., Yang, Y., & Hunt, K. (2017). *Rescue called off at flattened village as Chinese authorities warn of landslides*. CNN. Retrieved April 12, 2020 https://edition.cnn.com/2017/06/26/asia/china-landslide-rescue-called-off/index.html

Karstunen, M. (2011). *Drained and Undrained Analysis*. University of Strathclyde.

Kulhawy, F. H., & Mayne, P. W. (1990). Manual on Estimating Soil Properties for Foundation Design. In *EPRI Report EL-6800*.

Lacasse, S., & Nadim, F. (2009). Landslide risk assessment and mitigation strategy. *Landslides - Disaster Risk Reduction*, 31–62.

Laranjo, M. (2013). *Argilas Miocénicas de Lisboa Parametrização para o Dimensionamento de Estruturas Geotécnicas*. Faculdade de Engenharia, Universidade do Porto. PhD Thesis.

Minamitani, T. (2007). *An Experimental Study on the Parameter Affecting Tertiary Creep Deformation of Soils*. Kyoto University.

Mufundirwa, A., Fujii, Y., & Kodama, J. (2010). A new practical method for prediction of geomechanical failure-time. *International Journal of Rock Mechanics and Mining Sciences, 47*(7), 1079–1090.

Obrzud, R., Truty, A. (2018). *The Hardening Soil model – A Practical Guidebook*. Zace Services Ltd, Software engineering.

Oliveira, L. (n.d.). *Seismic microzonation studies for Lisbon*. Faculdade de Ciências, Universidade de Lisboa. PhD Thesis (expected 2022).

Petley, D. N., Bulmer, M. H., & Murphy, W. (2002). *Patterns of movement in rotational and translational landslides. Geology, 30*(8), 719–722.

Roque, D. (2020). *Displacement Measurement Through Insar Geodesy for Structural Health Monitoring*. Universidade de Lisboa. PhD thesis.

Rose, N. D., & Hungr, O. (2007). Forecasting potential rock slope failure in open pit mines using the inverse-velocity method. *International Journal of Rock Mechanics and Mining Sciences, 44*, 308–320.

Saito, M. (1969). Forecasting time of slope failure by tertiary creep. *7th International Conference on Soil Mechanics and Foundation Engineering, 2*, 677–683.

Saito, M., & Uezawa, H. (1961). Failure of soil due to creep. *5th International Conference on Soil Mechanics and Foundation Engineering, 1*, 315–318.

Segoni, S., Battistini, A., Rossi, G., Rosi, A., Lagomarsino, D., Catani, F., Moretti, S., & Casagli, N. (2015). Technical Note: An operational landslide early warning system at regional scale based on space-time-variable rainfall thresholds. *Natural Hazards and Earth System Sciences, 15*(4), 853–861.

Semenza, E., & Melidoro, G. (1992). Proceedings of the meeting on the 1963 Vaiont landslide. In E. Semenza & G. Melidoro (Eds.), *Proceedings of the meeting on the 1963 Vaiont landslide*.

Skempton, A. W., & Hutchinson, J. (1969). Stability of Natural Slopes and Embankment Foundations. *7th International Conference on Soil Mechanics and Foundation Engineering, Mexico, State of the Art Volume*, 291–340.

Teixeira Duarte Engenharia, S.A. (2017a). *Estabilização do Miradouro de São Pedro de Alcântara.*

Teixeira Duarte Engenharia, S. A. (2017b). *Miradouro de São Pedro de Alcântara - III Séculos de História.*

UNDRR. (2019). *Global Assessment Report on Disaster Risk Reduction*. United Nations Office for Disaster Risk Reduction (UNDRR).

Varnes, D. J. (1978). Slope Movement Types and Processes. In *Landslides: Analysis and Control* (pp. 11–33). National Academy of Sciences.

Varnes, D. J. (1984). *Landslide hazard zonation : A review of principles and practice*. UNESCO.

WP/WLI (The International Geotechnical Societies' UNESCO Working Party on World Landslide Inventory). (1993a). A suggested method for describing the activity of a landslide. In *Bulletin of the International Association of Engineering Geology Nº47* (pp. 53–57).

WP/WLI (The International Geotechnical Societies' UNESCO Working Party on World Landslide Inventory). (1993b). *Multilingual Landslide Glossary*. BiTech Publishers Ltd.

Zavodni, Z. M., & Broadbent, C. . (1980). Slope failure kinematics. *Canadian Institute of Mining, Metal Petroleum (CIM), 73*, 69–74.

Annexes

Annex A. Values of N_{SPT} and N^*_{SPT} for each borehole

Depth(m)	S1		S2		S3		S4		S5	
	Nspt	Nspt*	Nspt	Nspt*	Nspt	Nspt*	Nspt	Nspt*	Nspt	Nspt*
1,5	4	4	8	8	6	6			6	6
3	22	22	9	9	4	4			4	4
4,5	25	25	11	11	4	4			4	4
6	21	21	9	9	4	4			5	5
7,5	14	14	15	15	5	5			3	3
9	18	18	19	19	6	6			3	3
10,5	10	10	16	16	9	9			2	2
12	12	12	29	29	8	8			42	42
13,5	14	14	28	28	6	6			14	14
15	18	18	22	22					21	21
16,5	11	11	60	72					3	3
18	60	86	19	19					60	69
19,5	19	19	18	18					31	31
21	21	21	45	45					26	26
22,5	14	14	60	90	7	7			22	22
24	22	22	24	24	17	17	42	42	28	28
25,5	25	25	25	25	19	19	42	42	31	31
27	52	52	31	31	28	28	42	42	37	37
28,5	60	60	52	52	60	120	35	35	19	19
30	60	64	60	60	32	32	33	33	25	25
31,5	60	60	48	48	32	32	43	43	60	180
33	-	-	41	41	42	42	43	43	60	72
34,5	-	-	60	60	60	60	43	43	60	900
36	-	-	49	49	60	225	60	64	-	-
37,5	-	-	50	50	60	257	60	69	-	-
39	-	-	60	90	-	-	60	75	-	-
40,5	-	-	60	120	-	-	-	-	-	-
42	-	-	60	106	-	-	-	-	-	-

	GZ1
	GZ2
	GZ3
	Structure intercepted

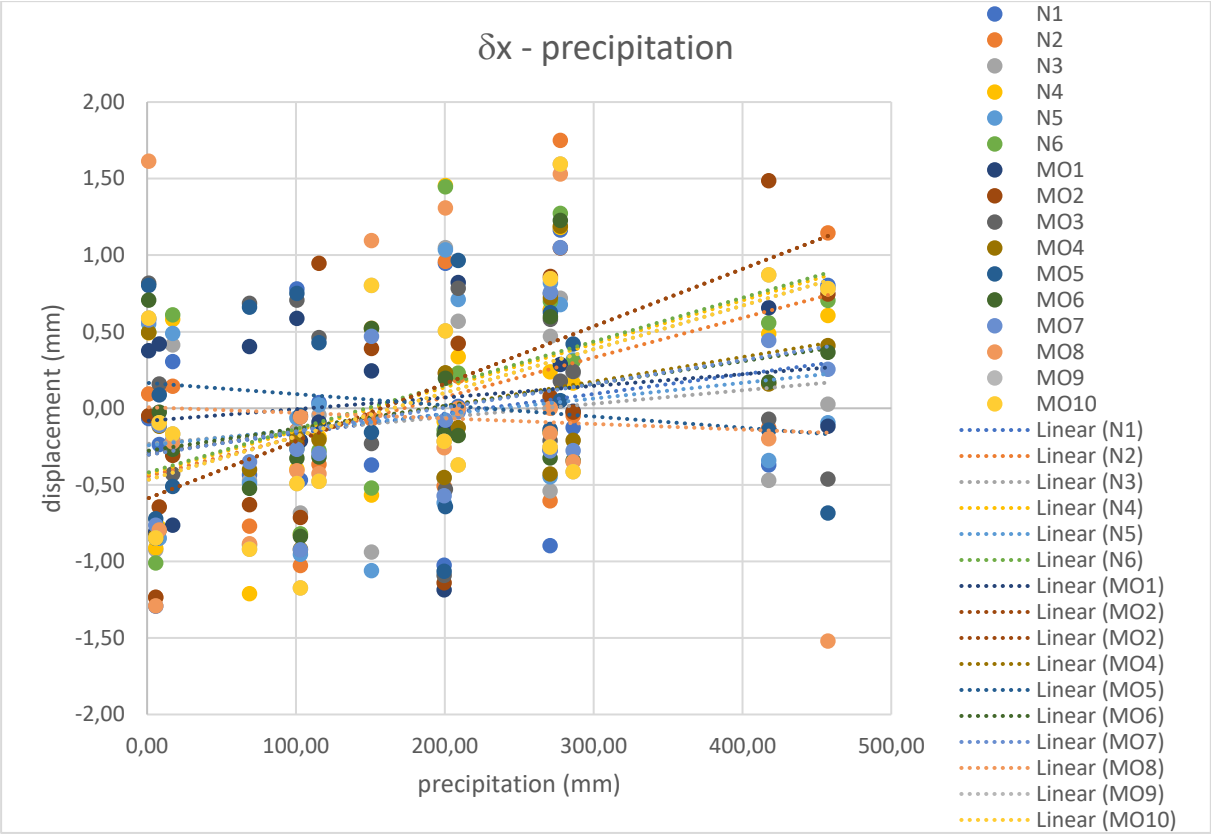

Annex B. Accumulated longitudinal (δ_x) displacement versus the accumulated precipitation for two months

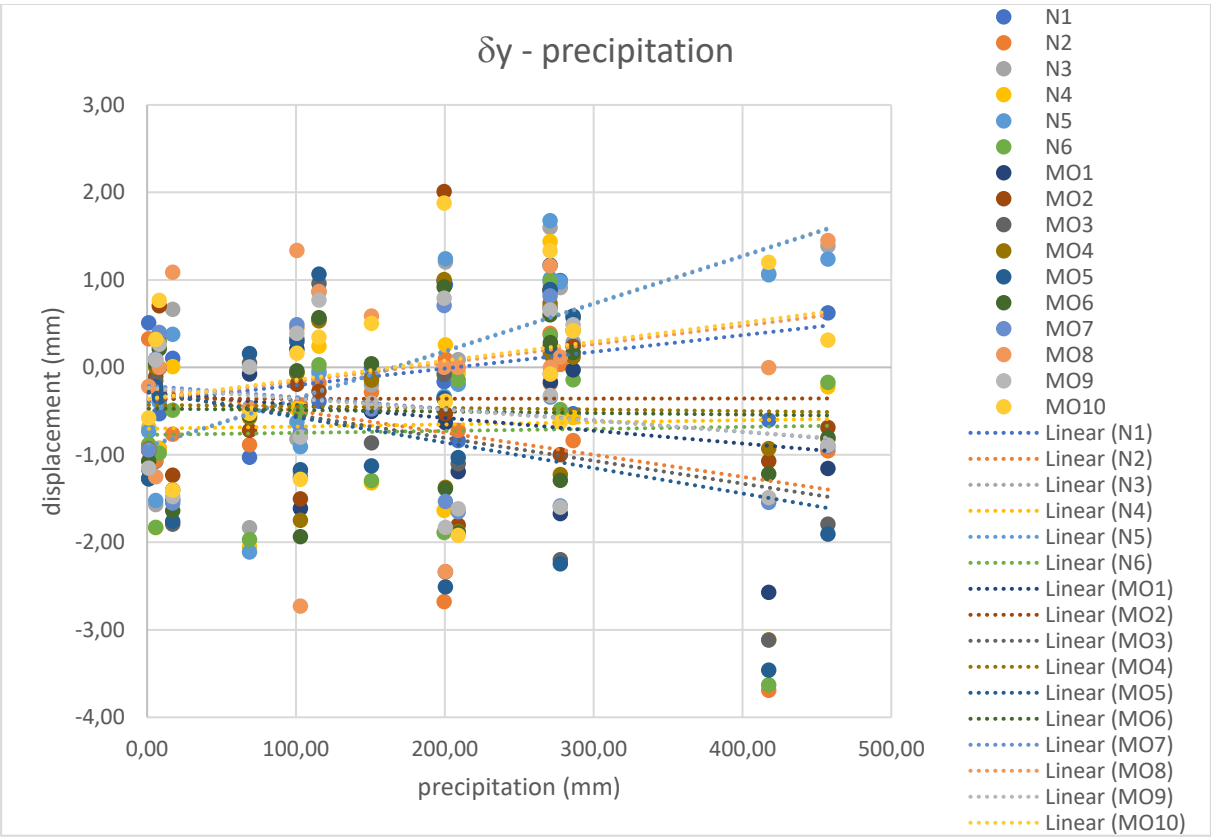

Annex C. Accumulated transversal (δ_y) displacement versus the accumulated precipitation for two months

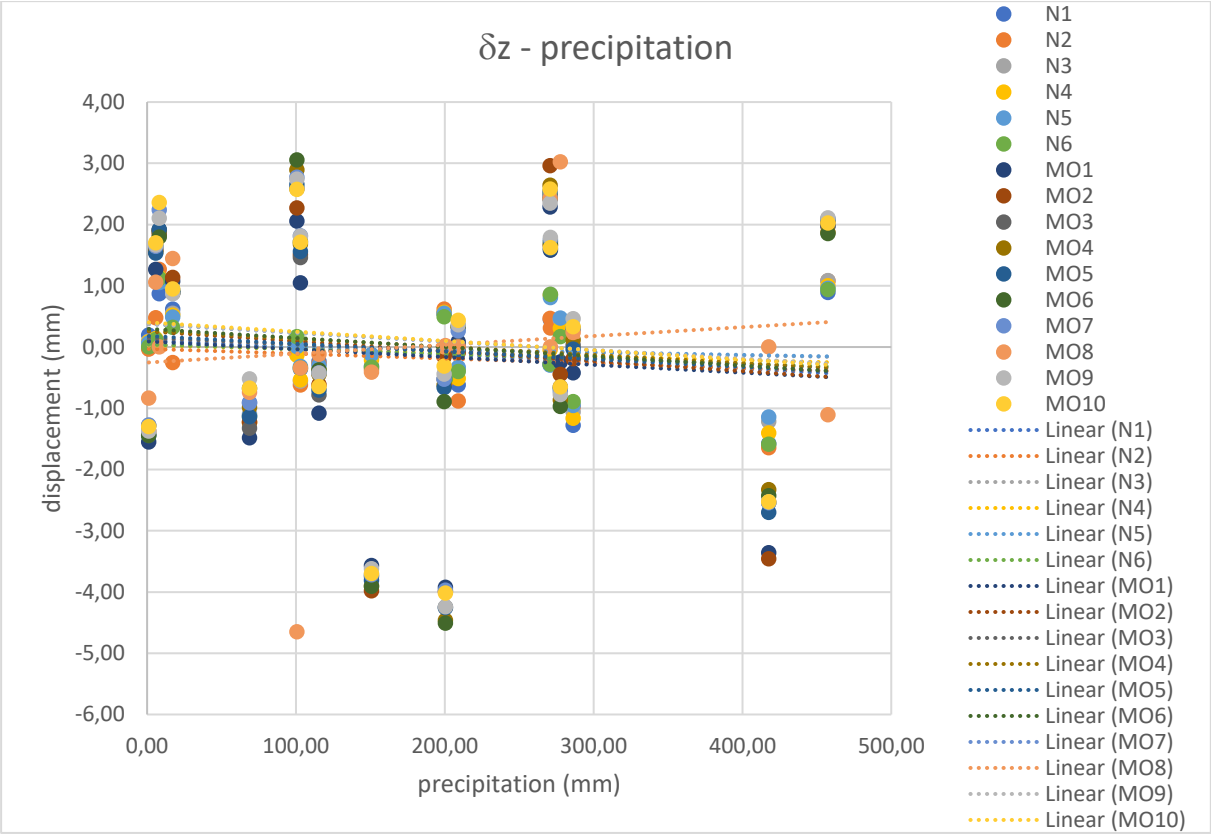

Annex D. Accumulated vertical (δ_z) displacement versus the accumulated precipitation for two months